Laboratory Studies of Astrophysical Ices

Thesis by

Richard W. Dissly

In Partial Fulfillment of the Requirements

for the Degree of

Doctor of Philosophy

California Institute of Technology

Pasadena, California

1995

(Submitted September 6, 1994)

For my Parents

Acknowledgments

First and foremost, I would like to thank my family for their love, help, and understanding through this experience. Your enthusiasm and faith in me have been a tremendous help. Lydia, thank you for your patience, especially in the last few months. No matter what happened at work, coming home to you made each day a good one.

Academically, I would like to acknowledge several people who helped guide me through the research maze. My most recent advisors at JPL, Vince Anicich and Mark Allen, deserve a great deal of credit for my development as a scientist. Thank you for the patience you have shown through the slow and rough spots on the way. Vince, your cheerfulness actually made it *fun* to come to work (although Gatewood would never admit it!). I'll really miss the whole coffee break crowd. A special thanks goes out to Murray McEwan, who was always willing to drop whatever he was doing to help. Your unselfishness is rare; I greatly admire you as a scientist and as a person.

In the time I have spent at Caltech, I have met so many good people and had enough memorable experiences that a brief acknowledgment cannot do them justice. I would just like to express my sincere appreciation for all the love and support that friends have provided. You put down a lot of roots in six years. Leaving will be harder than I ever would have thought.

Abstract

This thesis reports the results of three laboratory studies, each concerned with some aspect of ices in an astrophysical environment, presented as independent papers:

1. Molecular hydrogen is the most abundant molecule in interstellar space, and is therefore of central importance to the physics and chemistry of that environment. Experiments simulating the codeposition of molecular hydrogen and water ice on interstellar grains demonstrate that amorphous water ice at 12 K can incorporate a substantial amount of H_2, up to a mole ratio of $H_2/H_2O = 0.53$. We find that the physical behavior of ~80% of the hydrogen can be explained satisfactorily in terms of an equilibrium population, thermodynamically governed by a wide distribution of binding site energies. Such a description predicts that gas phase accretion could lead to mole fractions of H_2 in interstellar grain mantles as high as 0.3. Accretion of gas phase H_2 onto grain mantles, rather than photochemical production of H_2 within the ice, could be a general explanation for recent observations of frozen H_2 in interstellar ices. The possibility of interstellar grains that are rich in H_2 could strongly affect our understanding of grain surface chemistry and gas-grain interactions.

2. Photochemical models of Triton's atmosphere predict ethylene (C_2H_4) as a primary product of methane photodissociation, formed at a high enough level that it should be readily observable as a surface condensate in $\leq 10^6$ years, yet it has not been observed. Ultraviolet photolysis experiments on C_2H_4 ice were done to simulate its irradiation on Triton's surface. Our results show that C_2H_4 ice is readily dissociated by radiation of wavelengths $\leq$ 1849Å, with C_2H_2 ice as a primary product. Dilution in an inert N_2 matrix does not affect the photochemical yield of C_2H_2, suggesting that the reaction $C_2H_4 \rightarrow C_2H_2$ is unimolecular. Quantum yields for both the destruction of C_2H_4 and the formation of C_2H_2 are discussed, as functions of both irradiation wavelength and dilution in N_2 ice. Applying these results to Triton, we find that the ambient UV flux reaching Triton's surface is more than adequate to prevent the build-up of an ethylene ice layer.

3. Thermal models of icy satellite surfaces that allow the scattering and absorption of incident sunlight at significant depths predict an enhancement of subsurface temperatures over the mean surface temperature known as the solid-state greenhouse effect. We verify that a solid-state greenhouse can readily be produced in a bed of evacuated glass beads, used as a crude analog for the surface of an icy body. Measurements of the thermal and radiative properties thought to govern the size of this temperature enhancement confirm that it can be reasonably predicted from these parameters.

Table of Contents

List of Figures

Chapter 1:

Chapter 2:

List of Tables

Chapter 2:

Chapter 3:

Overview

This thesis presents the results of three experimental projects unified by a common theme: each represents an attempt to understand a chemical or physical process in laboratory ices on a mechanistic level, so that the results may be quantitatively applied in an astrophysical context. As time scales and ambient conditions may be very different between the lab and space, such a level of understanding is necessary to properly apply experimental results to an astrophysical environment.

In the first project, I tried to define an upper limit to the amount of H_2 that could be incorporated in amorphous water ice. This work was motivated by a wide range of theoretical predictions about how much H_2 should be stable on the icy surfaces of interstellar grains. In the process of trying to understand how the laboratory data could be applied to interstellar conditions, I found an interesting way to interpret the experimental results of H_2 release at relatively high temperatures (up to 70 K): most of the H_2 in the mixtures could be adsorbed on the surface of a highly porous water substrate, rather than trapped in the water matrix, as had been suggested previously (Laufer *et al.* 1987). If the range of binding energies on the water "surface" is large enough, then some H_2 would desorb even at these high temperatures. This can be viewed as an equilibrium process; the adsorbed population of H_2 represents a thermal distribution. If such a model is true for interstellar ices, the implications for grain surface chemistry could be profound: H_2 occupying

a large fraction of the surface physisorption sites, inhibiting the condensation of other species, and modifying the kinetics of surface reactions.

While I was working on this, a spectroscopic detection of frozen H_2 in interstellar ices was reported (Sandford *et al.* 1993). The project was suddenly not just an academic exercise! I recently submitted the paper given as Chapter 1, co-authored with Mark Allen and Vince Anicich, to *The Astrophysical Journal*, where it will appear in the November 10, 1994, issue. The purpose of the paper is to suggest that H_2 adsorption could be responsible for the observational detection, so that high H_2 abundances could be a widespread phenomenon. The paper does not state this as the definitive explanation, but rather as an alternative to the mechanism proposed by Sandford *et al.* (1993) of *in situ* H_2 production from the photodissociation of H_2O or CH_3OH ice. A similar explanation was also put forward by Buch and Devlin (*Ap. J. Letters*, in Press), which will precede our version in publication by about six weeks. I suppose this is an important aspect of my graduate education as well!

The outstanding issue remaining with this project is to determine the exact nature of the H_2 incorporation in water ice, both in the lab and in the interstellar medium. If the observed H_2 in the laboratory experiments is largely due to matrix trapping, and its gradual release controlled by conformational changes in the water ice, then the high trapped experimental abundances are probably an artifact of fast laboratory deposition rates. As such, the high fractional abundance of H_2 seen in the laboratory may not be applicable to interstellar conditions. Since the submission of our paper, Jenniskens and Blake (1994) have reported observing gradual structural changes in amorphous water ice samples from 38 K to 68 K, using an electron diffraction technique. This lends support to the view that changes in the water matrix control the release of trapped volatiles. More work is needed to

accurately pin down the structure and associated energetics of amorphous water ice in interstellar environments.

The project described in Chapter 2 involves measuring the kinetics of C_2H_4 photolysis in the solid-state. Previous research on the chemical effects of irradiating ices, both with ultraviolet light and energetic particles, is extensive. With regard to astrophysical environments, however, most of this research has been qualitative in nature, particularly for the laboratory studies of UV photolysis. Research has focused on cataloging the chemical products due to photolysis, and trying to match observed speciation or spectra, without a detailed understanding of chemical mechanisms, and almost no regard for kinetics. The point of the work in Chapter 2 is twofold. In a narrow framework, it addresses specific questions: what is the photochemical destruction rate of C_2H_4 ice on Triton's surface, and what are the chemical consequences of this photolysis? But in a larger context, this work demonstrates that understanding solid-state chemical kinetics is experimentally tractable, while it remains largely untouched as a field of study. A systematic survey of quantitative radiation effects, both UV and particle, on astrophysically relevant ices and mixtures of ices, needs to be undertaken to understand the chemical processing of icy surfaces and interstellar grain mantles.

With regard to the specific topic of Chapter 2, the work has produced both results and questions. The quantum yield for destruction of C_2H_4 ice was found to be roughly unity throughout the vacuum UV, so that on Triton's surface, the photochemical destruction rate is faster than the predicted condensation rate. The experiments have also established acetylene and molecular hydrogen as primary products of C_2H_4 photodissociation. But the C_2H_4 destruction has not been fully accounted for in the observed total

product yield, so there is still "missing mass" somewhere in the system. A possible explanation is that the products are tied up as polymers, which may help explain the observed coloration of Triton's surface. The results presented in this chapter will be submitted to *Icarus* in somewhat modified form.

Chapter 3 is a summary of work that developed out of a proposition I did with Bob Brown at JPL, trying to convince a surprisingly slow-to-believe community that the solid-state greenhouse effect was not just a fantasy. The primary goal of the project was simply to demonstrate experimentally that steady-state thermal profiles as a function of depth in planetary surfaces depend on where the radiation is being deposited. If incident visible radiation is absorbed over an extended depth, the steady-state temperature distribution is fundamentally different than if the light had all been absorbed at the surface. This may seem obvious, but as it had only been presented as a theory in the context of planetary surfaces, with potentially global geophysical consequences (Brown and Matson 1987; Matson and Brown 1989), testing this experimentally seemed worthwhile.

As explained in Chapter 3, glass beads only serve to demonstrate the possibility of a solid-state greenhouse effect. As an analog for an icy satellite surface, they have quite limited applicability. It would be worthwhile to continue this work using real ices, to understand how grain metamorphism will affect the thermal characteristics of the ice, and subsequently the thermal profiles.

References

Brown, R.H., and D.L. Matson 1987. Thermal effects of insolation propagation into the regoliths of airless bodies. *Icarus* **72**, 84.

Buch, V., and J.P. Devlin 1994. Interpretation of the 4141 cm^{-1} (2.415 μm) interstellar infrared absorption feature. *Astrophys. J.* **431**, L135.

Jenniskens, P., and D.F. Blake 1994. Structural transitions in amorphous water ice and astrophysical implications. *Science* **265**, 753.

Laufer, D., Kochavi, E., and A. Bar-Nun 1987. Structure and dynamics of amorphous water ice. *Phys. Rev. B* **36**, 9219.

Matson, D.L., and R.H. Brown 1989. Solid-state greenhouses and their implications for icy satellites. *Icarus* **77**, 67.

Chapter 1. H_2-Rich Interstellar Grain Mantles: An Equilibrium Description

Abstract

Experiments simulating the codeposition of molecular hydrogen and water ice on interstellar grains demonstrate that amorphous water ice at 12 K can incorporate a substantial amount of H_2, up to a mole ratio of H_2/H_2O = 0.53. We find that the physical behavior of ~80% of the hydrogen can be explained satisfactorily in terms of an equilibrium population, thermodynamically governed by a wide distribution of binding site energies. Such a description predicts that gas phase accretion could lead to mole fractions of H_2 in interstellar grain mantles of nearly 0.3; for the probable conditions of WL5 in the ρ Ophiuchi cloud, an H_2 mole fraction of between 0.05 and 0.3 is predicted, in possible agreement with the observed abundance reported by Sandford, Allamandola, and Geballe (1993). Accretion of gas phase H_2 onto grain mantles, rather than photochemical production of H_2 within the ice, could be a general explanation for frozen H_2 in interstellar ices. We speculate on the implications of such a composition for grain mantle chemistry and physics.

1.1. Introduction

Although molecular hydrogen is produced catalytically on grain surfaces in the interstellar medium, the amount of frozen H_2 present in grain mantles is uncertain. The extreme volatility of H_2 qualitatively suggests that very low temperatures are required for an appreciable amount of H_2 to condense on a grain surface. However, if a significant fraction of an icy grain mantle at realistic interstellar cloud temperatures were to consist of H_2, it would have a major impact on grain surface chemistry and gas-grain interactions (see, for example, Allen and Robinson 1976, 1977). The present paper is an extension of experimental work presented earlier (Dissly, Allen, and Anicich 1992), which reported that a large fraction of molecular hydrogen could be incorporated in interstellar water ice grain mantles under typical molecular cloud conditions by codepositional accretion of gas phase H_2 with H_2O. This is important in light of the recent detection of frozen H_2 in interstellar ice in the infrared spectrum of WL5, a deeply embedded protostar in the ρ Ophiuchus molecular cloud complex (Sandford *et al.* 1993).

Much speculation has been made in the past about the possibility of growing H_2 mantles on interstellar grains. Early estimates of the likelihood of H_2 condensation relied on vapor pressure studies (Wickramasinghe and Reddish 1968; Solomon and Wickramasinghe 1969; Lee, Gowland, and Reddish 1971). These results suggested that a thick H_2 mantle was possible only for temperatures $\leq$ 4 K. Subsequent reports have been in terms of the binding energy of H_2 to various surface compositions. As grain surfaces are thought to be covered by an icy mantle composed largely of amorphous water ice (see, for example, Tielens and Allamandola 1987), most studies have specifically addressed the interaction of H_2 with solid H_2O. Early predictions

of the binding energy, E_b, for the physisorption of H_2 to H_2O range from a theoretical estimate of 550 K (Hollenbach and Salpeter 1970) to a higher experimental value of 860 K (Lee 1972), where E_b is given in units of temperature, i.e., energy divided by Boltzmann's constant. The most recent experimental value of the H_2-H_2O binding energy is 555 ± 35 K (Sandford and Allamandola 1993).

The rate of growth of an adsorbed H_2 layer on a grain surface can be predicted by comparing the rate of collision between gas phase H_2 and a grain, assuming a unit sticking efficiency, with the residence time for the H_2 to remain bound to a grain surface. The residence time scale of an adsorbed molecule is described by the Arrhenius expression

$$\tau_{res} \sim \tau_{vib} \exp[E_b/T] , \qquad (1)$$

where T is the grain temperature and τ_{vib} is the vibrational period of the adsorbed molecule in its binding site on the surface (~10^{-13} s for H_2-H_2O; Sandford and Allamandola 1993). For the H_2-H_2O binding energies given above, this expression predicts that H_2 would condense out on grain surfaces for typical interstellar cloud temperatures and H_2 gas number densities. However, the binding energy of H_2 to an H_2 surface is known to be quite small, ~100 K (Lee 1972). For this low value of the binding energy, the residence time scale for H_2 is substantially shorter than the collision time scale for conceivable interstellar conditions. Thus the growth of a pure H_2 mantle is self limiting, as the binding energy of H_2 to the grain surface will decrease as the H_2 coverage increases. The point at which an equilibrium coverage occurs for given interstellar conditions is quite sensitive to the H_2 surface binding energy to the water ice. Estimates of this equilibrium

coverage range from an H_2 layer a few monolayers thick (Lee 1972) to a single H_2 monolayer covering only ~20% of the grain surface (Govers, Mattera, and Scoles 1980; Tielens and Hagen 1982).

As a variation on the theme of condensation, H_2 may accumulate in the mantle at a significant level as it coaccretes with other mantle species, such as H_2O. This is a more realistic model of mantle growth, as species will collide with grain surfaces at rates proportional to their respective gas phase abundances. Previous codepositional experiments of H_2 with H_2O showed that the amount of hydrogen incorporated in a water matrix could be substantial, with a mole ratio of H_2/H_2O as high as 0.63 (Laufer, Kochavi, and Bar-Nun 1987). This result suggests that H_2 may be a significant component throughout the volume of an icy grain mantle, and not just on the grain surface.

Accretion of H_2 from the gas phase is not the only way to incorporate molecular hydrogen into an icy grain mantle. Recent experiments have shown that molecular hydrogen can be chemically produced and subsequently trapped within icy mantles comprised of species that are rich in hydrogen, such as H_2O or CH_3OH, by either cosmic ray bombardment (Moore and Hudson 1992) or by ultraviolet photolysis (Sandford and Allamandola 1993). The latter UV experiments have shown that, for laboratory ice mixtures thought to typify interstellar grain mantle compositions, the fractional abundance of H_2 relative to H_2O saturates at ~0.35. In addition, the product H_2 is apparently either trapped or bound strongly enough in the ice that it does not effectively sublimate below 30 K, and can be detected in the ice mixture even at temperatures as high as 70 K.

A more detailed understanding of the relative importance of the different physical processes that may result in the incorporation of H_2 in

amorphous water ice is needed to properly model the composition of grain mantles in various interstellar environments. To that end, this paper reports the results of an experimental investigation of the composition and physics of ice samples prepared by codepositing amorphous water ice with an excess amount of H_2. We conclude that codepositional accretion of H_2 is a possible general mechanism for incorporating large amounts of molecular hydrogen in interstellar icy grain mantles.

1.2. Experimental Procedure

For this report, we have utilized an experimental arrangement similar to that described elsewhere (Allamandola, Sandford, and Valero 1988). Briefly, the apparatus consists of two differentially pumped chambers, which are each evacuated by a turbomolecular pump (Balzers TPU 170) to a background pressure of ~3 x 10^{-8} torr. Extending into the first chamber is a closed cycle helium refrigerator (Air Products Displex DE-202), which can be cooled down to 12 K. Attached to the end of the refrigerator is a sapphire window. The temperature of the window can be varied from 12 K to room temperature, with an accuracy of ± 0.2 K, by a resistive heater at the base of the window, monitored by a gold-chromel thermocouple and maintained by a temperature control system (Scientific Instruments Series 5500). Ice samples were prepared by simultaneously spraying H_2 and H_2O from separate gas lines slowly onto the cooled window. The twin pinhole nozzles are each 0.06 mm in diameter, set identically 4.0 cm away from the window, so that the substrate is exposed to the same distribution of gas from each nozzle. The composition of each ice sample was characterized upon heating by a

quadrupole mass spectrometer (Extrel), housed in the second, adjacent vacuum chamber. Transmittance spectra were taken of the ice samples with a Fourier Transform Infrared Spectrometer (Mattson Cygnus 25) between 2000 and 5000 cm^{-1} at a resolution of 1 cm^{-1}.

Recent experimental work on the structure of vapor-deposited amorphous water ice indicates that the surface area of the ice is highly dependent on the deposition conditions (Mayer and Pletzer 1986). Consequently, we tried to control our deposition parameters to simulate the interstellar accretion of icy mantles as closely as possible. The structure resulting from the slow growth of interstellar ice mantles can effectively be reproduced in the laboratory using depositions with a Knudsen number > 1 (K_n = ratio of mean free path of gas in reservoir to nozzle diameter). This gives depositional flow in the molecular rather than supersonic regime. The resulting low growth rate yields an amorphous ice with a high surface area, due to a microporous structure with pore sizes typically < 20 Å (Mayer and Pletzer 1986). Our experimental nozzle backing pressures ranged from 0.033 to 0.2 torr for H_2O, and 0.8 to 1.2 torr for H_2, assuring that $K_n > 1$ for both H_2 and H_2O in all our depositions. The highest deposition rate of H_2O was approximately 0.5 μm/hr (~ $5x10^{14}$ H_2O molecules/cm^2/sec), measured by monitoring the interference fringes from a HeNe laser reflected from the growing sample, discussed in greater detail in Appendix A of Chapter 2. Our ice samples were transparent, indicating no structure within the ice larger than ~1000 Å.

Depositions were carried out for several window temperatures between 12 and 30 K. Ice sample abundances were varied by changing either the deposition duration, or the deposition rate, or both. Deposition times ranged between 20 minutes and 2.5 hours. To assure that the relative gas collision

rate of H_2 with the growing ice was greater than that of H_2O, as is the situation in interstellar molecular clouds, ice samples were prepared with relative gaseous H_2:H_2O inlet pressures of between 4:1 and 36:1. The slow deposition of water did not affect the ambient pressure in the chamber, indicating that most of the input water molecules immediately condensed out on the window. This was not the case with the input of H_2. Admission of H_2 into the vacuum chamber raised the chamber pressure from the background of ~3 x 10^{-8} torr to ~1 x 10^{-5} torr. The deposition of an ice sample can then be viewed as the growth of H_2O in the presence of a surrounding 10^{-5} torr atmosphere of H_2.

Once the deposition was completed, the sample was allowed to sit ~10 minutes, until the pressure in the chamber had dropped and re-equilibrated. The sample was then heated, typically at a rate of 2 K/min. The evolved gases were monitored with the mass spectrometer, calibrated to the absolute partial pressures of both H_2 and H_2O. We derived the rate of gas release from the sample with the following formula,

$$\text{Desorption Rate [molec/min]} = \text{Pumping speed [l/min]} * \text{Number density [molec/l]}, \qquad (2)$$

with the number density of each gas determined from the mass spectrometer reading, and pumping speeds (100 l/s for H_2O, and 66 l/s for H_2) given by the pump manufacturer. Integrating this rate over the time it took for the entire ice sample to sublimate gave the total abundance of H_2 and H_2O in the sample.

Care was taken to account for the cryopumping of water ice from our samples onto the cold refrigerator column above the window during the

sample heating. This was done by observing the ratio of chamber pressures due to the injection of water with the full system at room temperature, versus the system with the refrigerator cold, but with a window temperature of 200 K, so that no ice would condense directly on the window. This calibration procedure was repeated several times, giving a ratio of warm/cold of 6.4 ± 0.1, meaning that the large majority of water molecules liberated during the sample sublimation condensed out on the upper refrigerator column. The amount of water seen by the mass spectrometer was thus underrepresented by a factor of 6.4 ± 0.1, so our water measurements were scaled by this amount to give the total amount of water in the ice samples. The same procedure indicated that the cryopumping of H_2 is negligible.

1.3. Results

In our initial experiments, the sapphire window onto which the ice samples were deposited was cooled to 12 K, a typical dark cloud grain temperature. The ice samples were prepared with relative gaseous H_2:H_2O inlet pressures of between 4:1 and 36:1, as described in the experimental section. The total abundances of H_2 and H_2O for each ice sample prepared, found by integrating under the desorption profiles for each species during sample heating, are summarized in Figure 1.1. It is immediately evident that the amount of hydrogen in our samples correlates with the total amount of water in the sample. A linear regression through the data yields a best fit for the ratio H_2/H_2O of 0.53. Given our uncertainties, this is in good agreement with the H_2/H_2O value of 0.63 found in the codepositional experiments of Laufer *et al.* (1987), although their deposition rates were significantly faster

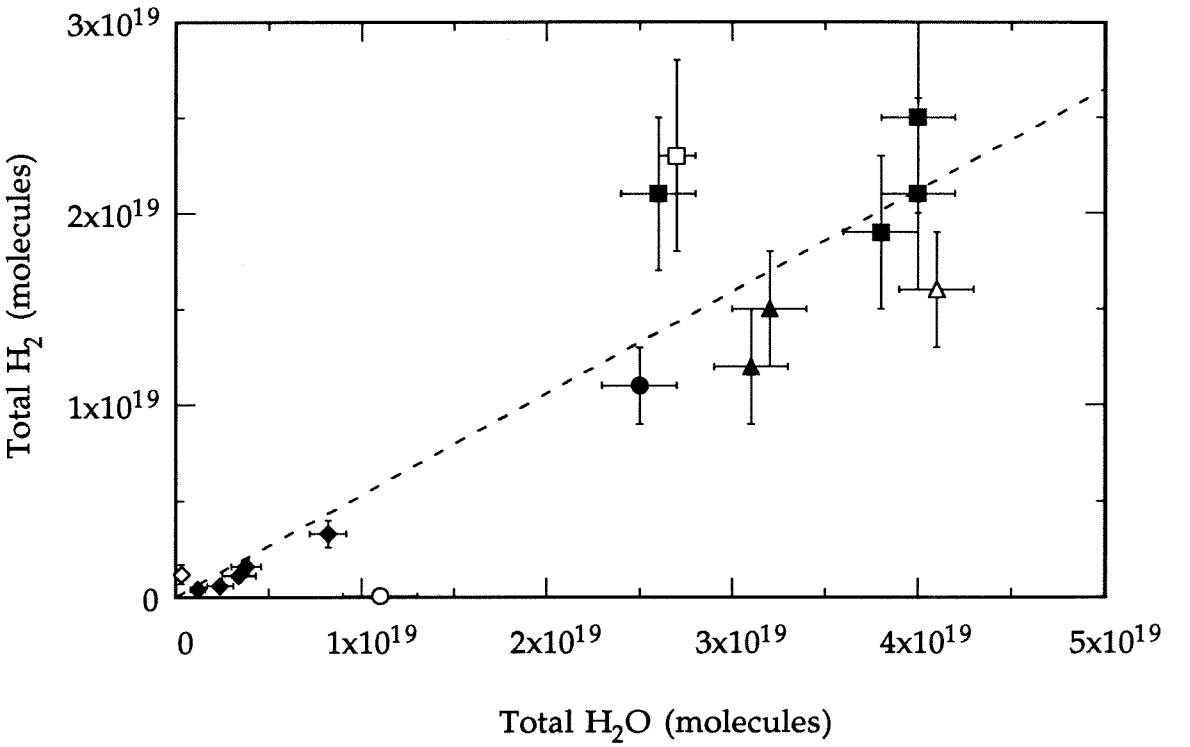

Figure 1.1. The total abundances of H_2 and H_2O in ice samples deposited on a sapphire substrate cooled to 12 K, prepared with H_2:H_2O gaseous inlet pressures of 0.8:0.2 torr (solid triangles, 70 minute deposition time), 1.2:0.2 torr (solid squares, deposition times between 1.5 and 2.5 hours), 1.2:0.1 torr (solid circle, 2.5 hour deposition time), and 1.2:0.033 torr (solid diamonds, deposition times between 20 minutes and 2.5 hours). In addition, there were 1 hour depositions solely of H_2O (open circle) and solely of H_2 (open diamond). Two identical depositions were carried out (H_2:H_2O gaseous inlet pressures of 1.2:0.2 torr, 1.5 hour deposition time); however, in one (open triangle) the ice sample was allowed to sit in the chamber for several hours after deposition while H_2O cryopumped from other parts of the vacuum chamber onto the sample, and in the other (open square) the sample was allowed to sit several hours, but now under an atmosphere of 10^{-5} torr of H_2 maintained in the chamber. The dashed line shows the best fit for the ratio H_2/H_2O of 0.53.

than ours. Although the different ice samples were prepared with relative H_2:H_2O gas inlet rates that varied by almost a factor of ten, the H_2/H_2O ratio in our experiments did not depend on this ratio in any systematic way, suggesting that the maximum amount of hydrogen that can be incorporated in the ice is quickly reached for a small excess of H_2 over H_2O.

Depositing only H_2 onto the 12 K window for 1 hour yielded very little hydrogen upon heating (Fig. 1.1, open diamond), confirming that H_2O ice is the substrate responsible for the H_2 binding. A similar 1 hour deposition of pure H_2O also produced negligible H_2 when the ice was heated (Fig. 1.1, open circle), demonstrating that the H_2 detected in our experiments is not a decomposition product of the H_2O in the ionizing region of the mass spectrometer. The error bars associated with each measurement are due to both uncertainty in the calibration of the mass spectrometer to an absolute pressure for both H_2 and H_2O, and the uncertainty in choosing the baseline for integration under each desorption profile. Residual water and hydrogen in the system over the course of the experiments made repeatability difficult, as reflected by the scatter of the data.

Since the ice samples were grown on the coldest point of the refrigerator, we were concerned about the possibility of H_2O cryopumping onto our sample from other parts of the chamber during the sample desorption, and perhaps affecting the measured ratio in the process. We therefore ran two control experiments: letting the ice sample sit in the chamber for several hours under vacuum at the end of the deposition (Fig. 1.1, open triangle), and letting the sample sit for several hours after the deposition under a 10^{-5} torr atmosphere of H_2 (Fig. 1.1, open square). This waiting period was hopefully long enough so that the cyropumping of additional H_2O on our sample would have become negligible. The former

run represents the lowest extreme of H_2/H_2O in our codeposited samples, suggesting that some cryopumping of H_2O was occurring after the deposition had ended. The latter experiment alternatively yielded the highest H_2/H_2O ratio of our codepositions, as even the cryopumped water was deposited under a large excess of H_2. Consequently, the brief waiting period between the end of deposition and the beginning of desorption in all our other experiments may have resulted in a final layer of deposited H_2O not saturated with H_2. Therefore, our derived fit of $H_2/H_2O = 0.53$ may be a lower limit to the true saturated value at 12 K.

The typical temperature programmed desorption (TPD) profiles for both H_2 and H_2O are shown in Figure 1.2, for depositions at window temperatures of 12, 20, and 30 K. For each ice sample, the hydrogen and water mixtures were deposited at the same rate (inlet nozzle backing pressures of 0.8 and 0.2 torr, respectively), and for the same duration (70 minutes), and in each case the heating progressed at a steady rate of 2 K/min. The total amount of H_2 and H_2O in our samples was found by integrating under the desorption curves. The fractions of H_2 in each sample for the different deposition temperatures (normalized to the value at 12 K) are 12:20:30 K ~ 1:0.37:0.04, showing a significant decrease with increasing substrate temperature. Close inspection of the H_2 desorption profile for the 12 K deposition shows two distinct regions: a low temperature component, represented by the large peak below ~30 K in which the majority (~80%) of the total hydrogen leaves the sample, and a high temperature component, represented by the broad plateau of a lower hydrogen liberation rate from ~30 - 80 K. The 20 K deposition has a similar structure, although less total H_2.

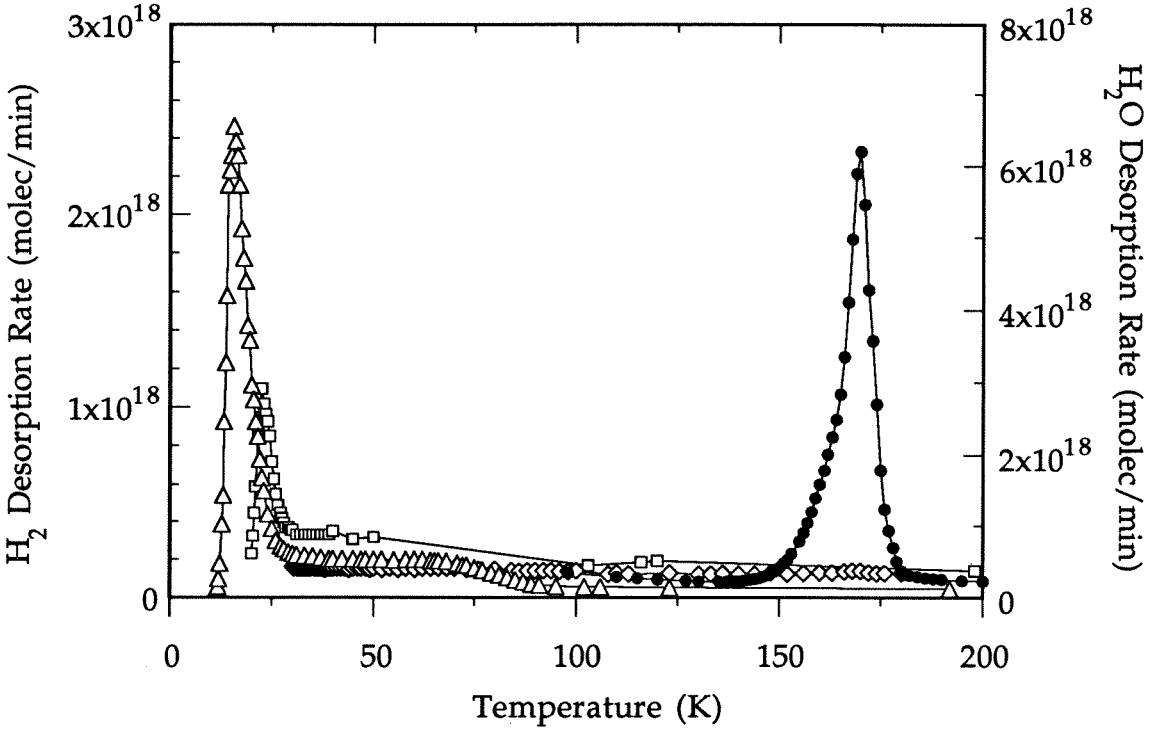

Figure 1.2. Desorption profiles for H_2 and H_2O during heating of ice samples at a steady rate of 2 K/min. Ice samples were prepared under identical conditions (see text), but at different window substrate temperatures. Shown are H_2 desorption profiles for window temperatures of 12 K (open triangles), 20 K (open squares), and 30 K (open diamonds) and the desorption profile of H_2O from the 12 K deposition (solid circles). Lines between markers serve only to aid visualization, and do not represent actual data. The H_2 desorption profiles for the 20 K and 30 K depositions were normalized by setting the H_2O abundance from these samples equal to that of the water abundance in the 12 K deposition.

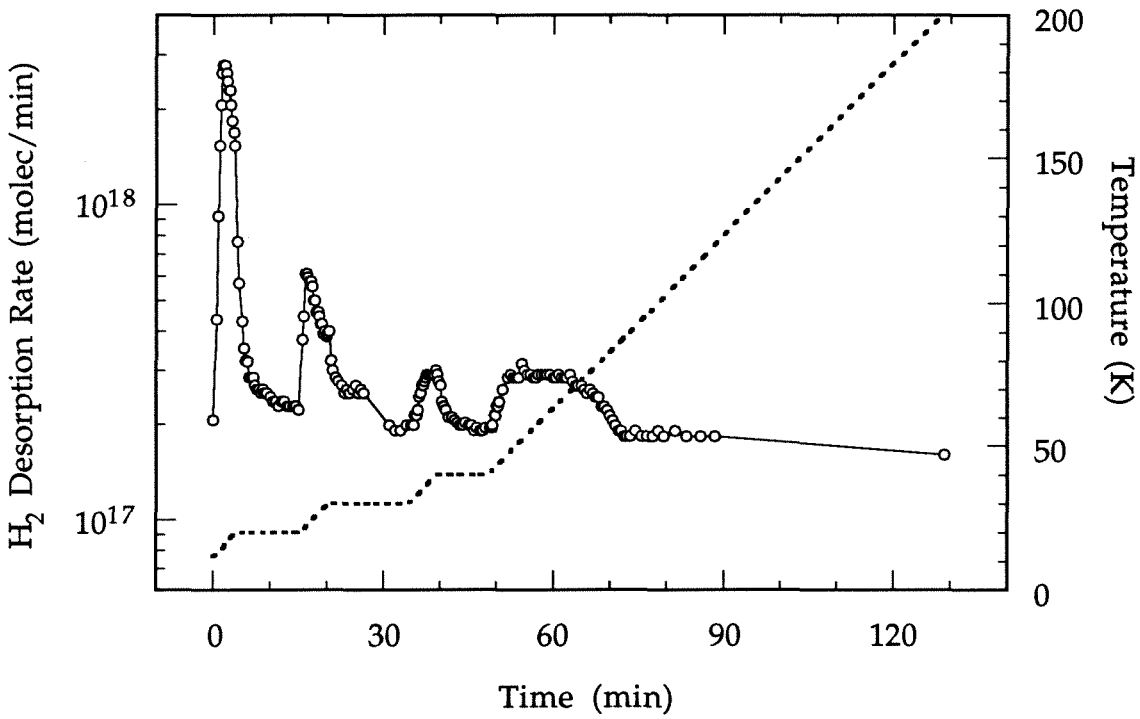

Figure 1.3. H_2 desorption profile (open circles) for a temperature programmed desorption experiment. The heating profile is indicated by the dashed line. The H_2/H_2O ice mixture was prepared under the same conditions as the experiments shown in Fig. 1.2, with a window temperature of 12 K. Again, the line between markers serves only as a visualization aid.

Our desorption profiles are similar to results reported previously (Laufer *et al.* 1987; Sandford and Allamandola 1993). We will contrast the explanations for the structure in the profiles later in this paper.

To investigate whether the high temperature component of the 12 K deposition shown in Figure 1.2 was not simply due to the time-delayed diffusion of unbound hydrogen from deeper layers in the ice, we performed the TPD experiment shown in Figure 1.3. The deposition conditions were identical to those given for the depositions in Figure 1.2. The ice sample was heated at the rate of 2 K/min, except when the temperatures were 20, 30, and 40 K, at which times the temperature was held constant for approximately 10 minutes to allow for the complete release of any labile H_2 in the sample volume. During the 10 minute temperature holds, the H_2 release rate dropped quickly to the background level. When we resumed increasing the sample temperature, the H_2 release rate immediately returned to the value when the increase in temperature was halted. We conclude from this that time-delayed solid-state diffusion of deeply bound H_2 is not significant. In fact, diffusion may not be the factor controlling the release of H_2 from the ice at all. Our results are consistent with the H_2 stable in the water ice at high temperatures. If this is true, then the respective areas under each temperature interval represent the amount of H_2 stably bound within that interval. The fractions of H_2 left in the water ice at each temperature are (again, normalized to the value at 12 K): $T > 12$ K, 1.0; $T > 20$ K, 0.37; $T > 30$ K, 0.19; and $T > 40$ K, 0.15.

Previous authors have reported an induced H_2 vibrational feature at 4137 cm^{-1} (Hixson *et al.* 1992; Sandford and Allamandola 1993) for frozen H_2-H_2O mixtures. We did not detect any spectral features in this region of our transmittance spectra. As our samples were only ~0.5 μm thick, such a feature

would be quite weak. We assign an upper limit to the integrated band absorbance $A < 1.8 \times 10^{-19}$ cm/molecule for any feature at or near 4137 cm^{-1}. This is done by correlating the measured H_2/H_2O ratio in our samples with the integrated absorbance of the observed 3.1 μm water ice peak. This is consistent with a previous estimate of the integrated absorbance for the H_2 band of $A > (9.4 \pm 0.9) \times 10^{-20}$ (Sandford and Allamandola 1993).

1.4. Physical Description of H_2 Incorporation in Water Ice

The recent detection of molecular hydrogen in interstellar ices raises a fundamental question: to what extent is the detected H_2 a product of the irradiation of an ice of hydrogen containing compounds such as water or methanol, or simply the result of ambient gas phase H_2 incorporated during the growth of grain mantles in the molecular cloud? Taken at face value, our laboratory results would suggest that codepositional adsorption alone could yield H_2 as a major component in interstellar grain mantles. However, the experimental conditions and time scales in our laboratory are quite different than those in the interstellar medium. To properly assess how our results can be applied to interstellar grain mantles, we need a thorough understanding of the physical processes that govern the adsorption and growth of the ice samples in our experiments.

As shown previously in equation (1), the residence time scale for H_2 to remain in a physisorption site is governed by the binding energy, E_b. Theoretical and experimental values of the binding energy of H_2 to H_2O ice, typically in the context of surface adsorption, were given in the introduction. However, these reports each provide only a single "average" value for the

surface binding energy. In actuality, an amorphous ice has an irregular surface with physisorption sites having a *distribution* of binding energies. A recent computational study by Hixson *et al.* (1992) predicts what such a distribution might look like, determined by finding the potential minima of an isolated H_2 molecule on the model surface of an amorphous ice water cluster. The model provides a limited description of our experimental ices, as the surface potentials of a cluster can only approximate those of a macroscopic solid. In addition, the model does not take into account either the effects of the adsorbed H_2 on the structure of the water cluster or the adsorbed H_2-H_2 interaction. Still, it does yield values for the H_2 surface binding energies that are reasonable in the context of previous theoretical and experimental reports. For a cluster of 450 water molecules, 240 possible surface binding sites for H_2 were found, with binding energies ranging in value from 320 K to 1399 K, with a peak in the population distribution at 650 K. In this theoretical distribution, 650 K is the most likely value for the binding energy. This is what the previous list of reported single-valued surface binding energies represents. The agreement between the peak of the theoretical distribution and the reported experimental values of 555 ± 35 K given by Sandford and Allamandola (1993) is good, given the limitations of the model calculation.

How might the concept of a distribution of binding site energies modify our thinking about H_2 incorporation in ices? The standard description of a single value for the surface binding energy predicts a uniform residence time scale for a given adsorbed species. An ice surface that has a distribution of binding site energies will have a corresponding distribution of residence time scales. Given a collision rate of an adsorbable species like H_2, this distribution will dictate an equilibrium surface population such that sites with $\tau_{res} > \tau_{col}$ will always be filled by H_2, assuming that the sticking probability of an H_2

molecule with a grain surface is unity. The collision time scale for an H_2 molecule to encounter a particular binding site is given by

$$\tau_{col} \sim [n(H_2)_{gas}\, \sigma_{site}\, v_{gas}]^{-1}. \quad (3)$$

Equating (1) and (3) for a constant gas-phase collision rate and grain surface temperature gives a critical value of E_b such that all sites with $E_b > E_b(crit)$ will always be filled by H_2 molecules.

This simple calculation actually provides an upper limit to the value of $E_b(crit)$, as it only takes into account impinging gas phase H_2 as the source for molecular hydrogen. An additional source of H_2 is on the surface of the ice itself, as an adsorbed H_2 molecule is more likely to migrate over the surface than escape it completely. This is due to the fact that the kinetic barrier to migration to a neighboring site is roughly half the value of E_b, the barrier to escape from the surface (Tielens and Hagen 1982). One can then imagine a sort of "musical chairs" of H_2 among surface binding sites, with stronger sites preferentially occupied over weaker sites. Migration from weaker sites to their stronger counterparts provides a flux of H_2 to strong sites in addition to the gas phase flux, which will lower the level of the critical binding energy from that found with gas phase adsorption as the sole source of H_2.

The results shown in Figure 1.3 provide a test of whether the incorporation of H_2 in our laboratory ices can be described by such an equilibrium physical model. By assuming that the H_2 release in this TPD experiment is controlled only by thermodynamic equilibrium, an experimental distribution of H_2 binding site energies can be inferred. The value of $E_b(crit)$ for each of the temperature holds at 20, 30, and 40 K, and the initial temperature at 12 K can be found as outlined above, by equating the H_2

collision rate with the residence time scale at that temperature. Since we are assuming that the ice sample is always in equilibrium, the collision rate of H_2 is dictated by the background pressure of H_2 when the sample is being heated, rather than the H_2 pressure during deposition. As the background pressure was ~3 x 10^{-8} torr, the H_2 number density was ~1 x 10^9 cm^{-3}. Thus, with a typical binding site size of 10^{-15} cm^2, and with a gas temperature of 300 K, τ_{col} ~ 5 seconds for an H_2 molecule to collide with an individual surface site under the background pressure. If we then take this 5 seconds as the residence time scale, and an ice temperature of 12 K, solving for E_b(crit) gives 380 K. Therefore, when our ice sample is sitting under a background pressure of H_2 at 12 K, all H_2 in binding sites with E_b > 380 K will have a longer residence time than it takes for a new H_2 molecule to find and occupy that site, and will always be filled by H_2. If the H_2 population of our ice samples is truly governed by this equilibrium model, then only hydrogen in those binding sites with E_b < E_b(crit) will be labile at a given temperature hold in the TPD experiment. Repeating this simple procedure, the fraction of H_2 left in the water ice at 12, 20, 30, and 40 K then yields the relative number of sites in our sample with E_b > E_b(crit) for each of these temperatures.

The experimentally inferred relative distribution of binding sites with E_b greater than a given value from the Figure 1.3 TPD experiment are compared in Figure 1.4 with the results of the theoretically computed distribution by Hixson *et al.* (1992). Because the 12 K ice sample was allowed to sit for several minutes under the background pressure of H_2 immediately after the deposition, hydrogen in sites with E_b < 380 K escaped the sample before the measurements were started, so the experimental distribution is

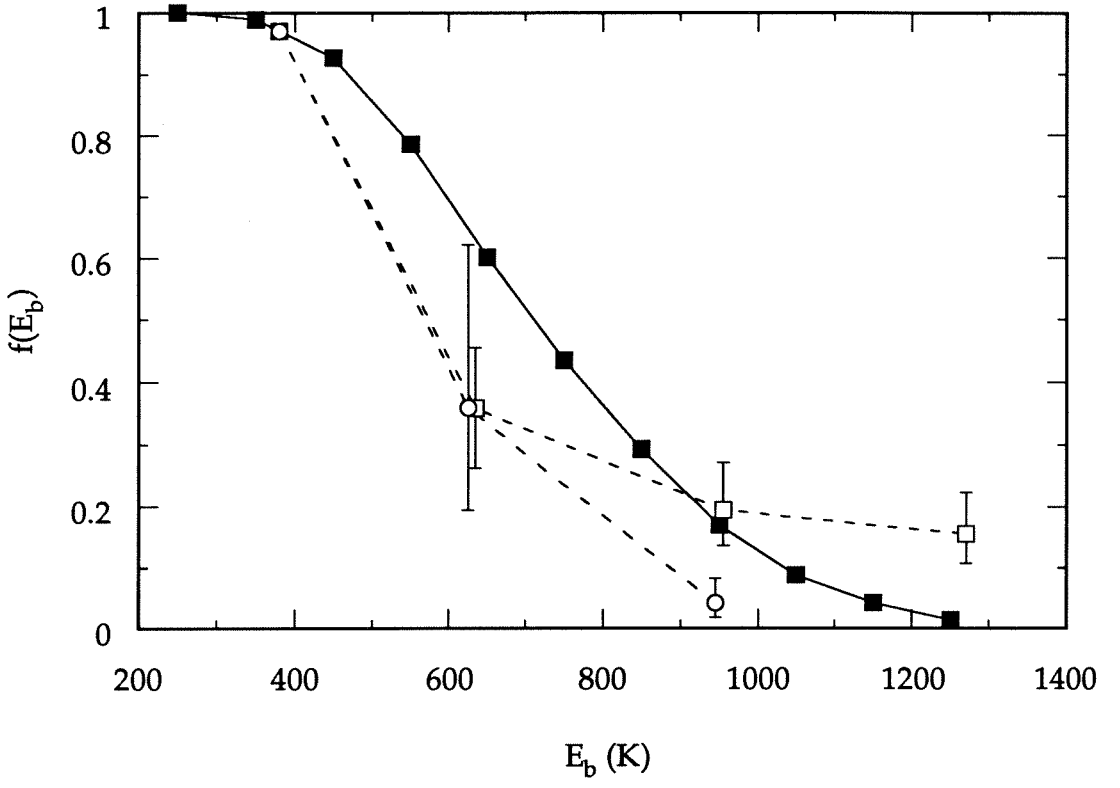

Figure 1.4. Comparison of our experimental results with a theoretical distribution of surface binding site energies, given by Hixson *et al.* (1992). Values are presented as $f(E_b)$, the fraction of sites with E_b greater than a given value: the theoretical distribution (solid squares), the distribution of H_2 binding site energies derived from the TPD experiment shown in Fig. 1.3 (open squares), and a similar distribution inferred from the results for depositions at 12, 20, and 30 K shown in Fig. 1.2 (open circles). Errors were determined relative to the normalized abundances at 380 K, the minimum value of binding energy for H_2 that we could feasibly detect (see text). Again, lines between markers serve only as a visualization aid.

normalized to the theoretical one at 380 K. The approximate agreement between the two distributions supports the physical picture of H_2 incorporated in the ice by the equilibrium distribution outlined above.

This physical model is applicable to ices deposited at temperatures above 12 K as well. This is shown by displaying in Figure 1.4 the relative amounts of H_2 in the samples deposited at 12, 20, and 30 K, discussed previously with reference to Figure 1.2. This data curve is normalized to the theoretical curve as before. Again, the relative abundances of the total H_2 in ices deposited at different temperatures is consistent with an equilibrium distribution of binding site energies, although the experimental curve falls consistently below the theoretical estimate of Hixson *et al.* (1992). A possible explanation for this discrepancy is that the theoretical curve gives energies that are slightly too high for real ice mixtures, as one would intuitively expect from the lack of an H_2-H_2 interaction potential in the model. This would suggest that the peak of the theoretical distribution at E_b = 650 K is also too high; it may in actuality be closer to the 555 K experimental estimate of Sandford and Allamandola (1993).

Figure 1.4 shows additional interesting information. Although the overall fit of the theoretical distribution to the data is fair, the TPD experiment from Figure 1.3 shows a definite high energy tail, suggestive of H_2 from deeply buried sites not predicted by the theoretical surface model. These buried sites only appear to account for ~20% of the total number of sites, when compared to the theoretical distribution. As mentioned previously, the desorption profiles for the 12 K depositions, as shown in Figure 1.2, consist of two distinct regions with relative sizes that appear to be independent of the sample thickness: the main low energy peak, and a smaller, higher energy plateau. The plateau region accounts for ~20% of the total liberated H_2 in our

12 K deposited desorption profiles as well, suggesting that it is due to the desorption from deeply buried sites. The desorption profiles of very thin (~100 Å) ice samples (not shown) are a notable exception, as the plateau region appears to decrease in relative size as the samples decrease in thickness, although the H_2 desorption signal is very weak for samples this small. We therefore suggest that the primary peak in the H_2 desorption profile is due to the liberation of surface or near surface H_2, in equilibrium with the gas phase, controlled by a distribution of binding energy sites similar to the theoretical one. The plateau is apparently due to deeply buried H_2, either physically trapped in the water ice matrix or strongly bound by very energetic sites not described in the theoretical surface distribution by Hixson *et al.* (1992). Thus, in our experiments, ~80% of the H_2 population is adequately described by the theoretical surface binding energy distribution, while ~20% is apparently due to H_2 buried deeply within the H_2 matrix. This is consistent with the results of the photochemical experiments by Sandford and Allamandola (1993). As the H_2 in their experiments was primarily produced deep within the volume of the ice rather than on or near the surface, this would explain their report that the total abundance of H_2 in their ice samples did not change significantly for temperatures less than 30 K. Our finding that this non-equilibrium H_2 is released from the ice at temperatures as high as 70 K is also consistent with their report.

The difference in the distribution between the two experimental curves in Figure 1.4 suggests that the amount of H_2 in the ice when it was deposited at 12 K and then raised to a certain temperature is systematically higher than when the ice is actually deposited at that same temperature. This difference may also be due to the burial of H_2 into deeper, more strongly bound sites. This is not surprising, as the 12 K deposition has a higher equilibrium surface

abundance than a higher temperature deposition, allowing proportionally more H_2 to be buried into the non-equilibrium population as the water ice is growing.

It is interesting that the desorption profiles for a given deposition temperature appear to be independent of sample thickness, at least for samples > 100 Å in thickness. One would expect that if the profile has distinct regions that are due to separate surface and volume populations, the relative size of the volume contribution would increase as the sample thickness increased. The fact that it does not suggests that the distribution of sites is in fact a characteristic of the entire ice sample. This is potentially consistent with an ice that is highly microporous, like the structure of a sponge, so that the "surface" does in fact dominate the population for all our experimental thicknesses. If amorphous water ice has such an open structure, adsorbed molecules in the volume of the ice would be in equilibrium with those in the gas phase. As such, H_2 molecules would freely migrate between the gas phase and the porous ice volume until finding a vacant binding site. We tried to test this experimentally, with a sequenced deposition of H_2O and H_2. The deposited H_2O was allowed to sit for several hours so that the cryopumping of H_2O had effectively stopped. The H_2 was then deposited on this water substrate. Our results suggest that to within a factor of two, this gives the same H_2/H_2O ratio as our codepositional experiments. However, the results of this sequence experiment were not as clear or reproducible as our other experiments. We hope to repeat this set of experiments in the near future, to properly assess the nature of the amorphous ice surface.

A previous explanation for the temperature-dependent release of H_2 from a water ice matrix has been put forward by Laufer *et al.* (1987). They concluded that the H_2 is physically trapped in the water ice during

codeposition. As the water ice matrix is heated, this opens the ice structure in a steady and repeatable way, which controls the release of trapped H_2. This would imply that the population of trapped H_2 is dictated by conformational changes in the water only. Large trapped abundances are then probably an artifact of the fast laboratory deposition rates. This would suggest that accretional trapping in the volume of the ice is a minor effect under interstellar conditions. *Our intent is to offer the alternative explanation that a significant population of H_2 in ice samples may be an equilibrium condition, controlled primarily by the thermodynamic behavior of a simple distribution of binding site energies.* With such a model, interstellar grains may contain a substantial fraction of H_2, discussed in more detail below.

1.5. The H_2 Abundance in Interstellar Grain Mantles

The amount of H_2 incorporated in interstellar grain mantles dominated by water ice can be derived from this physical model of an equilibrium between gas phase H_2 and the grain binding site energy distribution. Utilizing the concept of a critical binding energy, the respective gas-grain collision frequencies under laboratory and interstellar conditions allow a direct comparison of the population of adsorbed H_2 in these two environments. Following the procedure outlined above to determine the critical binding energy of an ice surface at a given temperature and under a given number density of H_2, we can estimate this value for various interstellar conditions, where molecular hydrogen also dominates the available gas phase speciation, typically by several orders of magnitude. E_b(crit) then fully determines the equilibrium mole fraction of bound H_2 for

the grain mantle. For example, at reasonable molecular cloud values of T = 10 K and $n(H_2) = 10^4$ cm^{-3}, E_b(crit) ~ 450 K. For this value, the equilibrium population of H_2 will fill over 90% of the available surface sites in the theoretical surface distribution of Hixson *et al.* (1992). As we postulate that ~80% of the desorbed H_2 in our experiments is due to a similar equilibrium population, and that the total H_2/H_2O ratio in our samples is 0.53, we estimate that interstellar grains have an H_2/H_2O ratio as high as ~(0.9)(0.8)(0.53) ~ 0.4. The equilibrium mole fraction of H_2 in a grain mantle dominated by H_2 and H_2O (i.e., $H_2/(H_2 + H_2O)$) would then be ~0.3. Adding any deeply buried, non-equilibrium H_2 will only raise this abundance. Figures 1.5 (a) and (b) summarize the calculated values of E_b(crit) and the corresponding predicted fractional abundance of H_2 in grain mantles for different values of interstellar gas-grain temperature and gas phase H_2 number density. For comparison with the interstellar results, the derived values of E_b(crit) and fractional H_2 abundances from our codeposition experiments with different substrate temperatures are also shown in Fig. 1.5 (a). Note that at low temperatures in particular, the higher gas phase densities in the laboratory relative to typical interstellar conditions do not lead to significant differences in the equilibrium fractional H_2 abundances, as E_b(crit) is not a sensitive function of gas phase number density. Thus in the context of the equilibrium model, our laboratory provides a reasonable simulation of the interstellar environment.

This equilibrium model may adequately describe the observed interstellar frozen H_2 abundance along the line of sight of WL5 in the ρ Oph molecular cloud (Sandford *et al.* 1993). WL5 is a deeply embedded infrared source ($A_V \geq 50$), with local number densities thought to be in the range of 10^4 - 10^6 cm^{-3} (Wilking and Lada 1983). The detection of CO frozen in nonpolar

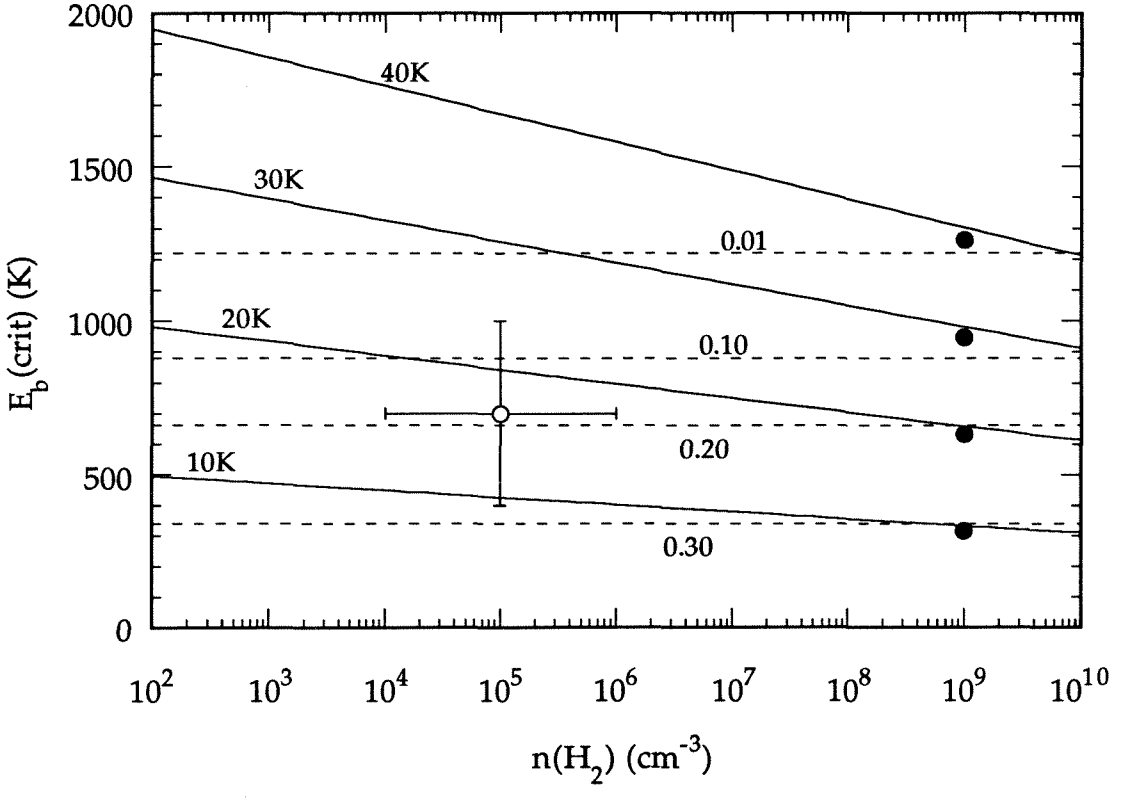

Figure 1.5 (a). Critical binding energies and equilibrium fractional H_2 abundances in interstellar grain mantles for different H_2 gas phase number densities and gas-grain temperatures. The solid lines show calculated E_b(crit) values at 10, 20, 30, and 40 K. The H_2 mole fractions of 0.01, 0.1, 0.2, and 0.3 are indicated (dashed lines) for the appropriate values of E_b(crit). The open circle represents the value of E_b(crit) computed for the conditions in the cloud containing WL5, as described in the text. The filled circles show E_b(crit) for laboratory conditions at a background pressure of ~3×10^{-8} torr and ice temperatures of 12, 20, 30, and 40 K. Their slight offset from the isothermal lines is due to E_b(crit) being determined for a 300 K gas phase temperature.

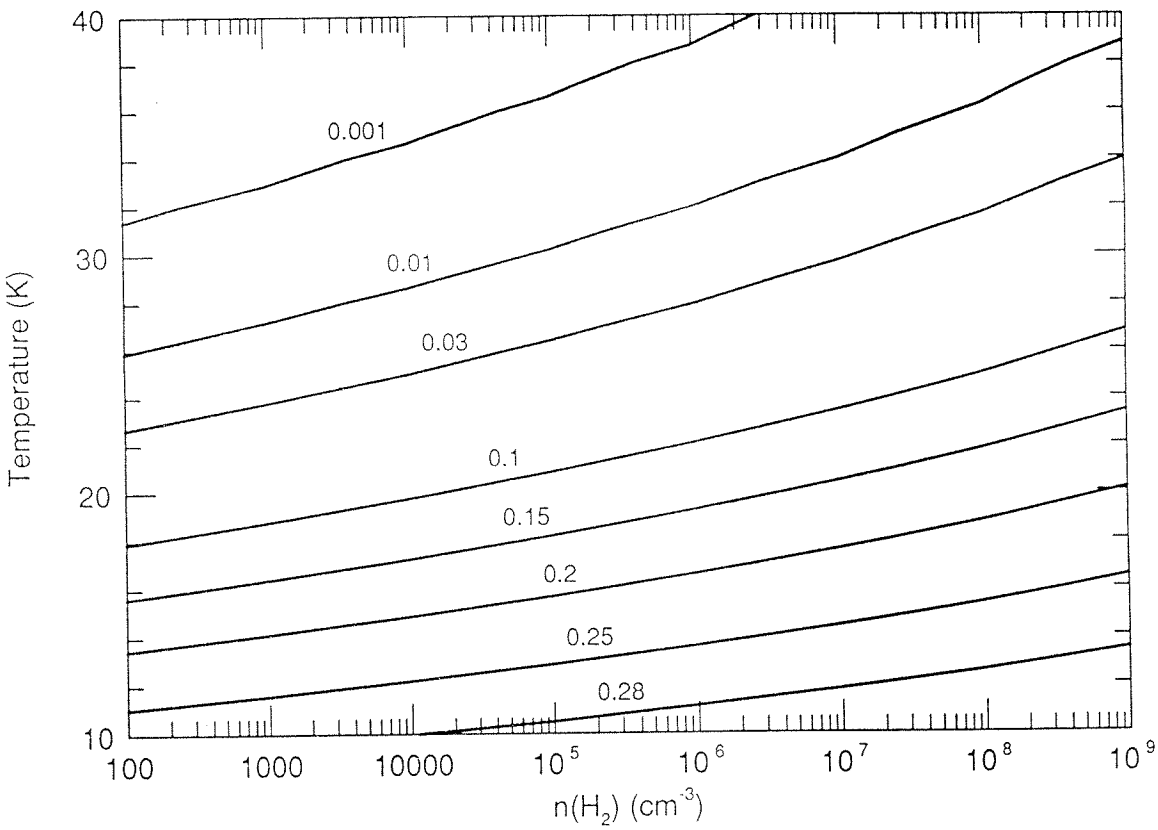

Figure 1.5 (b). Contours of predicted H_2 fractional abundance (H_2/total) in interstellar grain mantles, in terms of the gas phase H_2 number density and the temperature, taken to be the same for both gas and grains. This figure is an alternative way to view the information plotted in Figure 1.5 (a).

matrices along this line of sight (Kerr, Adamson, and Whittet 1991) indicates that temperatures are probably in the range of 10 - 25 K. Plotting this range of conditions in Fig. 1.5 (a), we predict that grain mantles along this line of sight would have H_2 mole fractions from 0.05 to almost 0.30. Unfortunately, an observational determination of the ratio of H_2 to total ice molecules toward WL5 has not been made. The column abundance of water ice along this line of sight is uncertain, as the observed water ice feature at 3.1μm is saturated (Tanaka *et al.* 1990). However, the ice phase H_2/CH_3OH ratio has been determined to be ≤ 0.08 (Sandford *et al.* 1993). If the H_2O/CH_3OH ratio is ~2 - 3, as it is for ices in other similar interstellar environments, and as these two species likely dominate the composition of most grain mantles (Allamandola, Sandford, and Tielens 1992), this would put the fractional abundance of H_2 along this line of sight at the few percent level, consistent with the lower end of our predicted range.

If this equilibrium model is correct, molecular hydrogen in interstellar grains would be a widespread phenomenon. Ultraviolet photoprocessing would not be a requirement to explain the presence of frozen H_2 in interstellar ices. We suggest, then, that interstellar grains may have a significant fractional abundance of H_2 (~30% of the total number density) at 10 K temperatures even in unilluminated regions of molecular clouds. The presence of H_2 as a product of photolysis in the ice would be a special case limited only to regions with a significant UV flux. More observations of the frozen H_2 feature along other lines of sight with widely varying UV radiation budgets are needed to adequately test the relative importance of UV photoprocessing versus gas phase accretion.

Significant quantities of molecular hydrogen incorporated in the icy mantles of interstellar grains will clearly affect grain chemistry and physics.

Molecular hydrogen would fill the most energetic sites on the grain surface, leaving only weak sites for the physisorption of other molecules. If other heavier adsorbed chemical species cannot displace the bound H_2, such molecules will be bound less strongly to, and desorb more easily from, an H_2 rich ice (Allen and Robinson 1977), predicting less depletion of heavy species onto grains. Atomic and molecular mobility over the surface of amorphous ice mantles will be very different if the ice surface is saturated with H_2 (Smoluchowski 1983). One would intuitively expect that the surface mobility of other species would increase, as on average less energetic sites would be available. This could possibly enhance chemical reaction rates on grain surfaces, although surface abundances and the residence time scales for species heavier than H_2 would be lowered.

If the volume of icy grain mantles are also rich in H_2, this should provide a more reducing environment for energetic reactions in the mantle, such as those occurring in ice irradiation experimental simulations (see, for example, Greenberg *et al.* 1993; Pirronello 1993; and references therein). In addition, the overall increase in the ice mantle number density due to the bound H_2 may result in a higher heat capacity of the grain mantle than in previous estimates, thereby changing our understanding of mantle heating processes.

As comets are thought to be largely aggregates of interstellar icy grains, a truly primitive, unprocessed comet should reflect the composition of its interstellar origin. A primitive comet composed of ices that had never experienced temperatures above 20 K might then have a large amount of hydrogen incorporated in its bulk (see also Sandford *et al.* 1993). Comets composed of icy material that had experienced higher temperatures would show a diminished amount of hydrogen in accordance with the amounts

shown in Figure 1.5. The total amount of molecular hydrogen incorporated in a comet might then provide an indication of the degree of thermal processing that a comet, or the much smaller grains that accumulate to form comets, had experienced since the ice had originally condensed.

1.6. Conclusions

Our experimental results show that codeposition of H_2 with H_2O at 12 K can incorporate a large fraction of hydrogen in the water matrix, up to a mole H_2/H_2O ratio of 0.53. Nearly 80% of this population of H_2 sublimates at temperatures below 30 K, while the remainder appears stable well above 40 K. The more volatile component is consistent with an equilibrium distribution of surface binding site energies, described theoretically by Hixson *et al.* (1992). Such an explanation would predict a mole fraction of H_2 in interstellar grain mantles of nearly 0.3 due only to the accretion of gas phase molecular hydrogen. For the probable conditions of WL5 in the ρ Ophiuchi cloud, mole fractions for H_2 of between 0.05 and 0.3 are calculated from the equilibrium model, in possible agreement with the observed abundance (Sandford *et al.* 1993).

To adequately test if this process can explain the recent detection of frozen H_2 in interstellar ices, more work is needed on laboratory, theoretical, and observational fronts. Laboratory work is required to definitively establish whether our results are either due to an equilibrium bound population of H_2, or mechanical matrix trapping of H_2 by the water deposition. Such work needs to be understood in detail if the results are to be extrapolated to interstellar conditions. Experimental work is also needed to determine if

other common interstellar ices, such as CO or CH_3OH, have the same ability to adsorb a large fraction of H_2 as water ice. The modeling must also substantially improve, to determine how the potential energy surface of a simulated amorphous water cluster changes as more molecular hydrogen is added. Additional work also is needed to predict the likelihood and relative energies of sites deep within an ice volume. Finally, the observational detection of solid phase H_2 in interstellar space demands more such work along many different lines of sight. The generality of this feature is key to our understanding of the processes which may yield H_2 in interstellar grain mantles.

Since the submission of this paper, we have become aware of the work of Buch and Devlin (1994), who report results of both computational and spectroscopic studies of H_2 adsorption on icy grain mantles. They also conclude that gas-phase adsorption can generate H_2 abundances of several percent in interstellar grain mantles.

Acknowledgments

This work represents research carried out at the Jet Propulsion Laboratory, California Institute of Technology, under contract to the National Aeronautics and Space Administration. One of us (RWD) would like to thank the NASA Graduate Student Researchers Program for their support. The comments of G. Blake, W. Langer, and M. Werner are appreciated.

References

Allamandola, L. J., S. A. Sandford, and A. G. G. M. Tielens 1992. Infrared spectroscopy of dense clouds in the C-H stretch region: Methanol and diamonds. *Astrophys. J.* **399**, 134.

Allamandola, L. J., S. A. Sandford, and G. J. Valero 1988. Photochemical and thermal evolution of interstellar/precometary ice analogs. *Icarus* **76**, 225.

Allen, M., and G. W. Robinson 1976. Molecular hydrogen in interstellar dark clouds. *Astrophys. J.* **207**, 745.

Allen, M., and G. W. Robinson 1977. The molecular composition of dark interstellar clouds. *Astrophys. J.* **212**, 396.

Buch, V., and J. P. Devlin 1994. Interpretation of the 4141 cm^{-1} (2.415 μm) interstellar infrared absorption feature. *Astrophys. J.* **431**, L135.

Dissly, R. W., M. Allen, and V. G. Anicich 1992. H_2-rich grain mantles. *Bull. Amer. Astr. Soc.* **24**, 1120.

Govers, T. R., L. Mattera, and G. Scoles 1980. Molecular beam experiments on the sticking and accommodation of molecular hydrogen on a low-temperature substrate. *J. Chem. Phys.* **72**, 5446.

Greenberg, J. M., C. X. Mendoza-Gomez, M. S. de Groot, and R. Breukers 1993. Laboratory dust studies and gas-grain chemistry. In *Dust and Chemistry in Astronomy* (T. J. Millar and D. A. Williams, Eds.), pp. 271-295. Bristol, Philadelphia.

Hixson, H. G., M. J. Wojcik, M. S. Devlin, J. P. Devlin, and V. Buch 1992. Experimental and simulated vibrational spectra of H_2 adsorbed in amorphous ice: Surface structures, energetics, and relaxations. *J. Chem. Phys.* **97**, 753.

Hollenbach, D., and E. E. Salpeter 1970. Surface adsorption of light gas atoms. *J. Chem. Phys.* **53**, 79.

Kerr, T. H., A. J. Adamson, and D. C. B. Whittet 1991. Sharp infrared CO features in the ρ Ophiuchi molecular cloud. *Mon. Not. R. Astr. Soc.* **251**, 60P.

Laufer, D., E. Kochavi, and A. Bar-Nun 1987. Structure and dynamics of amorphous water ice. *Phys. Rev. B* **36**, 9219.

Lee, T. J. 1972. Formation of interstellar molecular hydrogen. *Nature* **237**, 99.

Lee, T. J., L. Gowland, and V. C. Reddish 1971. Condensation of hydrogen on interstellar grains. *Nature* **231**, 193.

Mayer, E., and R. Pletzer 1986. Astrophysical implications of amorphous ice - a microporous solid. *Nature* **319**, 298.

Moore, M. H., and R. L. Hudson 1992. Far-infrared spectral studies of phase changes in water ice induced by proton irradiation. *Astrophys. J.* **401**, 353.

Pirronello, V. 1993. Irradiation of molecular ices. In *Dust and Chemistry in Astronomy* (T. J. Millar and D. A. Williams, Eds.), pp. 297-329. Bristol, Philadelphia.

Sandford, S. A., and L. J. Allamandola 1993. H_2 in interstellar and galactic ices: Infrared characteristics, UV production, and implications. *Astrophys. J.* **409**, L65.

Sandford, S. A., L. J. Allamandola, and T. R. Geballe 1993. Spectroscopic detection of molecular hydrogen frozen in interstellar ices. *Science* **262**, 400.

Smoluchowski, R. J. 1983. Adsorption and mobility on amorphous surfaces: Application to astrophysical problems. *J. Phys. Chem.* **87**, 4229.

Solomon, P. M., and N. C. Wickramasinghe 1969. Molecular and solid hydrogen in dense interstellar clouds. *Astrophys. J.* **158**, 449.

Tanaka, M., S. Sata, T. Nagata, and T. Yamamoto 1990. Three micron ice-band features in the ρ Ophiuchi sources. *Astrophys. J.* **352**, 724.

Tielens, A. G. G. M., and L. J. Allamandola 1987. Composition, structure, and chemistry of interstellar dust. In *Interstellar Processes* (D. J. Hollenbach and H. A. Thronson, Jr., Eds.) p. 397. Reidel, Dordrecht.

Tielens, A. G. G. M., and W. Hagen 1982. Model calculations of the molecular composition of interstellar grain mantles. *Astron. Astrophys.* **114**, 245.

Wickramasinghe, N. C., and V. C. Reddish 1968. Accretion of solid hydrogen mantles by grains in OB associations. *Nature* **218**, 661.

Wilking, B. A., and J. L. Lada 1983. The discovery of new embedded sources in the centrally condensed core of the ρ Ophiuchi dark cloud: The formation of a bound cluster? *Astrophys. J.* **274**, 698.

Chapter 2. The Photochemical Fate of Ethylene on Triton's Surface

Abstract

We present the results of UV photolysis experiments on C_2H_4 ice to simulate the irradiation of this species on the surface of Triton. Photochemical models of Triton's atmosphere predict C_2H_4 as a primary product of methane dissociation, formed at a high enough level that it should be readily observable as a surface condensate in $\leq 10^6$ years, yet it has not been observed. Our results show that C_2H_4 ice is readily dissociated by radiation of wavelengths $\leq$ 1849Å, with C_2H_2 ice as a primary product. Dilution in an inert N_2 matrix does not affect the photochemical yield of C_2H_2, suggesting that the reaction $C_2H_4 \rightarrow C_2H_2$ is unimolecular. Quantum yields for both the destruction of C_2H_4 and the formation of C_2H_2 are discussed, as functions of both irradiation wavelength and dilution in N_2 ice. Applying these results to Triton, we find that the ambient UV flux reaching Triton's surface is more than adequate to explain the non-detection of ethylene ice.

2.1. Introduction

Our present understanding of the chemistry of icy surfaces in the outer solar system is still poorly developed. Gross differences still remain, for example, between predicted cosmochemical compositions and the observed speciation of surface ices. Water is expected to be the primary icy component for all bodies, but has yet to be detected on either Triton or Pluto. The nitrogen budget is overwhelmingly dominated by N_2, as seen on Titan, Triton, and Pluto, while a highly reducing solar nebula would reasonably predict ammonia as the most prevalent nitrogen species. Carbon, on the other hand, is primarily observed in the reduced form of methane, while the oxidized species such as CO and CO_2 that should accompany the observed N_2 in the solar nebula (Prinn and Fegley 1989) are only observed as trace components at best (Cruikshank *et al.* 1993; Owen *et al.* 1993). It is thus evident that a great deal of subsequent processing of outer solar system ices must occur to satisfy the present day observations.

Discrepancies also exist on a more local level between predicted and observed speciation in specific planetary atmospheres and surfaces. An incomplete understanding of chemical processing is likely the reason for these differences as well. This paper addresses such a specific discrepancy: the non-detection of ethylene ice (C_2H_4) on the surface of Triton. In an atmosphere such as Triton's with a substantial amount of methane, the photochemical dissociation of CH_4 leads to the formation of radicals that recombine to form a range of C_2 hydrocarbons. Previous researchers have modeled the methane photochemistry of Triton's atmosphere (Strobel *et al.* 1990; Lyons *et al.* 1994) and predict ethylene as the primary photochemical end-product, with over an order of magnitude greater production rate than

any other species. The specific methane photodissociation pathways used in these models are outlined below:

$$CH_4 + h\nu \rightarrow {}^1CH_2 + H_2 \quad (1)$$

$$\rightarrow {}^3CH_2 + H_2 \quad (2)$$

$$\rightarrow CH + H_2 + H\,. \quad (3)$$

These product radicals then recombine to form C_2H_4 via the following reactions:

$$CH + CH_4 \rightarrow C_2H_4 + H \quad (4)$$

$$CH_3 + {}^3CH_2 \rightarrow C_2H_4 + H\ . \quad (5)$$

For the ambient low temperature of ~38 K on Triton's surface (Tryka *et al.* 1993), hydrocarbon products such as ethylene are highly supersaturated and should rapidly condense out of the atmosphere onto the surface. A haze layer is in fact seen in Triton's atmosphere (c.f., Herbert and Sandel 1991), which is most likely the result of the nucleation of such photochemical products. Lyons *et al.* (1994) predict a column condensation rate of 1.7×10^8 molecules cm^{-2} sec^{-1} for ethylene, which should produce an easily detectable surface layer of C_2H_4 ice in about 10^6 years. However, C_2H_4 has yet to be detected either as a surface or atmospheric constituent on Triton. Nor has it been seen on Pluto, which has a similar atmospheric composition and thus a similar expected photochemistry.

There are several possible explanations for the non-detection of ethylene. First, the photochemical models may not adequately describe the atmospheric chemistry of Triton. For example, recent experimental work

(Mordaunt *et al.* 1993) has shown that the methyl radical is the dominant primary photodissociation product at 1216 Å:

$$CH_4 + h\nu \rightarrow CH_3 + H \ . \qquad (6)$$

The three-body recombination of methyl radicals produces C_2H_6, so these authors have suggested this as the primary formation pathway for ethane in Titan's atmosphere, for example. Like ethylene, C_2H_6 has not been detected on Triton, but including this photodissociation channel in Triton photochemical models will probably affect the relative hydrocarbon production rates. However, until such model runs are made, we will assume that C_2H_4 is an important chemical product.

A second explanation for the non-detection is burial of C_2H_4 ice by global-scale volatile transport on seasonal time scales of ~1000 years (see, e.g., Trafton 1984). As C_2H_4 is non-volatile at Triton temperatures, abundant mobile species such as N_2 may rapidly cover hydrocarbon deposits, hiding them from direct observation.

As a third possibility, previous authors (Cruikshank *et al.* 1984; Thompson and Sagan 1990) have suggested that surface hydrocarbon ices on Triton such as C_2H_4 could be chemically modified by energetic radiation, forming products that are perhaps not easily detected within the limits of current infrared spectroscopic techniques. On Triton's surface, the ambient solar UV flux has been estimated to cause observable photochemical changes much faster than the flux of energetic particles from cosmic rays, the solar wind, or Neptune's magnetosphere (Thompson and Sagan 1990).

This work represents a quantitative study of the UV photolysis of solid state ethylene. The results quantitatively establish the dissociation rates, UV

cross sections, and absolute product yields of solid state C_2H_4 photolysis, which are then applied to Triton conditions to interpret the photochemical kinetics of possible surface ethylene ice. We find that the ambient UV flux reaching Triton's surface leads to photodissociation that is more than adequate to explain the non-detection of ethylene ice.

The photochemical alteration of astrophysical ices in general has been a subject of much recent research. Both ion irradiation and ultraviolet photolysis have been simulated in the laboratory for a wide range of ices abundant in both the outer solar system and interstellar medium (see, e.g., Moore *et al.* 1983; Allamandola *et al.* 1988; Greenberg *et al.* 1993; Pirronello 1993). To date, the bulk of the UV photolysis studies have been largely qualitative in nature, focusing primarily on product identifications and relative yields. Such cataloging work has been quite successful in offering formation mechanisms for detections of otherwise anomalous chemical species. However, very little *quantitative* research has been done on the UV photolysis of ices with application to astrophysical environments, such as the determination of specific product quantum yields under a well characterized radiation field, or an understanding of the full network of both primary and secondary reactions that lead to a final observed product distribution. As such, an understanding of the kinetics for the chemistry of ices in the outer solar system is almost wholly lacking. The field of solid state kinetics is in general very immature compared to its gas phase counterpart, especially with respect to astrophysical applications. It would be interesting to compare the kinetics in ices to the equivalent known gas phase reactions to determine if there are fundamental differences between them.

2.2. Background

Extensive quantitative research has been reported on the vacuum ultraviolet photolysis of gas phase ethylene (e.g., Sauer and Dorfman 1961; Okabe and McNesby 1962; Back and Griffiths 1967; Hara and Tanaka 1973), while corresponding work with the liquid and solid states has received less attention (Tschuikow-Roux *et al.* 1967; Gorden and Ausloos 1971; Hirokami and Cvetanovic 1974). In the gas phase, the primary dissociation pathways are listed below:

$$C_2H_4 + h\nu \rightarrow [C_2H_4^*] \rightarrow C_2H_2 + H_2 \quad (7)$$

$$\rightarrow C_2H_2 + 2H \quad (8)$$

$$\rightarrow C_2H_3 + H \quad (9)$$

The quantum yields (ϕ) for these respective reactions depend on the incident wavelength, and are summarized below in Table 2.1. While molecular hydrogen and acetylene (C_2H_2) dominate the product yield in all experiments,

Table 2.1. Quantum Yields for Gas Phase Ethylene Photodissociation Channels

	ϕ_6	ϕ_7	ϕ_8	References
1236 Å	0.28	0.72	0	1
1470 Å	0.36	0.62	0.01	2
1634 Å	0.47	0.48	0.05	3
1849 Å	0.53	0.33	0.14	3
1930 Å	0.53	0.33	0.14	4

References: (1) Okabe and McNesby 1962; (2) Sauer and Dorfman 1961; (3) Hara and Tanaka 1973; (4) Balko *et al.* 1992.

n-butane (C_4H_{10}) and ethane (C_2H_6) are also produced above the 10% level. The proposed reactions to form these products (Sauer and Dorfman 1961) involve the formation of the ethyl radical (C_2H_5), as outlined below:

$$H + C_2H_4 \rightarrow C_2H_5 \quad (10)$$

$$C_2H_5 + C_2H_5 \rightarrow C_4H_{10} \quad (11)$$

$$\rightarrow C_2H_4 + C_2H_6 \quad (12)$$

On a per molecule basis, these authors show that the sum of the yields of C_2H_2, C_2H_6, and C_4H_{10} is the same as the loss of C_2H_4, so the above reactions provide a complete description of the primary processing, with the exception of the vinyl radical (C_2H_3) formed at the longer wavelengths.

Wavelength dependent UV absorption cross-sections have also been established for ethylene in the gas phase (Zelikoff and Watanabe 1953). The strongest absorption occurs near 1700 Å, with $\sigma \sim 3 \times 10^{-17}$ cm^2. The cross section remains close to this value at shorter wavelengths: at Lyman α (1216 Å) $\sigma \sim 2.3 \times 10^{-17}$ cm^2. The cross section falls off rapidly for $\lambda > 1900$ Å.

For solid state photolysis, only relative product yields have been reported. C_2H_2 and H_2 again are the dominant products, formed with nearly equivalent yields. Additional products are only seen at the few percent level at best, such as 1-butene (C_4H_8) and n-butane (C_4H_{10}). The fate of the vinyl radical is still largely uncertain, in both the solid state and gas phase experiments. It has been suggested (Hirokami and Cvetanovic 1974) that C_2H_3 can associate with C_2H_4 in the solid state. These authors also suggest that photoexcited C_2H_4 can associate with C_2H_4 in the ground state. Such association reactions are a common mechanism invoked for polymer

formation. This will be discussed later in the paper in the context of the current experiments.

While the relative yields of the observed products in solid-state photolysis have been reported, the quantum yields have not. In addition, the degree of consumption of the original C_2H_4 ice has not been monitored, as it has in the gas phase. As such, there may be additional products that have not been accounted for. It is possible that the close proximity of excited and radical products in solid state photolysis could lead to association reactions not observed in the gas phase, as the surrounding matrix will act as a third body to satisfy the energy and momentum constraints that prohibit association in the gas phase. On the other hand, excited states may be rapidly quenched by the matrix, prohibiting certain decay mechanisms. The possibility of fundamental differences between gas phase and solid state processes warrants further study.

Previous C_2H_4 photolysis experiments in the solid state have used chromatographic and mass spectrometric techniques to identify and quantify products. The products were thus not measured *in situ* in the ice, but rather in the gas phase subsequent to photolysis by heating the sample. Such a technique introduces some ambiguity in the identification of products due only to photolysis, as the heating of the ice may release trapped radicals that react when they otherwise would not in the frozen sample. Such radical storage and release is believed to be common in ice photolysis experiments, and can release enough energy to cause the sample to literally explode upon heating (d'Hendecourt *et al.* 1982). Such a process has been proposed as a viable desorption mechanism for interstellar ices (c.f., Leger *et al.* 1985).

This paper presents quantitative results of the ultraviolet photolysis of ethylene ice, monitored spectroscopically in the solid state to avoid the

ambiguities that may be caused by sample heating. Mass spectroscopic scans are also used for the qualitative identification of photolysis products, especially those not identifiable spectroscopically, such as H_2. The effects of radiation wavelength, fluence (time integrated flux), and dilution in an N_2 matrix are investigated to test the range of possible conditions that may exist on Triton's surface. The goal of this paper is to provide a mechanistic description of the chemical processing caused by photolysis, rather than just to compile empirical results that satisfy the current observations. Such an understanding gives predictive power for the range of environmental conditions that Triton, and other icy bodies, may experience at different points in their histories.

2.3. Experimental

2.3.1. Apparatus Description

The spectroscopic setup utilized in these experiments is the Extraterrestrial Ice Simulator (EIS) at JPL. The design is similar to other facilities that study the infrared spectra of astrophysical ices (e.g., Allamandola *et al.* 1988). Figure 2.1 is a schematic of the apparatus. The EIS consists of two differentially pumped chambers, which are each evacuated by a turbomolecular pump (Balzers TPU 170) to a background pressure of ~3 x 10^{-8} torr. Extending into the first chamber is a closed cycle helium refrigerator (Air Products Displex DE-202), which can be cooled down to 12 K. Attached to the end of the refrigerator is a sapphire window, the optical substrate upon which the ice samples are deposited. The temperature of the window can be varied from 12 K to room temperature, with an accuracy of better than 0.1 K,

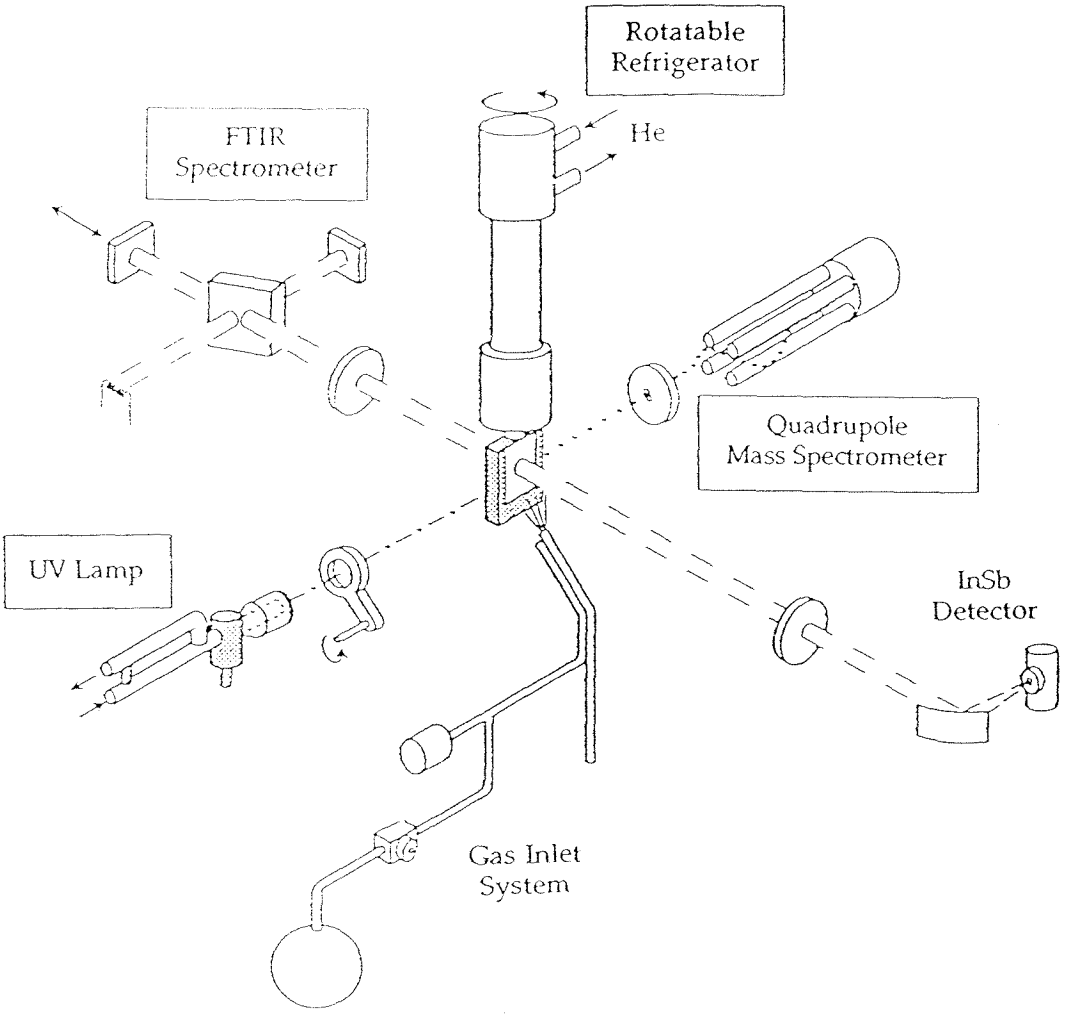

Figure 2.1. Schematic of the Extraterrestrial Ice Simulator (EIS) at JPL.

by a resistive heater at the base of the window, monitored by a silicon diode epoxied to the window and maintained by a temperature control system (Lakeshore DRC-93CA). The silicon diode was calibrated at both liquid N_2 and liquid He temperatures. Ice samples are prepared by spraying from a pinhole nozzle, 0.06 mm in diameter, set 4.0 cm away from the window. The deposition rate and sample thickness are measured by monitoring the interference fringes from a HeNe laser reflected off the surface of the growing film, described in detail in Appendix A. Typical deposition rates were ~ 1 μm/hr. The bulk of the photolysis experiments were done at 38 K to simulate current Triton surface conditions.

The spectrometer in the EIS facility is a Mattson Fourier Transform Infrared Spectrometer (Cygnus 25, Galaxy upgrade), capable of 0.25 cm^{-1} spectral resolution, although all data were taken in the current work at a resolution of 1 cm^{-1}, as higher resolutions gave no additional detail in the ice spectra. Spectra were taken in the region from 2000 - 5000 cm^{-1}, as sapphire is opaque below 2000 cm^{-1}. A tungsten halogen source and InSb detector were used for all spectra, to maximize the signal in the C-H stretching features near 3000 cm^{-1} that were used to monitor the abundances of ethylene and resultant photolysis products. Transmission spectra of the ice samples were determined by taking the ratio of the lamp intensities with and without an intervening ice sample. All interferograms were apodized using the Beer-Norton weak function (see, e.g., Griffiths and deHaseth 1986), provided by Mattson. Optical fringing in the frequency spectra was a problem, caused by plane-parallel resonances in the optical path. This fringing appeared as spikes in the original interferogram. Removal of these resonance spikes helped reduce the fringing considerably, without affecting the bandshapes that were

being measured. Additional spectral analysis, such as baseline corrections and band absorbance integrations, were made using Mattson FIRST™ software.

Once a sample had been deposited, the entire refrigerator (and attached sample) could be rotated by 90° without breaking vacuum to face the ultraviolet source. Two different sources were used, both powered by a microwave discharge cavity: a continuous-flow hydrogen lamp and a sealed mercury lamp. The hydrogen lamp used a mixture of 90% He and 10% H_2 at a constant pressure of ~ 1 torr, and provided radiation from Lyman α (1216 Å) out through the H_2 molecular emission bands (1400 - 1650 Å), while the Hg lamp was used as a line source at 1849 Å. The total flux on the sample was continuously monitored by a silicon photodiode (International Radiation Detectors, Inc., model XUV-100). The procedure used to quantify the UV flux is detailed in Appendix B. After the sample had been irradiated, the refrigerator column was rotated back so that the sample was perpendicular to the spectrometer beam, and a spectrum taken again. This procedure was repeated several times for each sample, to monitor the progress of the photolysis. All ice samples appeared visibly clear, with no discernible coloration even after several hours of photolysis. Sample thicknesses varied from ~ 0.5 to 5 μm.

The composition of some irradiated ice samples was also characterized by heating the sample, and monitoring the evolved gas phase species with a quadrupole mass spectrometer (Extrel), housed in the second, adjacent vacuum chamber. The mass spectrometer was used only for product identification, not for quantitative analysis. In addition, all experimental data acquisition (sample temperature, chamber pressure, UV flux, HeNe laser reflectance, and mass spectrometer scans) was automated using LabVIEW routines controlled and digitally recorded on a computer.

The gases used in these experiments were nitrogen (Matheson Research Grade, 99.9995% pure), ethylene (Matheson, 99.5%), and acetylene (Matheson, 99.6%). The nitrogen was used without additional purification, while both the C_2H_4 and C_2H_2 were further purified by repeated vacuum distillation at liquid nitrogen temperatures.

2.3.2. Calibration of Column Abundances

As described in Appendix A, the thicknesses of the ice samples were determined by monitoring interference fringes in the reflected intensity of a HeNe laser from the surface of the ice as it was being deposited. Deposition rates for each species were found for fixed nozzle backing pressures over a range of substrate temperatures by depositing an ice sample thick enough to generate several fringes. Subsequent depositions under the same conditions occur at the same rate, so that the thickness of even very thin films that generate less than one reflected fringe could be found by simply monitoring the deposition time and extrapolating from the known rate. The deposition rate for a given species and substrate temperature was not a simple linear function of nozzle backing pressure, so the backing pressure was kept constant over all experimental runs (at 0.2 torr). This control keeps the relative exposure of the sapphire substrate to the incoming gas uniform between different experiments.

When mixtures of gases were deposited (e.g., N_2 and C_2H_4), the total backing pressure was again kept at 0.2 torr. The deposition rate of each species was taken to be just that of the pure gas weighted by its partial pressure in the reservoir gas. This assumes that it is the *total* backing pressure that determines the substrate exposure, and that the simultaneous deposition of the two species do not affect each other's rates. This is admittedly an

oversimplification, as sticking coefficients and binding energies for deposited gases can depend strongly on the nature of the substrate, as seen from the results in the hydrogen-water ice experiments of Chapter 1.

2.4. Results of Photolysis

2.4.1. Product Identification

In the spectral range of 2000 - 5000 cm^{-1} used for these experiments, the *only* spectroscopic changes seen in the photolysis of ethylene for both UV sources was the production of C_2H_2 at the expense of C_2H_4, as shown in Figure 2.2. No other products were identifiable spectroscopically. Defining upper limits of the possible products outlined in Section 2.2 is difficult, as the band strengths for C_2H_6, C_4H_8, and C_4H_{10} have not been previously determined. In addition, no C-H stretching features have been assigned unambiguously to the vinyl radical, C_2H_3, although dipole moment derivatives have been calculated. This will be discussed later in the paper.

As an independent check on identifying possible photolysis products, mass spectroscopic scans were made during the heating of some irradiated samples, as done by previous authors (see Section 2.2). The first scans were made over the range of 0 - 70 amu, shown in Figure 2.3, for several different sample temperatures during heating at a constant rate. Although features can be seen for H_2O, C_3, and C_4 hydrocarbons, in addition to H_2 and the C_2 hydrocarbons, the former species are common to all temperatures, including the background, so that they do not originate from the ice sample. The only species due to the heating of the ice are at masses 2, 26, 27, and 28 amu. No positive identification can be made for either C_2H_6 (mass 30) or n-butane

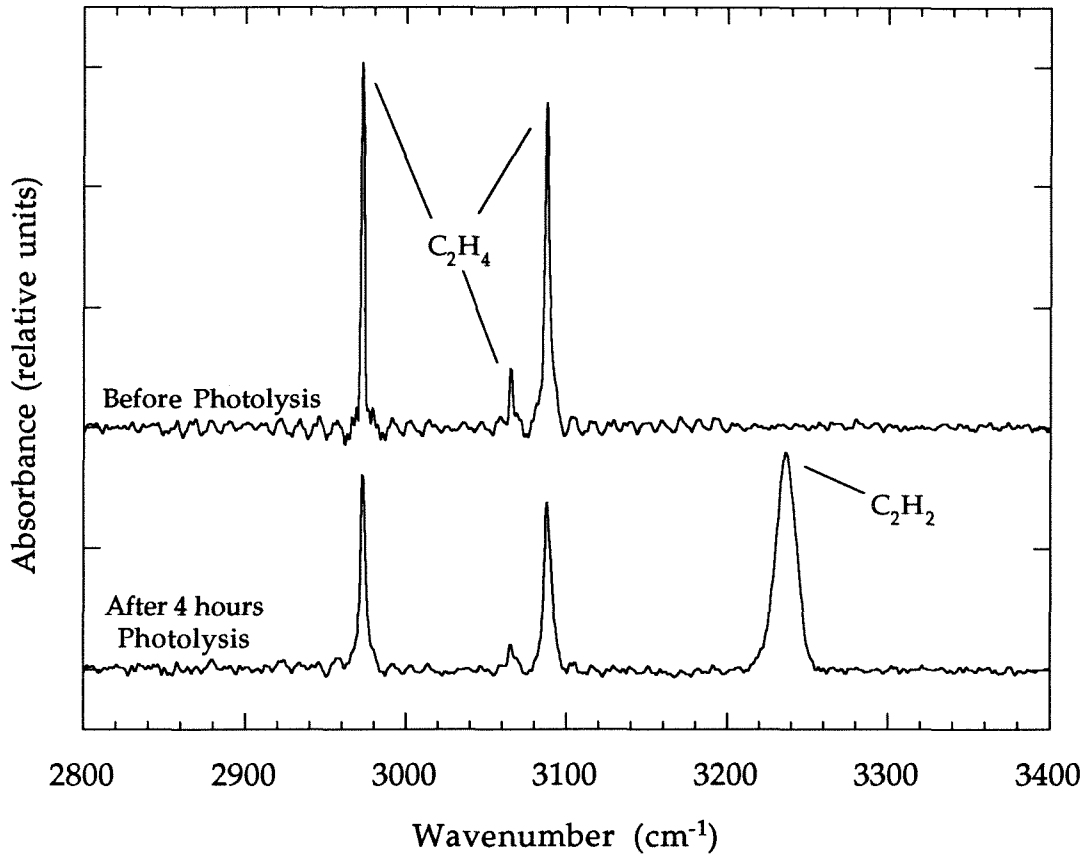

Figure 2.2. Qualitative spectroscopic evidence of the effect of hydrogen lamp irradiation on a sample of C_2H_4 ice: C_2H_2 is clearly produced at the expense of C_2H_4. The Hg lamp also induces this chemical change. The absorbance scale is the same for both spectra.

(mass 58), photolysis products reported by other researchers, on the basis of these results.

Once it was determined which masses were liberated by the heating of the ice sample, a series of mass spectroscopic experiments was done to study these in more detail. Four different ice samples were deposited: C_2H_4 with no photolysis, C_2H_2 with no photolysis, and C_2H_4 irradiated for both 40 minutes and 5 hours under the Hg lamp. The deposition of all four samples

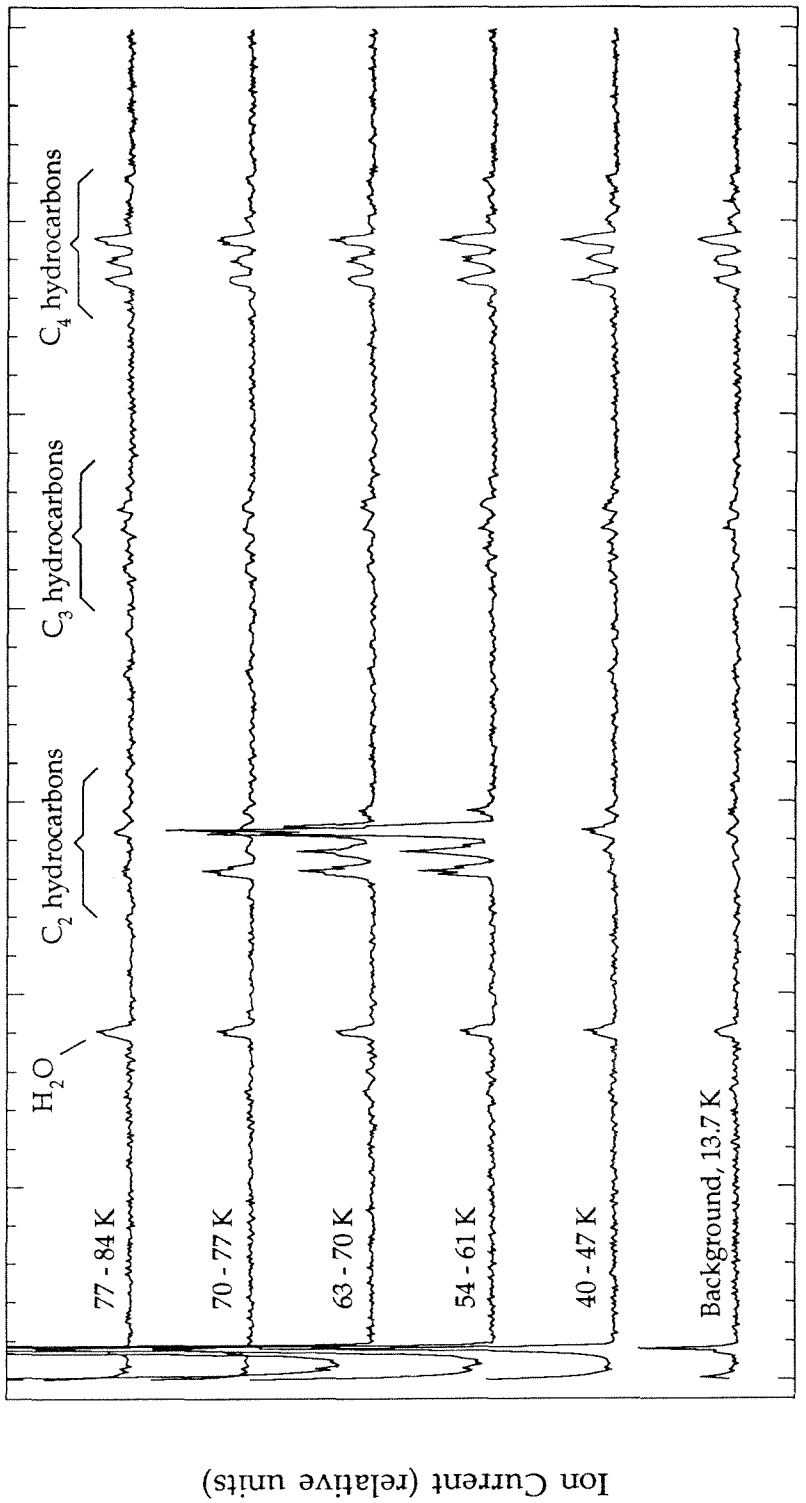

Figure 2.3. Mass spectrometer sweeps during the heating of a C_2H_4 ice sample that had been subjected to 100 minutes of irradiation under the Hg lamp. Note that the only qualitative differences in the sweeps occur at masses 2, 26, 27, and 28; these are the only masses affected by the photolysis.

was monitored to give the same initial abundance of material, as determined spectroscopically from the initial column density. The samples were then heated at 4 K/minute and the liberated gas phase species monitored at 2, 26, 27, and 28 amu, as these were the only masses affected by photolysis. The unirradiated samples of C_2H_4 and C_2H_2 were used as controls to determine if a substantial fraction of the product yield at a particular mass was due to electron impact dissociation in the ionizing region of the mass spectrometer rather than as a result of photolysis.

The results of these temperature programmed desorption experiments are shown in Figures 2.4 (a-d). As seen in Fig. 2.4 (a), H_2 is a definite product of photolysis, with the yield increasing as a function of irradiation dosage. Note that the majority of the H_2 is liberated only when the C_2H_4 sample sublimates at temperatures above 60 K, suggesting that the hydrogen is trapped in the matrix where it is produced. This is interesting in the context of the experimental results from Chapter 1 on H_2/H_2O mixtures, which were consistent with a population of adsorbed H_2 in equilibrium with the gas phase, controlled only by a range of binding energies in the water ice rather than being physically trapped. It would be interesting to try the stepwise heating experiments used in Chapter 1 to investigate in greater detail the thermal stability of H_2 in photolyzed C_2H_4 ices.

The scans in Figure 2.4 (b) for C_2H_2 (mass 26) clearly show acetylene as an irradiation product. The scan for the 5 hour photolysis experiment shows two peaks: the first is due to the electron impact dissociation of the unprocessed C_2H_4, and the second is due to C_2H_2 produced in the ice by photolysis. It is also clear that increasing the radiation dosage increases the yield of acetylene at the expense of the original C_2H_4, comparing the 40 minute and 5 hour experiments.

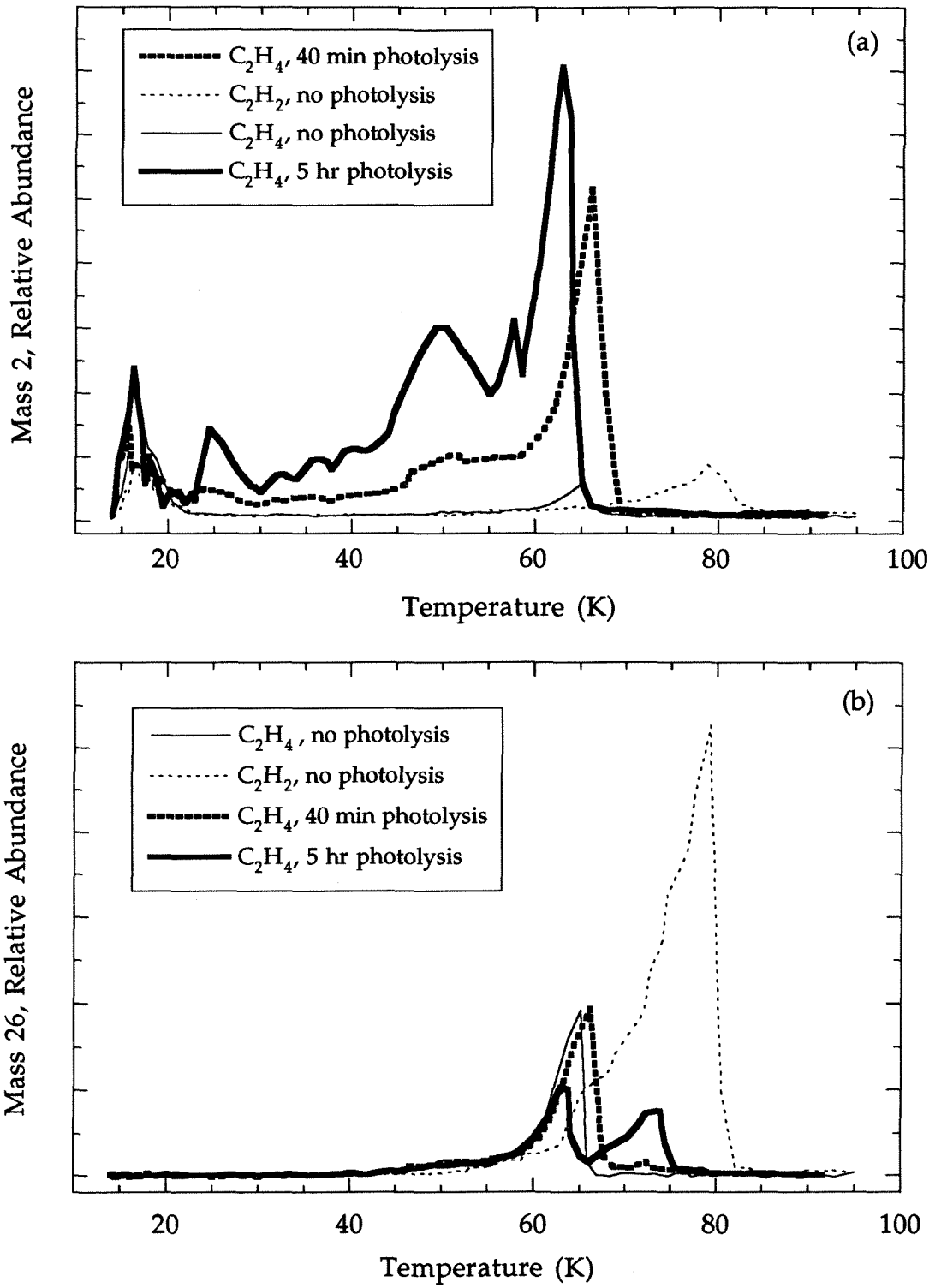

Figure 2.4. Ion current profiles for H_2 (a) and C_2H_2 (b) during steady heating of four different samples. The initial column densities were identical.

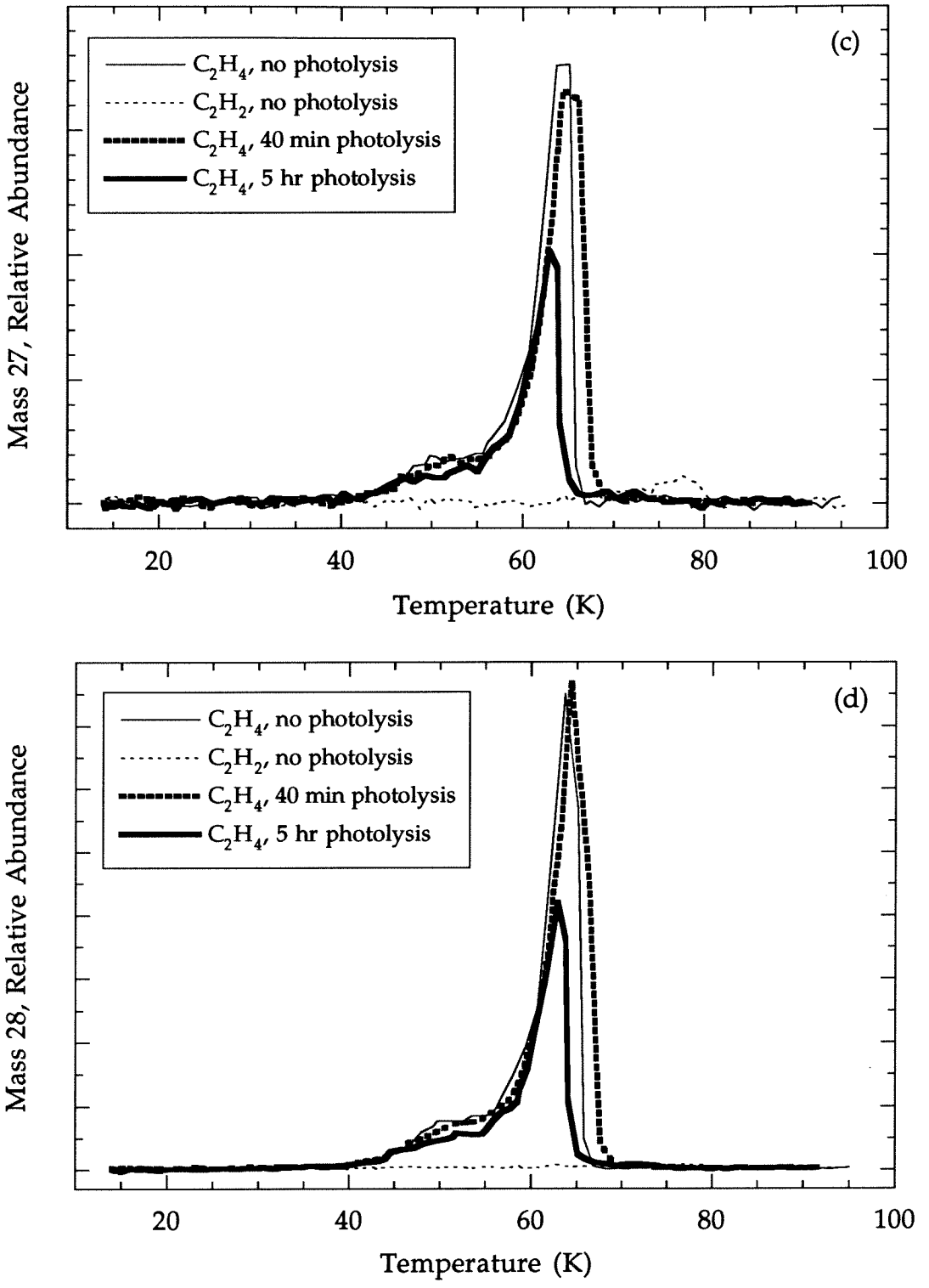

Figure 2.4 (cont'd). Ion current profiles for C_2H_3 (c) and C_2H_4 (d) from the same four samples.

Comparing the scans for C_2H_3 (mass 27) and C_2H_4 (mass 28) in figures 2.4 (c) and (d), it is apparent that the amount of C_2H_3 correlates to the amount of C_2H_4, independent of radiation dosage. This shows that the detected C_2H_3 is due only to the electron impact dissociation of C_2H_4. This result would suggest that the formation and trapping of vinyl radicals in the photolyzed C_2H_4 is not an important process, unless large amounts of trapped C_2H_3 react during the sample heating, as discussed earlier in section 2.2.

2.4.2. Quantitative Infrared Spectral Analysis

The technique outlined in section 2.3.2 is appropriate for measuring the initial column abundance of a deposited species, but does not help determine the amount of change in species abundance as the result of ultraviolet photolysis, the primary subject of this chapter. To quantitatively measure the change in column abundance of both C_2H_4 and C_2H_2, the primary species of interest here, near-IR spectra were taken several times during photolysis. As discussed in the experimental section, the ice sample could be rotated from the irradiation position into the spectrometer beam, a spectrum taken, then rotated back for additional photolysis. The UV irradiation source was turned off while a spectrum was being taken.

To calculate a column density from the size of a particular IR feature, the integrated absorbance of the band must be known. The integrated band absorbance, or band intensity, has been labeled A by previous authors (see, e.g., Zhao, Ospina, and Khanna 1988; Hudgins *et al.* 1993). For an optically thin sample, as used in these experiments, this is defined as

$$A = \frac{\int \tau \, d\nu}{N} \tag{13}$$

where N is the column density of the species of interest and $\int \tau d\nu$ is the absorbance integrated over the full frequency range of the band. The absorbance is simply the optical depth in the sample at each frequency,

$$\tau(\nu) = -\ln\left[\frac{I(\nu)}{I_o(\nu)}\right] \tag{14}$$

with $I(\nu)$ as the flux through the ice sample at frequency ν, and $I_o(\nu)$ the background flux (no sample), as described in the experimental section.

In the range of 2000 - 5000 cm^{-1} used in these experiments, solid-state acetylene has one prominent feature at 3223 cm^{-1}, the ν_3 asymmetric C-H stretch. Solid ethylene has several features in this region, the two largest being the ν_9 band at 3088 cm^{-1} and the ν_{11} band at 2973 cm^{-1}. These features can be seen in Fig. 2.2. These three strongest bands are monitored in the experiments to determine the changing abundances of C_2H_2 and C_2H_4. The A value for the ν_3 C_2H_2 band is reported to be 3.6 x 10^{-17} cm/molecule (Khanna *et al.* 1988), while the A values for the C_2H_4 ν_9 and ν_{11} bands are given as 1.3 x 10^{-18} cm/molecule and 7.4 x 10^{-19} cm/molecule, respectively (Zhao *et al.* 1988). As described by these authors, the anomalous dispersion (rapid change in the complex index of refraction) near a strong feature results in a perturbation of the measured line strength, due to reflective losses from the film-vacuum and film-substrate interfaces. These reported A values take such losses into account, so that they represent the "pure" integrated band absorbances, describing only the bulk ice. As the integrated band absorbances in the present experiments were to be used only as calibrations for determining column abundances for the particular setup of these experiments, it was easier to simply remeasure the integrated absorbances

with the reflective losses folded in, rather than trying to calculate the amount of reflected loss using the previously reported "pure" values. Even though the current values are somewhat offset from the "pure" ones, this difference is the same for both the calibrations and experiments. In addition, the *A* values are somewhat temperature dependent, so the previously reported values would not have been as accurate for the current experimental temperatures. The proper "pure" integrated band absorbances can be determined from the present reported measurements, but such modeling is beyond the scope of this work.

To determine the integrated band absorbances for the strong IR features of C_2H_2 and C_2H_4, ice samples of known thickness were deposited for both species, using the laser monitoring technique described in Appendix A. Several thicknesses were deposited, all optically thin for the band of interest, so that a line could be fit through a Beer's Law plot of column density versus band absorbance to determine the *A* value. As the transition point for an absorbance feature to deviate from the optically thin regime is at a peak absorbance of ~ 0.7 (Griffiths and deHaseth 1986), all bands were kept well below this value. The data and least-squares fits are shown for C_2H_4 in Fig. 2.5 (a) and (b), and for C_2H_2 in Fig. 2.6 (a) and (b), for ices at both 38 K and 17 K. The error bars are primarily due to uncertainty in the baseline of the absorbance features. The measured integrated band absorbances are summarized in Table 2.2.

These measured *A* values represent the integrated band absorbances for pure C_2H_2 and C_2H_4 ices. However, as the band strength and position for a particular species are dependent on the nature of the surrounding matrix, it is necessary to determine *A* values for the appropriate experimental conditions. As shown previously, C_2H_2 is a photochemical product of irradiated C_2H_4 ice.

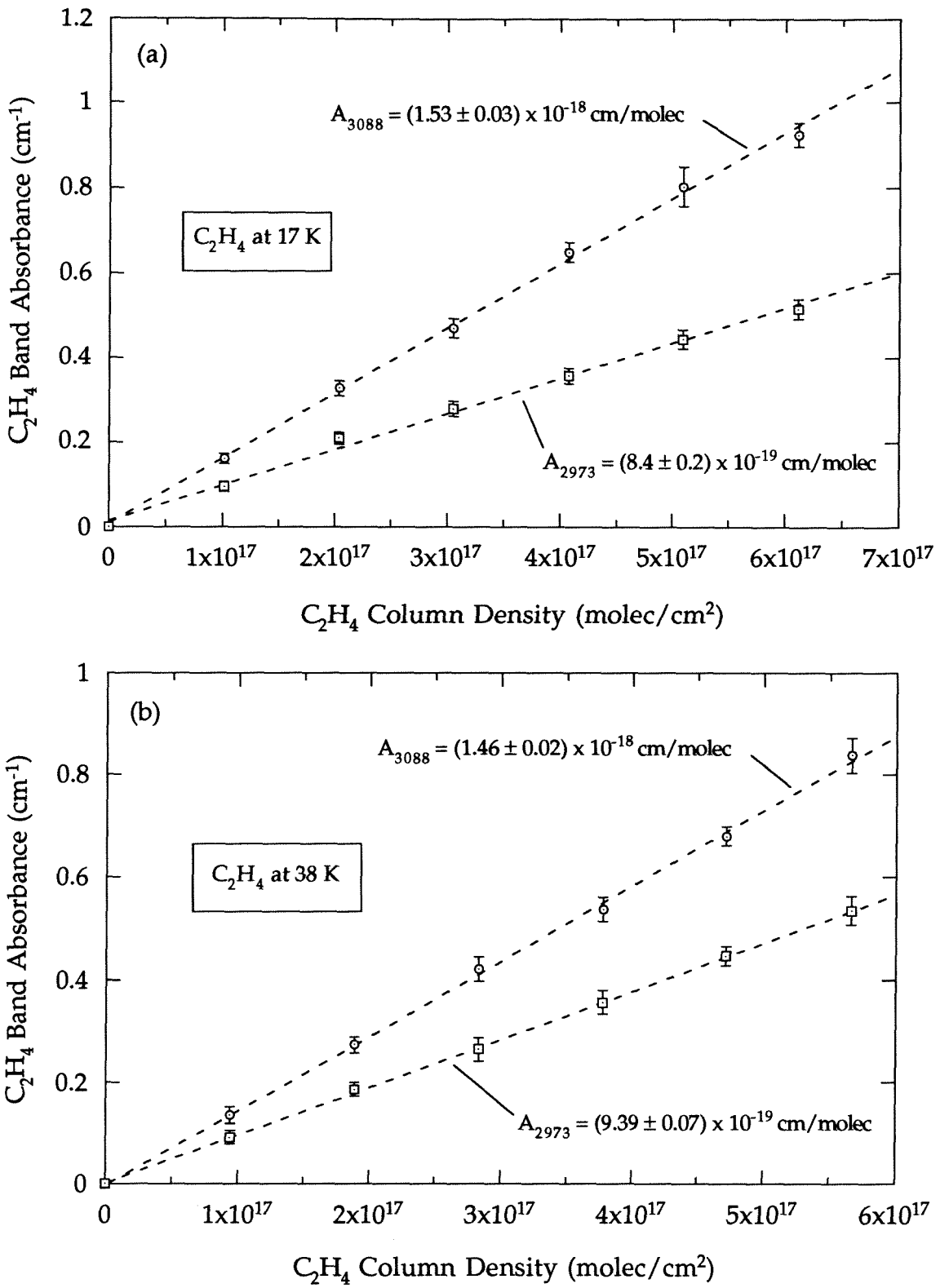

Figure 2.5. C_2H_4 ν_9 (3088 cm^{-1}) and ν_{11} (2973 cm^{-1}) integrated band absorbance determinations at (a) 17 K and (b) 38 K.

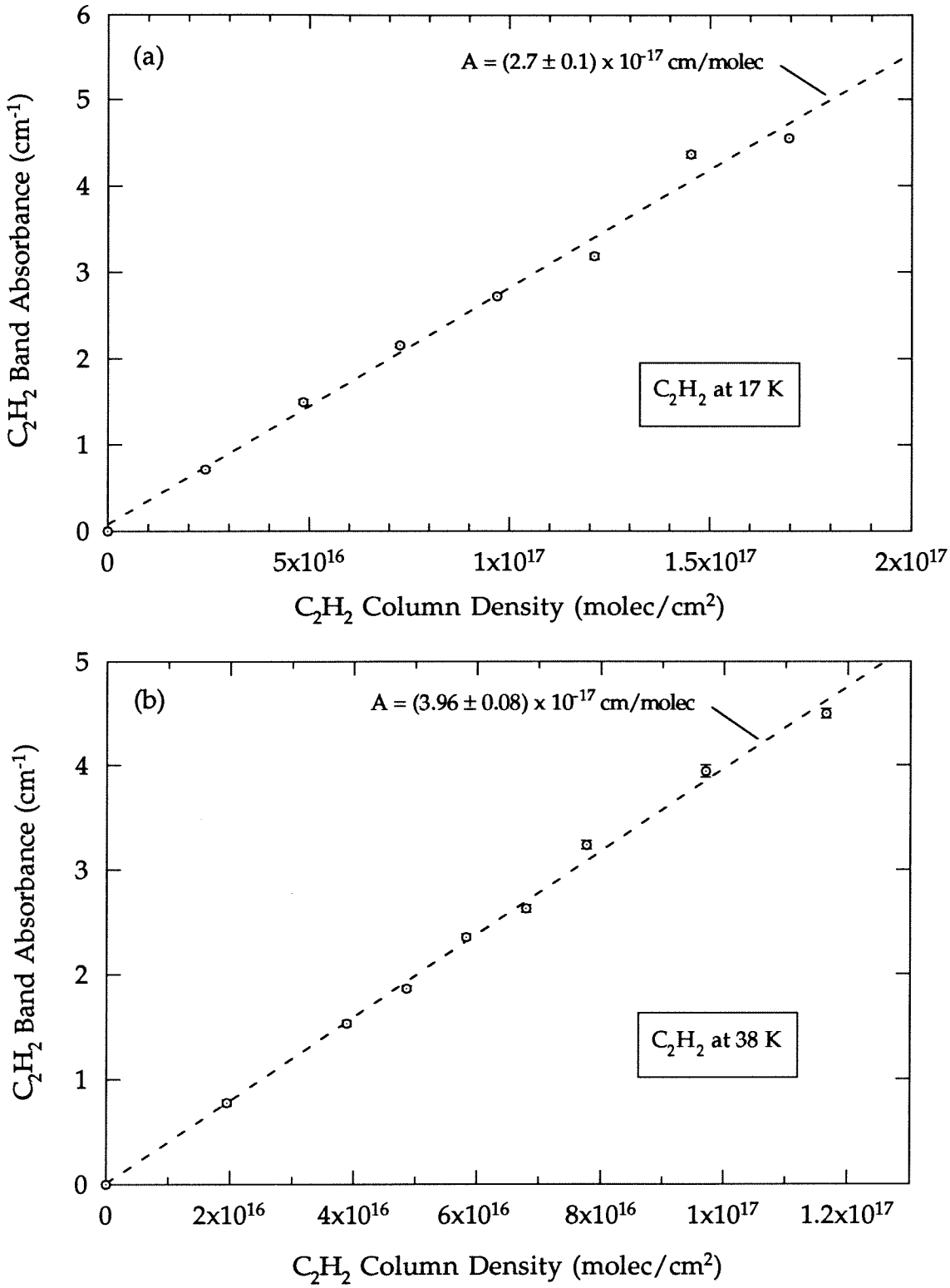

Figure 2.6. C_2H_2 ν_3 (3223 cm^{-1}) integrated band absorbance determinations at (a) 17 K and (b) 38 K.

Table 2.2. Integrated Absorbance Values for Selected C_2H_2 and C_2H_4 Bands at 17 K and 38 K (cm/molecule)

	17 K	38 K
C_2H_2 ν_3 Band (3224 cm^{-1})	$2.7 \pm 0.1 \times 10^{-17}$	$3.96 \pm 0.08 \times 10^{-17}$
C_2H_4 ν_9 Band (3088 cm^{-1})	$1.53 \pm 0.03 \times 10^{-18}$	$1.46 \pm 0.02 \times 10^{-18}$
C_2H_4 ν_{11} Band (2973 cm^{-1})	$8.4 \pm 0.2 \times 10^{-19}$	$9.39 \pm 0.07 \times 10^{-19}$

To understand how sensitive the band strengths of both species are to the C_2H_2/C_2H_4 ratio, C_2H_2+C_2H_4 mixtures of known composition were deposited, and both the band strengths and positions were measured. The results for the C_2H_2 ν_3 band over the full solid solution of C_2H_2 + C_2H_4 are shown in Fig. 2.7 (a) and (b). As the band positions are diagnostic of the C_2H_2/C_2H_4 ratio within a particular ice sample, this inferred ratio in the photolysis experiments is used to determine an appropriate value of the integrated band absorbance.

To interpret the photolysis experiments done on C_2H_4 in an N_2 matrix, similar measurements of the band strength and position of both the C_2H_2 and C_2H_4 features were taken for different degrees of dilution in N_2. These measurements were done at 17 K, as the vapor pressure of solid N_2 rapidly increases above this temperature, making it difficult to deposit and maintain an ice sample. Spectra showing the effect of dilution in N_2 on the C_2H_4 ν_9 and ν_{11} bands are shown in Figure 2.8 (a), and similarly for the C_2H_2 ν_3 band in Figure 2.8 (b). Note the splitting of the C_2H_2 ν_3 band, while the C_2H_4 bands only shift to higher energies. The measured integrated band absorbances and band positions for both C_2H_4 and C_2H_2 as a function of dilution in an N_2

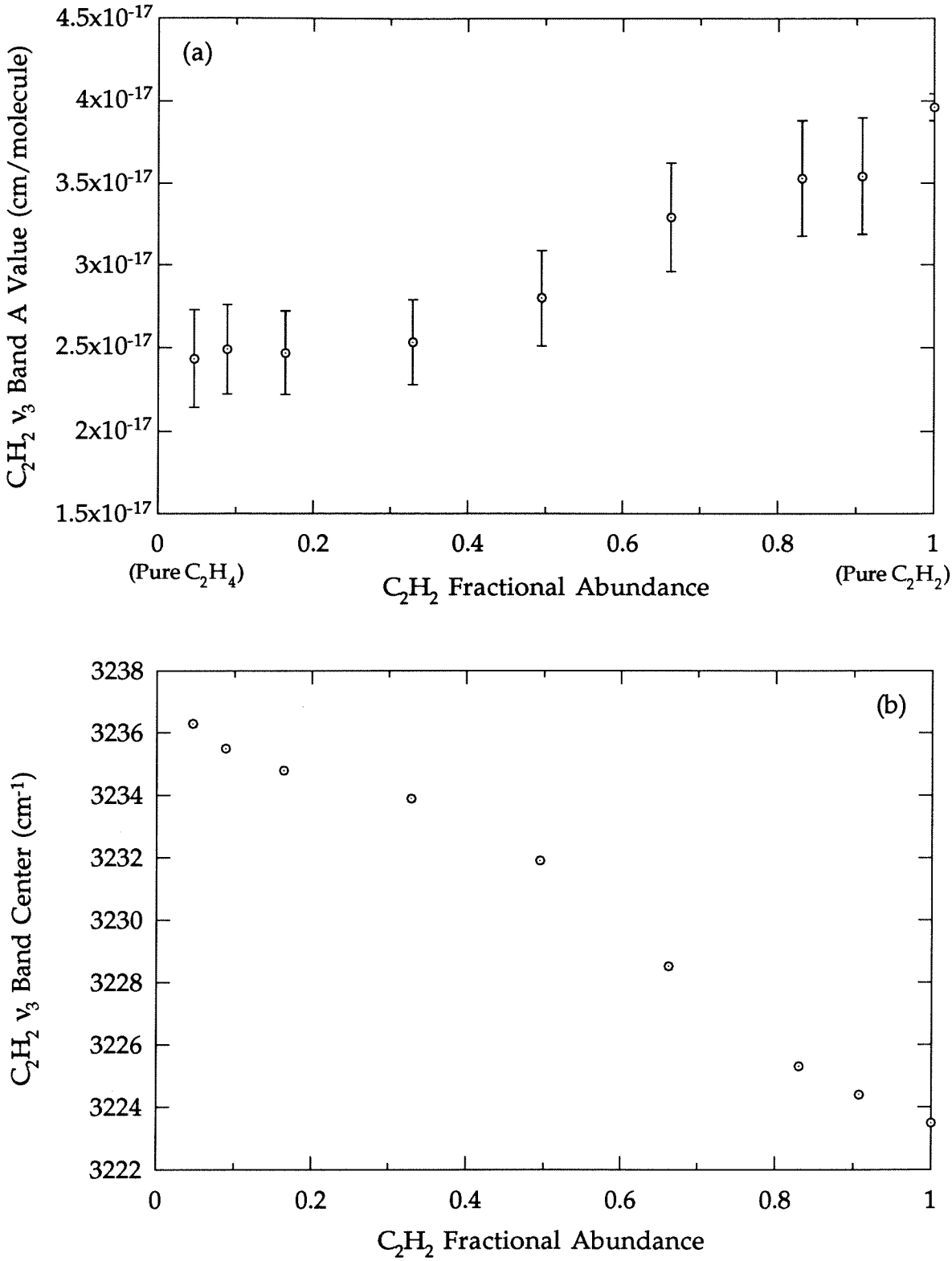

Figure 2.7. C_2H_2 ν_3 (a) A values and (b) band centers as a function of dilution in C_2H_4 matrix.

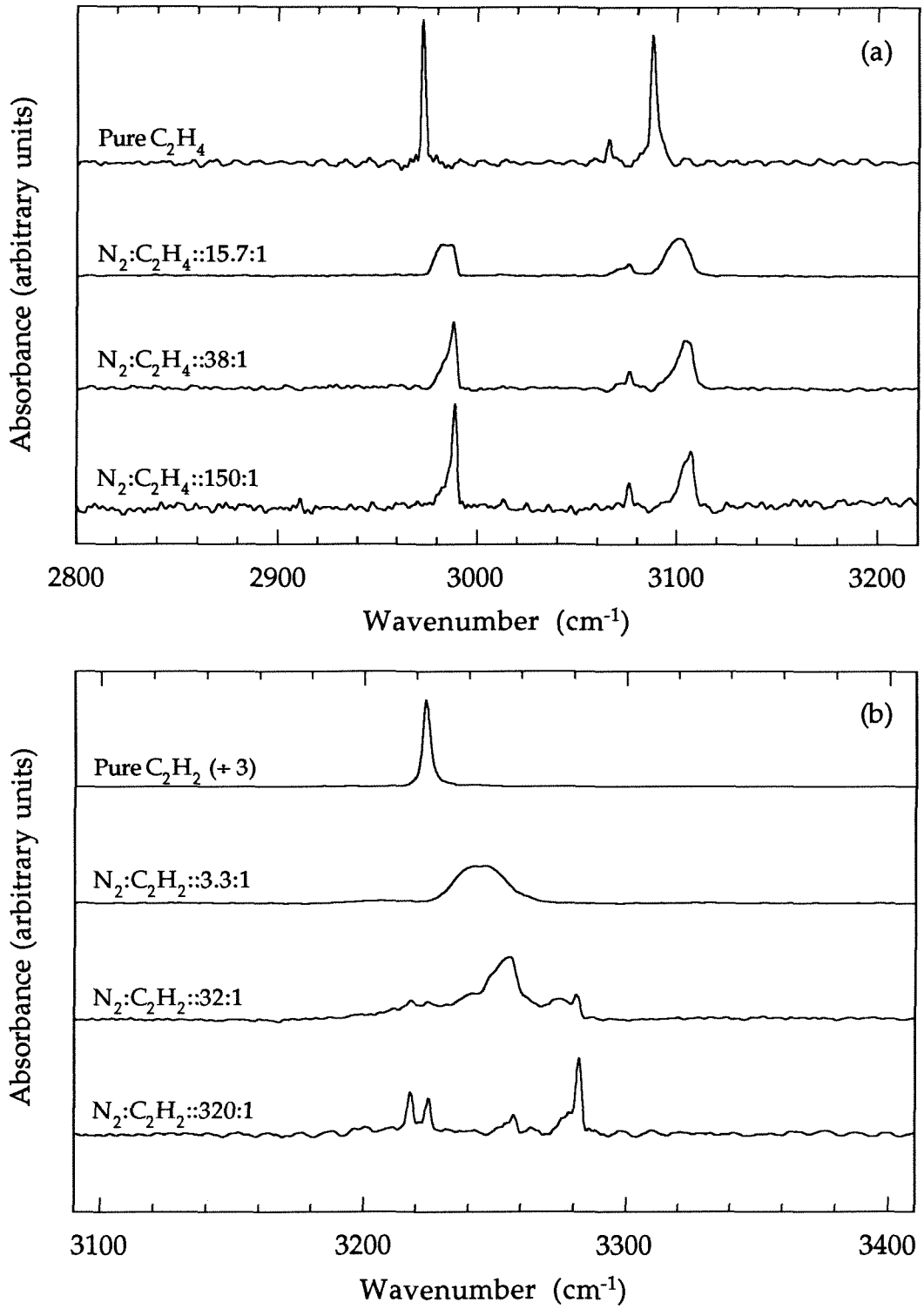

Figure 2.8. Spectra as a function of dilution in N_2 matrix for (a) the ν_9 and ν_{11} bands of C_2H_4, and (b) the ν_3 band of C_2H_2.

matrix are shown in Figures 2.9 and 2.10, respectively. All band positions have an uncertainty of ± 1 cm^{-1}, the spectrometer resolution.

To quantify the change in absorbance of both the C_2H_2 and C_2H_4 bands as a function of radiation fluence, band integrations were measured on the difference of the spectra before and after a given radiation dose, rather than on the absolute spectra. Such difference spectra would be expected to show an increase in the C_2H_2 ν_3 band, and a corresponding decrease in the C_2H_4 features. While this was generally true, quantitative interpretation of the C_2H_4 features was often more difficult than this simple description implies.

Figure 2.11 shows examples of the range encountered in the measured spectra. As the band changes in C_2H_4 in the lower spectrum show both positive and negative features, it is not obvious that the integrated area under each band represents the change in C_2H_4 column abundance. In addition, the change in C_2H_4 column abundance inferred from the ν_9 feature was often quite different than that inferred from the ν_{11} band.

The C_2H_4 changes became systematically more difficult to interpret as ice sample thickness was increased. While it is possible that this is caused by the cryopumping of C_2H_4 onto the sample from other parts of the vacuum chamber, this was considered unlikely, as samples that were not irradiated showed no change in C_2H_4 column density when left at 38 K over a period of several hours.

Alternatively, the observed C_2H_4 band changes could be due to annealing caused by the UV radiation. Annealing may arise from the heat generated by the kinetic energy of reaction products being absorbed by the matrix, or the direct transfer of energy from photoexcited ethylene ($C_2H_4^*$) to the lattice. Annealing is generally thought to sharpen absorbance features by making the local electronic environments more uniform, as occurs in the

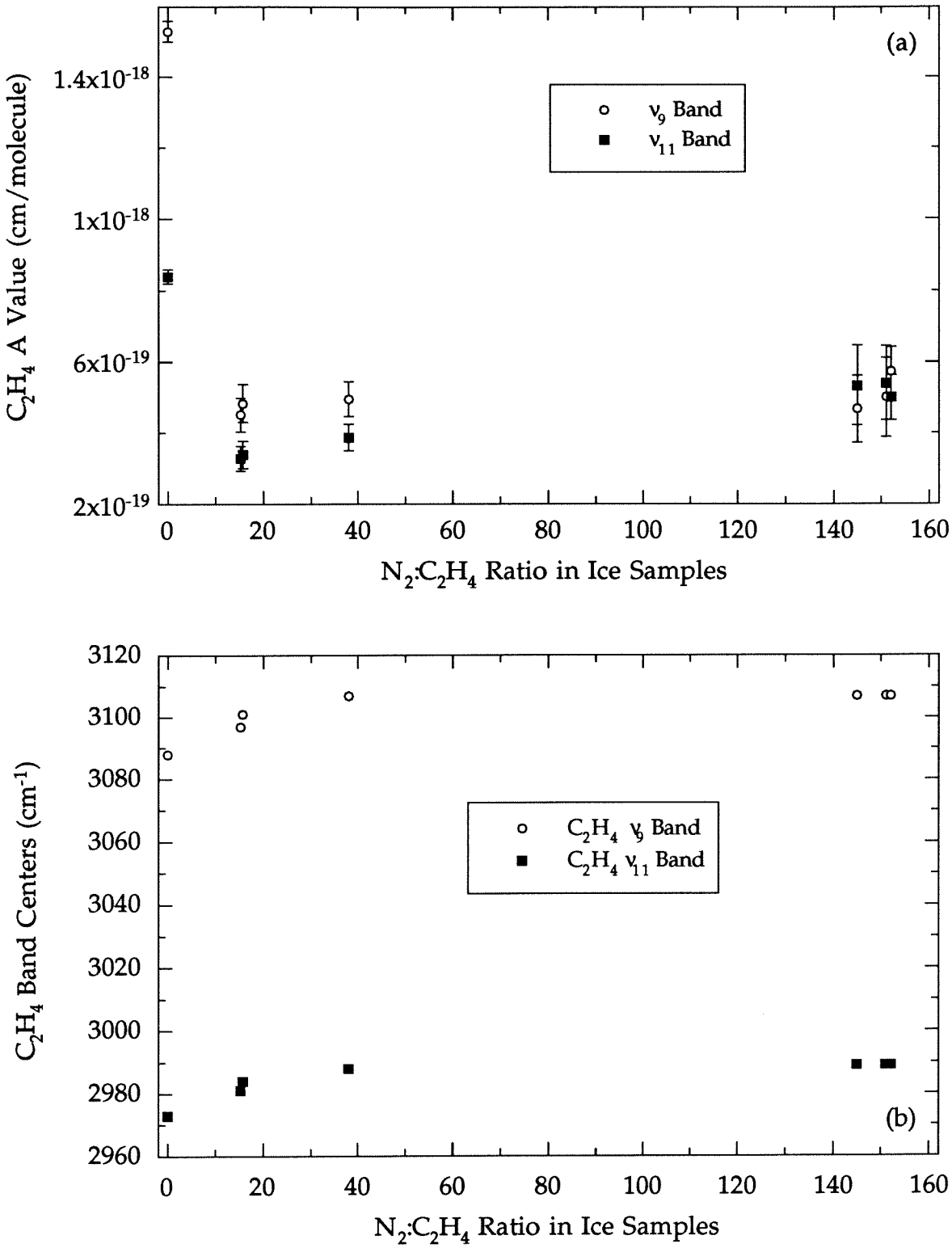

Figure 2.9. C_2H_4 ν_9 and ν_{11} (a) A values and (b) band centers as a function of dilution in N_2 matrix.

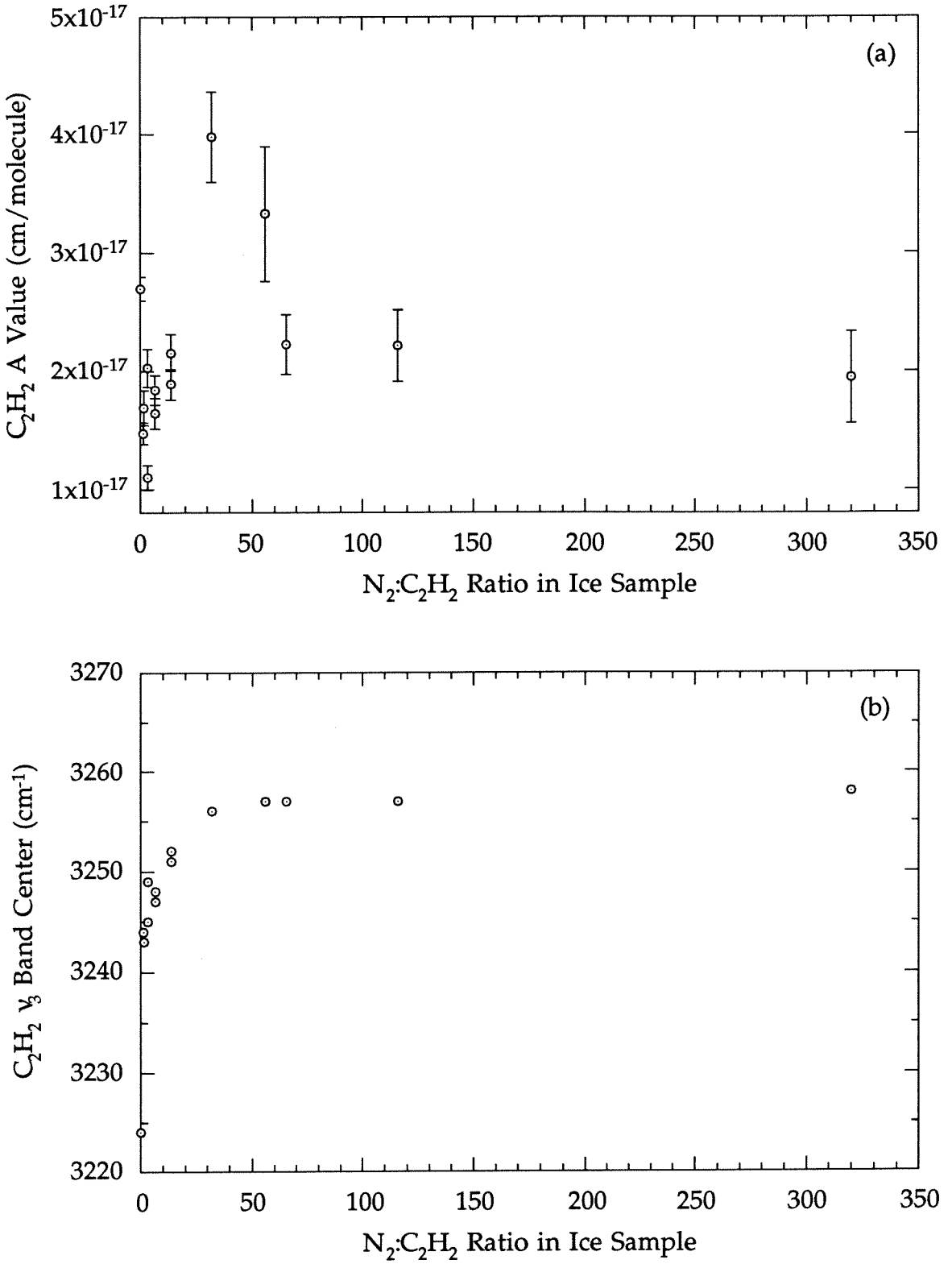

Figure 2.10. C_2H_2 ν_3 (a) A values and (b) band centers as a function of dilution in N_2 matrix.

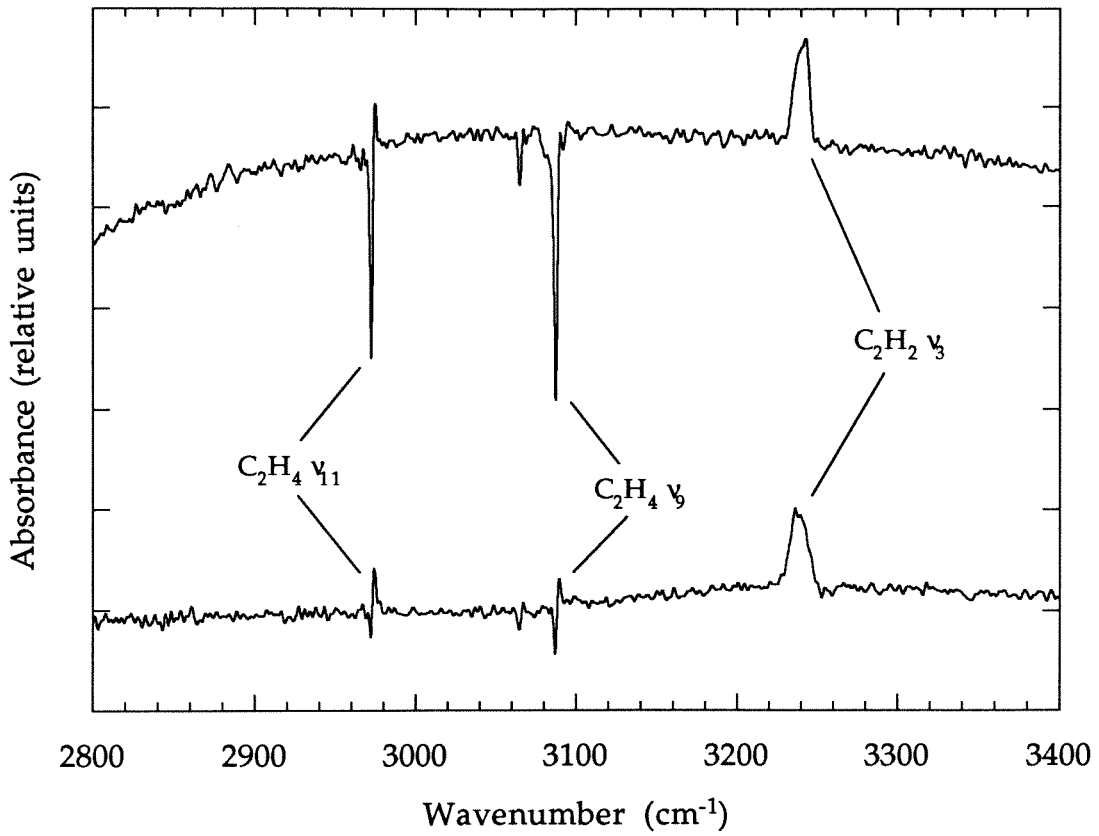

Figure 2.11. An example of typical difference spectra used to determine absolute changes in C_2H_4 and C_2H_2 column abundances.

transition from an amorphous to crystalline state. Such phase changes may cause differences in band strength as well. If, for example, the average integrated band strength of an ice sample were to increase as a result of irradiation induced annealing, then the size of a band may actually increase even though the column density had actually decreased. Such local heating caused by the radiation may affect thick samples more than thin, if the thermal conductivity of the ice were very low, as has been reported (Kouchi *et al.* 1992). Large thermal gradients could then be supported more easily in thick samples, so that multiple phases may be observed through the ice

column. In fact, possible phase changes in C_2H_4 at low temperatures have been reported (Jacox 1962; Rytter and Gruen 1979), although there is no consensus on this.

If annealing caused by radiation affects band strengths, then perhaps pre-annealing the sample by heating it before the irradiation would help clarify the difference spectra. This was tried, by heating the deposited C_2H_4 ice to 60 K, just below the sublimation temperature, and letting the sample sit for three hours. The sample was then recooled to 38 K, and irradiated several times. The final result was no different than having just irradiated the sample without pre-annealing, and in fact, the spectra in Figure 2.11 are taken from this experiment. Although band shapes and positions were seen to change due to sample heating, the bands reverted back to their original shapes and positions upon recooling. This would argue that phase changes, rather than true annealing, were responsible for the band changes, as annealing is not a reversible process.

Figure 2.12 summarizes the data from the hydrogen lamp irradiation of pure C_2H_4 ice samples, with 2.12 (a) showing the trends in C_2H_4, and (b) showing the trends in C_2H_2. Figures 2.13 (a) and (b) show the corresponding data for irradiation by the mercury lamp. The error bars are again largely due to uncertainty in spectral baselines. In addition, as only the change in band sizes due to photolysis was measured in the difference spectra, the errors propagate through to each successive measurement when determining absolute abundances. The error between two successive measurements is thus smaller than indicated by the size of the error bars.

As can be seen in Figures 2.12 and 2.13, several different thicknesses of ice were irradiated with each lamp. The thicknesses covered a range of optical depths for the UV radiation, from samples that were less than optical depth

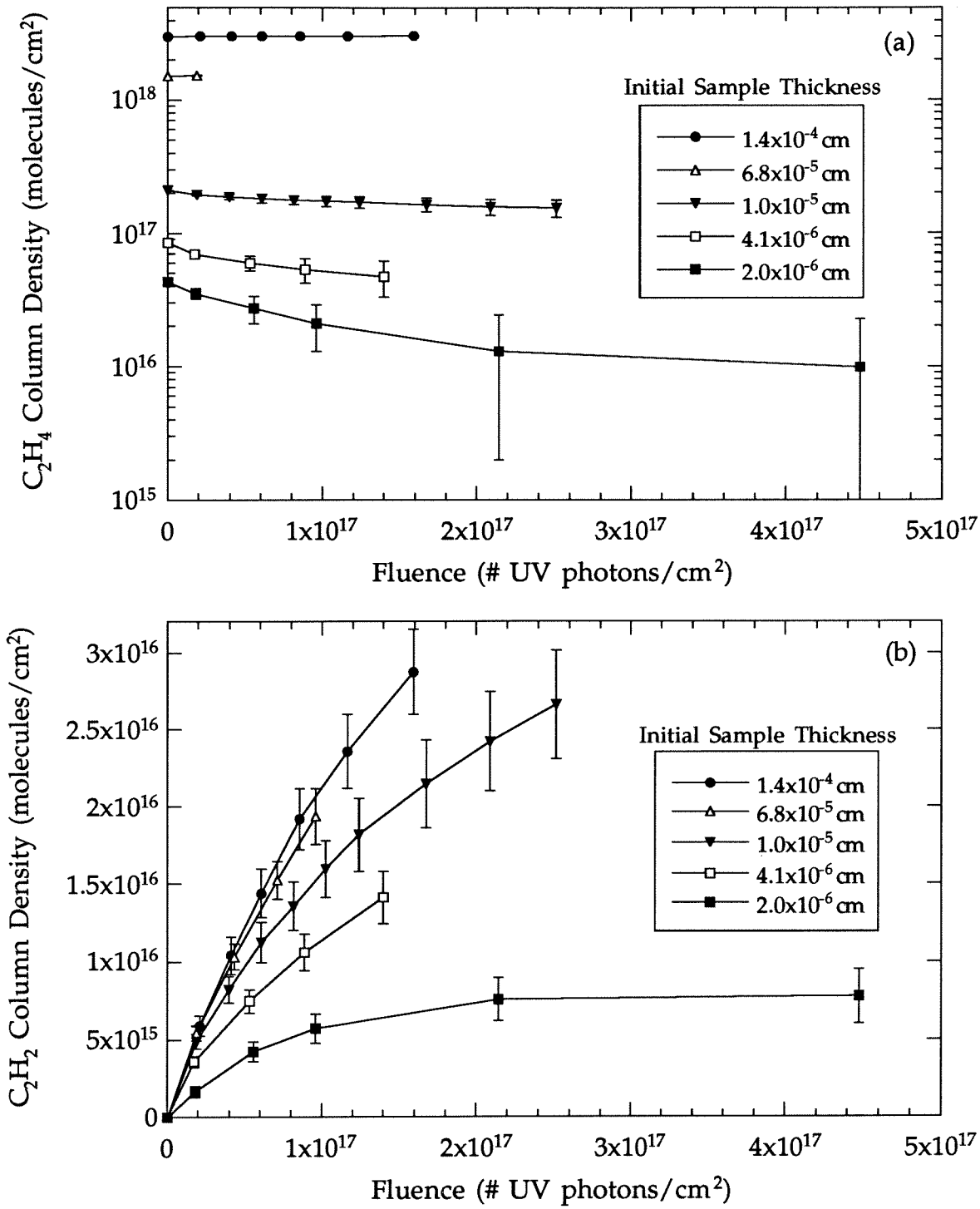

Figure 2.12. Column density changes of (a) C_2H_4 and (b) C_2H_2 due to the H_2 lamp irradiation of pure C_2H_4. The samples varied only in initial thickness. C_2H_4 abundances are shown only as inferred from the ν_9 band (3088 cm^{-1}). Errors are primarily from uncertainties in the baseline of the measured IR bands. The lines between data points serve only as a visualization aid.

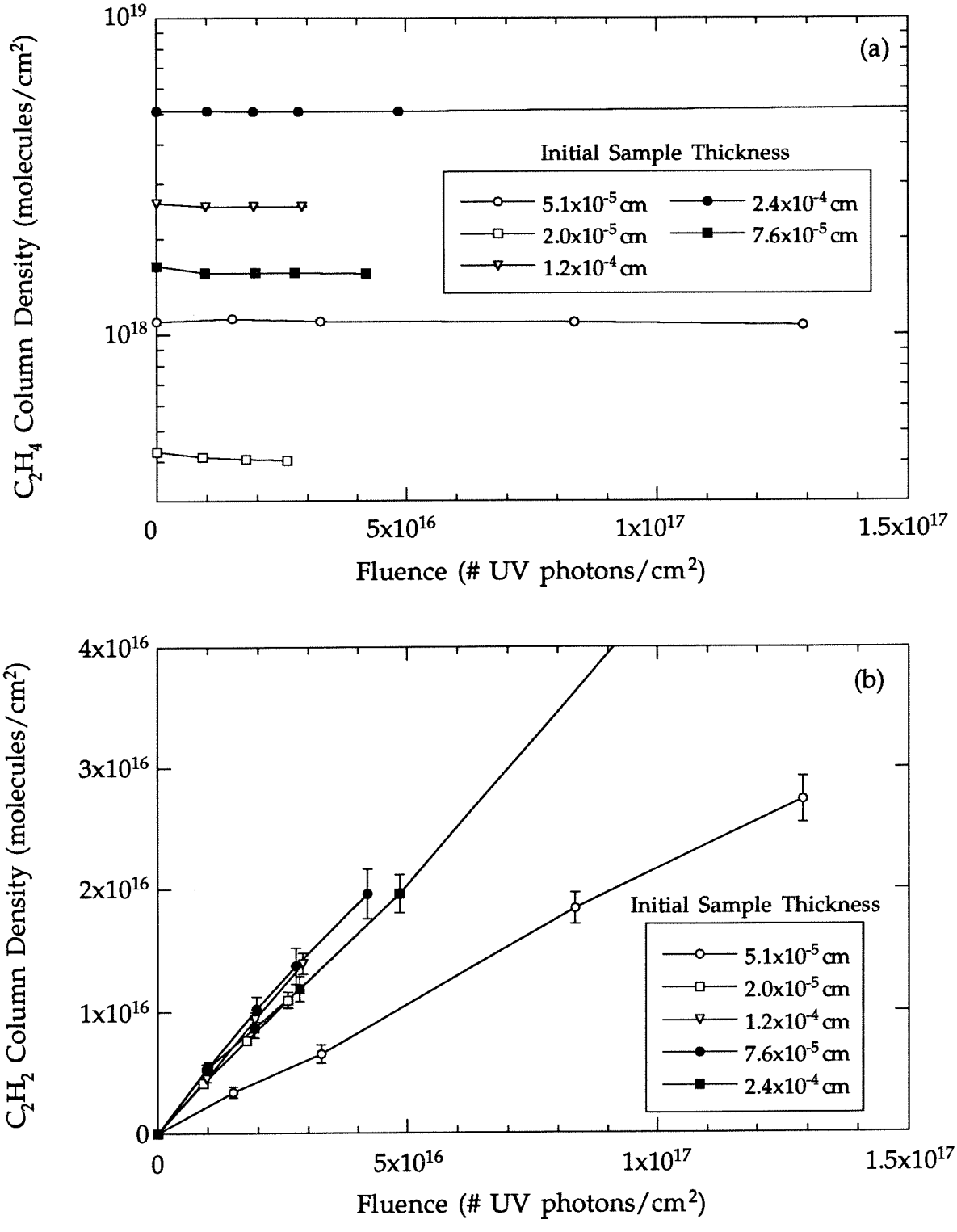

Figure 2.13. Column density changes of (a) C_2H_4 and (b) C_2H_2 due to the Hg lamp irradiation of pure C_2H_4. Note that the data trends are not as clean as the results for the H_2 lamp irradiation shown in Fig. 2.12.

unity to those that were opaque to virtually all the incident UV radiation. The purpose of this variation was to provide information on the UV cross-section of solid state C_2H_4, discussed later in this paper.

The results of irradiating C_2H_4 under various degrees of dilution in an N_2 matrix are shown in Figures 2.14 and 2.15, for the H_2 and Hg lamps, respectively. It is immediately evident that the same conversion of C_2H_4 to C_2H_2 is occurring even when the ethylene is quite dilute. This argues strongly in favor of a unimolecular dissociation process governing this reaction, as any bimolecular process would be expected to slow as the dilution increased.

2.5. Interpretation of Results

To properly model the effect of photolysis in the solid state, it is important to realize that the ice samples are optically thick to the incident UV radiation. Since all abundance determinations are measured over the full column of each ice sample, many different environments are being viewed simultaneously, which complicates the interpretation. The kinetics must be independently determined at each depth in the ice sample, and then integrated to try and match the observed column abundances.

Given that the only species spectroscopically observed in these experiments were C_2H_4 and C_2H_2, the kinetics can only be constrained by the abundance evolution of these species. The model reaction network invoked is shown below:

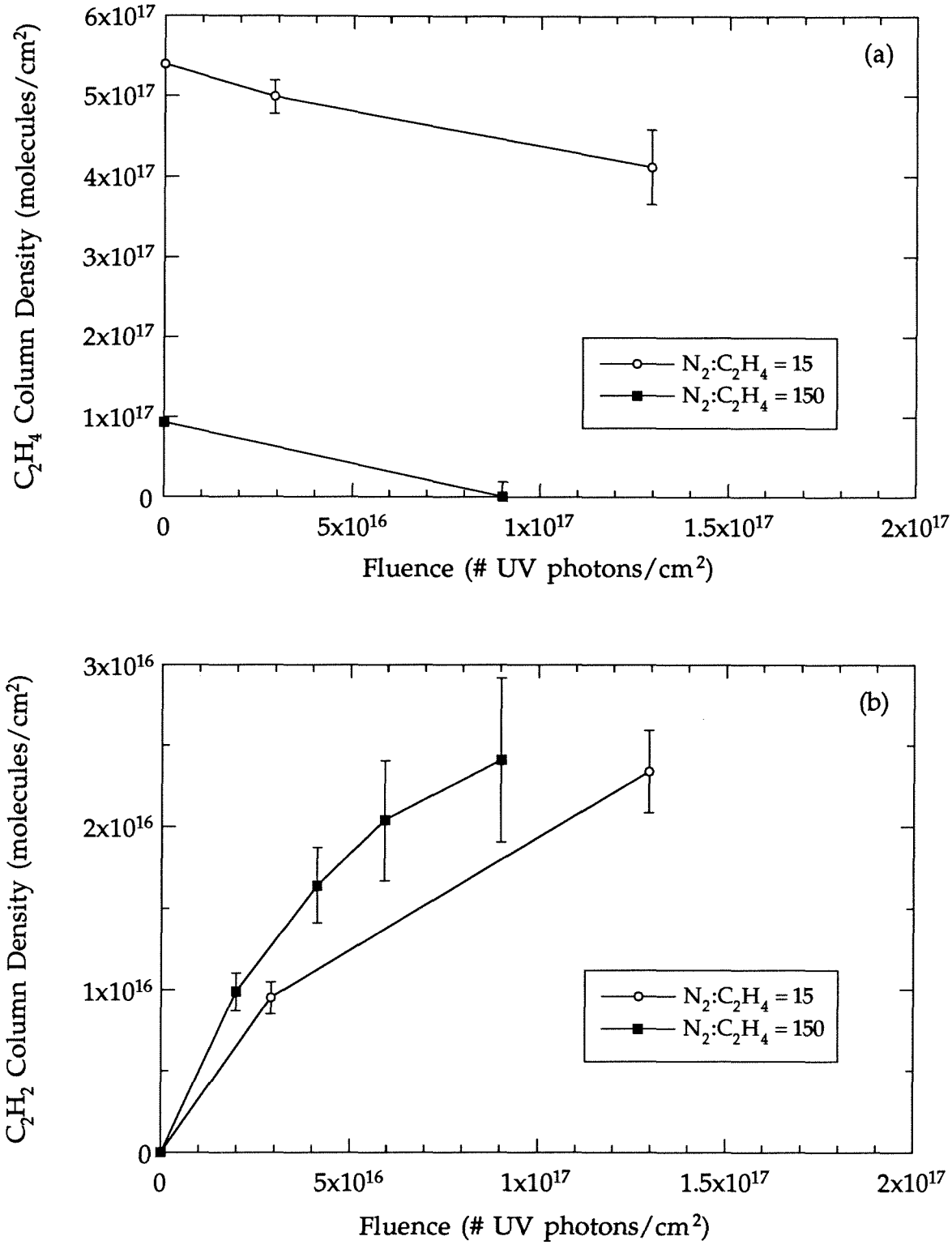

Figure 2.14. Column density changes of (a) C_2H_4 and (b) C_2H_2 due to the H_2 lamp irradiation of N_2:C_2H_4 mixtures. Note that dilution does not affect C_2H_2 production.

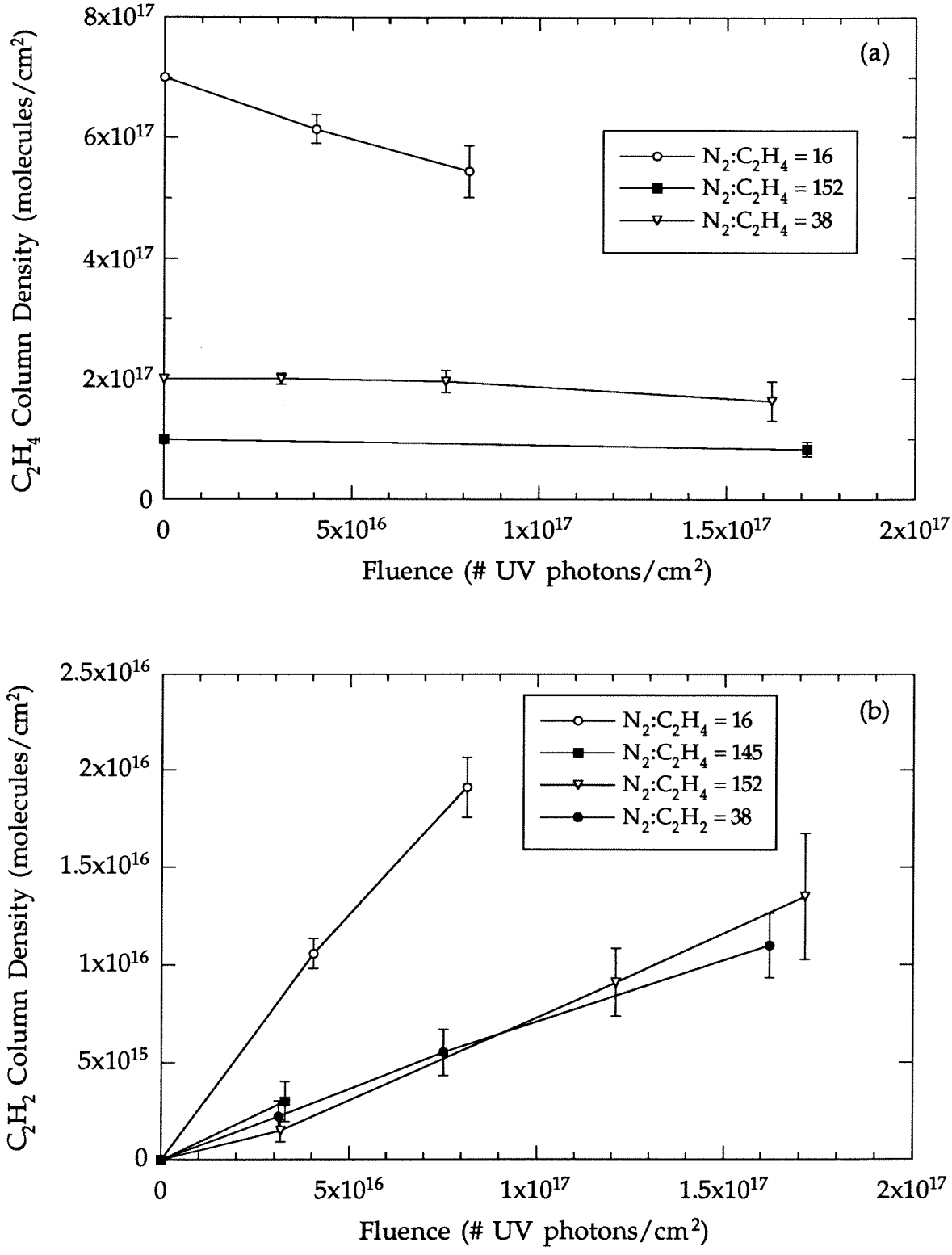

Figure 2.15. Column density changes of (a) C_2H_4 and (b) C_2H_2 due to the Hg lamp irradiation of N_2:C_2H_4 mixtures.

$$C_2H_4 + h\nu \xrightarrow{k_1} C_2H_2 + (H_2, 2H) \quad (15)$$

$$\xrightarrow{k_2} \text{other products} \quad (16)$$

$$k = k_1 + k_2 \quad (17)$$

$$C_2H_2 + h\nu \xrightarrow{k_3} \text{products} \quad (18)$$

Including the loss process for C_2H_2 is motivated by the results of irradiating pure C_2H_2 ice, which was tried only with the hydrogen lamp. The results of this are shown in Figure 2.16, with acetylene clearly being destroyed by UV

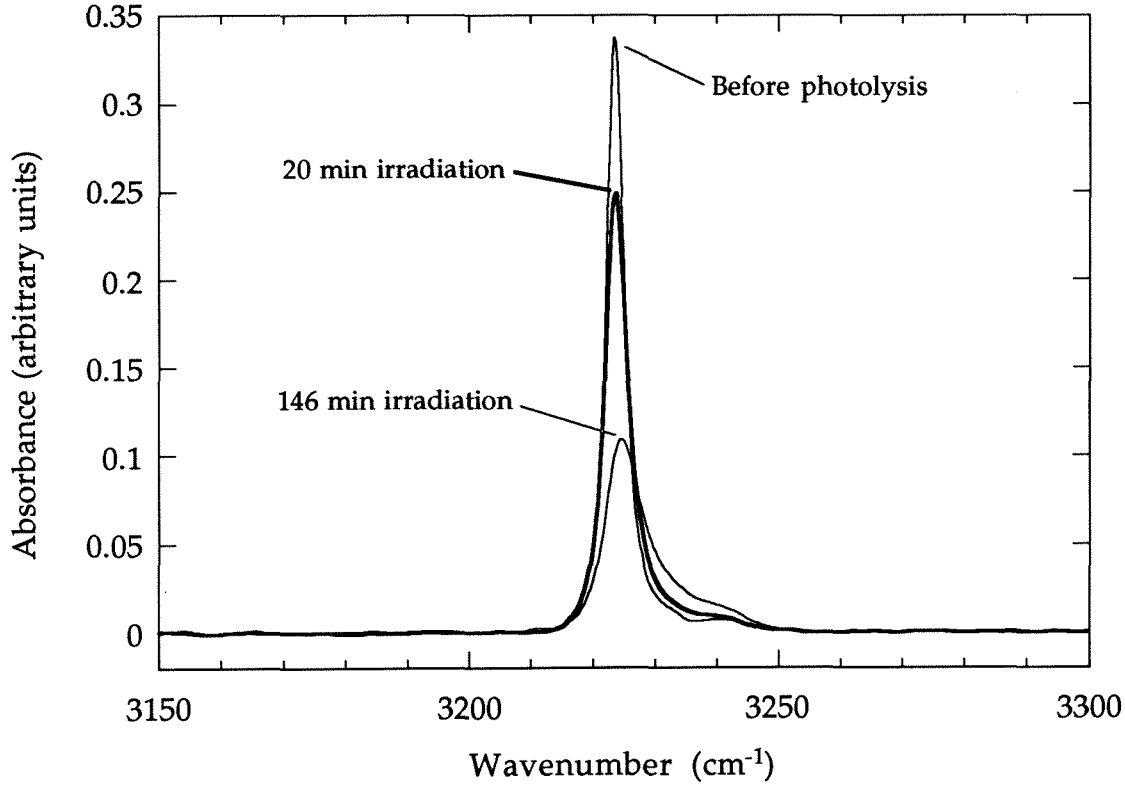

Figure 2.16. Photolysis of pure C_2H_2 by the H_2 lamp. Initial sample thickness was ~ 4×10^{-6} cm.

photolysis as well. Although the C_2H radical has been shown to be the primary product in the gas phase (Okabe 1983), no new spectral features were observed as a result of this photolysis. A further description of solid state

acetylene photolysis is beyond the scope of the present paper, but we hope to study this in the near future.

Ion molecule processes are not considered to play a role in these experiments, as the ionization potential of C_2H_4 is 10.4 eV, corresponding to a UV wavelength of 1190 Å that is more energetic than any radiation used. It should be pointed out, however, that ionization potentials in the solid state may be lower than their corresponding values in the gas phase (Gorden and Ausloos 1971), so that some photoionization may be occurring in response to irradiation by the hydrogen lamp.

The kinetics for the reaction series outlined above in equations (15) - (18) are thus governed by the following:

$$\frac{d[C_2H_4](z,t)}{dt} = -k[C_2H_4](z,t), \tag{19}$$

$$\frac{d[C_2H_2](z,t)}{dt} = k_1[C_2H_4](z,t) - k_3[C_2H_2](z,t). \tag{20}$$

The species number densities are dependent on both depth and time for optically thick ices. The rate coefficients are defined as shown below:

$$k = \phi\sigma I(z,t), \tag{21}$$

where, using k in equation (19) as an example, ϕ is the quantum yield for C_2H_4 destruction [# molecules destroyed/incident photon], σ is the cross section for C_2H_4 [cm^2], and $I(z,t)$ is the incident UV radiation flux [photons cm^{-2} sec^{-1}], so that k has units of sec^{-1}.

Equations (19) and (20) can be solved analytically, with the solutions given as follows:

$$[C_2H_4](z,t) = [C_2H_4]_0(z)\exp(-kt) \tag{22}$$

$$[C_2H_2](z,t) = \frac{k_1}{k_3 + k}[C_2H_4]_0(z)\{\exp(-kt) - \exp(-k_3 t)\} \tag{23}$$

These solutions assume that the UV cross section is constant over both depth and time. Such an assumption is reasonable to first-order, as the cross sections for C_2H_4 and C_2H_2 are similar for most of the vacuum UV (Zelikoff and Watanabe 1953; Wu *et al.* 1989), so that even as the chemistry of the ice is changing, the average cross section is not. This may not be valid if there are other products formed in significant quantities that have cross sections substantially different than C_2H_4.

The column densities of C_2H_4 and C_2H_2 can be found by simply integrating over the sample thickness:

$$N(t) = \int_0^d n(z,t)dz \tag{24}$$

The column density can then be determined as a function of total fluence, as the UV flux is monitored continuously during photolysis.

In this model, the column of ice is divided into 100 depth steps, and equations (22) and (23) are then used to determine the number densities of C_2H_4 and C_2H_2 as a function of depth for a given fluence, leaving the UV cross section, k, k_1, and k_3 as free parameters. The sum over these depth steps provides the column density. These values are then compared to the data for

the same fluence level, and the differences between them are minimized using a least-squares approach over the full data set for a particular photolysis experiment. That is, the curves are fit to the data for C_2H_2 and C_2H_4 simultaneously. The trends for the ν_9 band of C_2H_4 were less scattered than those for the ν_{11} band, so the C_2H_4 data was only fit to the former. In addition, if no common set of parameters could provide a good fit for both the C_2H_4 and C_2H_2 data trends, fitting the C_2H_2 was given priority, as the estimated errors for the ν_3 band were systematically smaller than those for ethylene.

Figures 2.17 and 2.18 show typical fits for photolysis with the H_2 lamp and Hg lamp, respectively. The fits for photolysis by the H_2 lamp are better than those for the Hg lamp, perhaps due to variability in the fractional flux of the 1849 Å line, as discussed in Appendix B. Another possible reason for the discrepancy is that the UV penetration scale length is changing substantially with time, so that equations (22) and (23) are no longer adequate to describe the species evolution.

The parameters providing the best fit for each photolysis experiment are summarized in Table 2.3, for both pure and dilute samples of C_2H_4. The large error bars provide a fair degree of latitude in choosing the fit parameters for each experiment. Each experiment was fit separately, and the mean and standard deviation were determined from the full set of experiments. It is hoped that no systematic judgements were made among the fits, so that the standard deviation is representative of only random experimental error. The averages and standard deviations do not include the dilute samples.

As the model characterizes the UV radiation field in terms of the penetration scale length, cross sections for the non-dilute samples are determined from this scale length, assuming an ice density of 1 g/cm^3. The

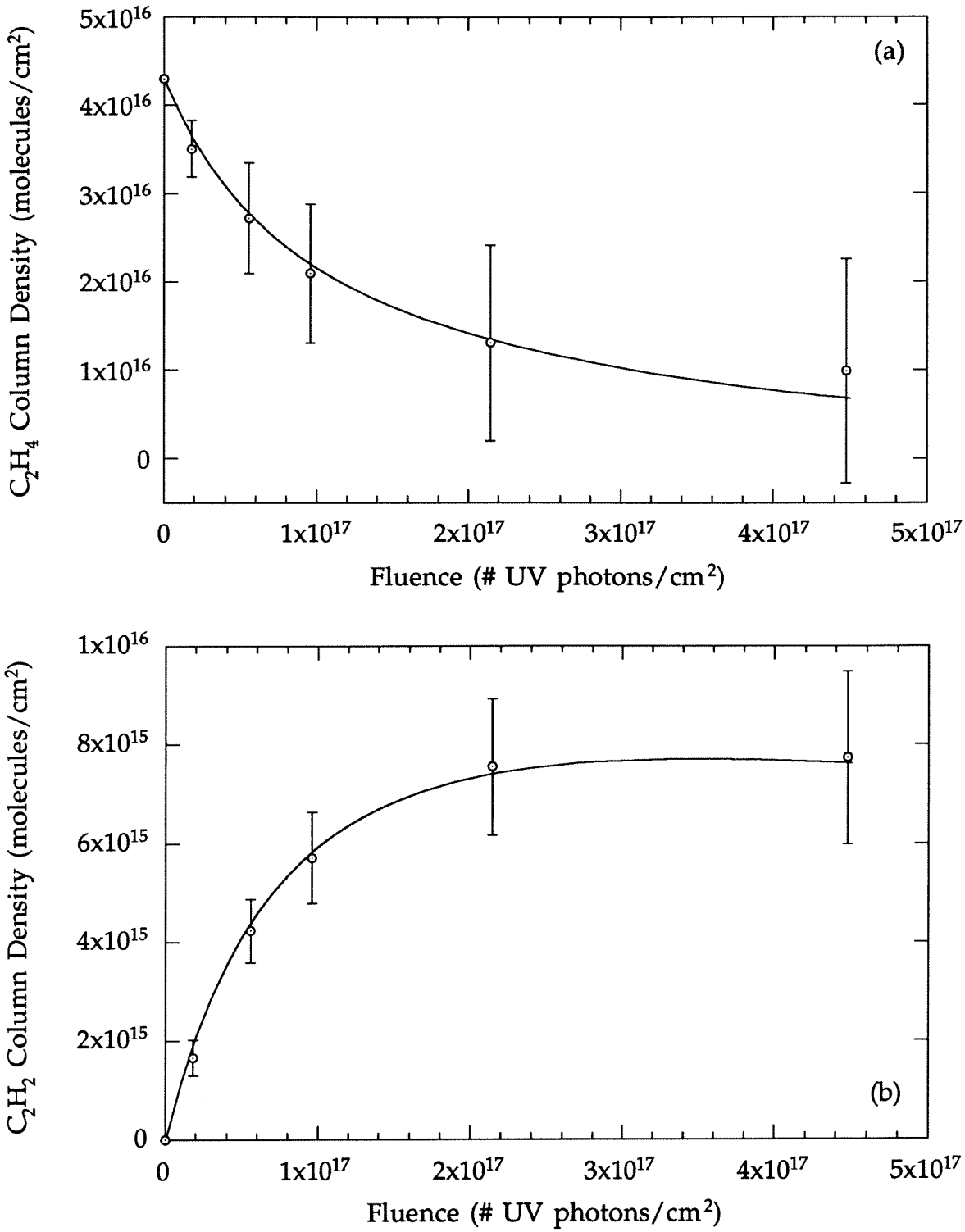

Figure 2.17. Examples of fits to the trends of (a) C_2H_4 and (b) C_2H_2 for photolysis with the H_2 lamp.

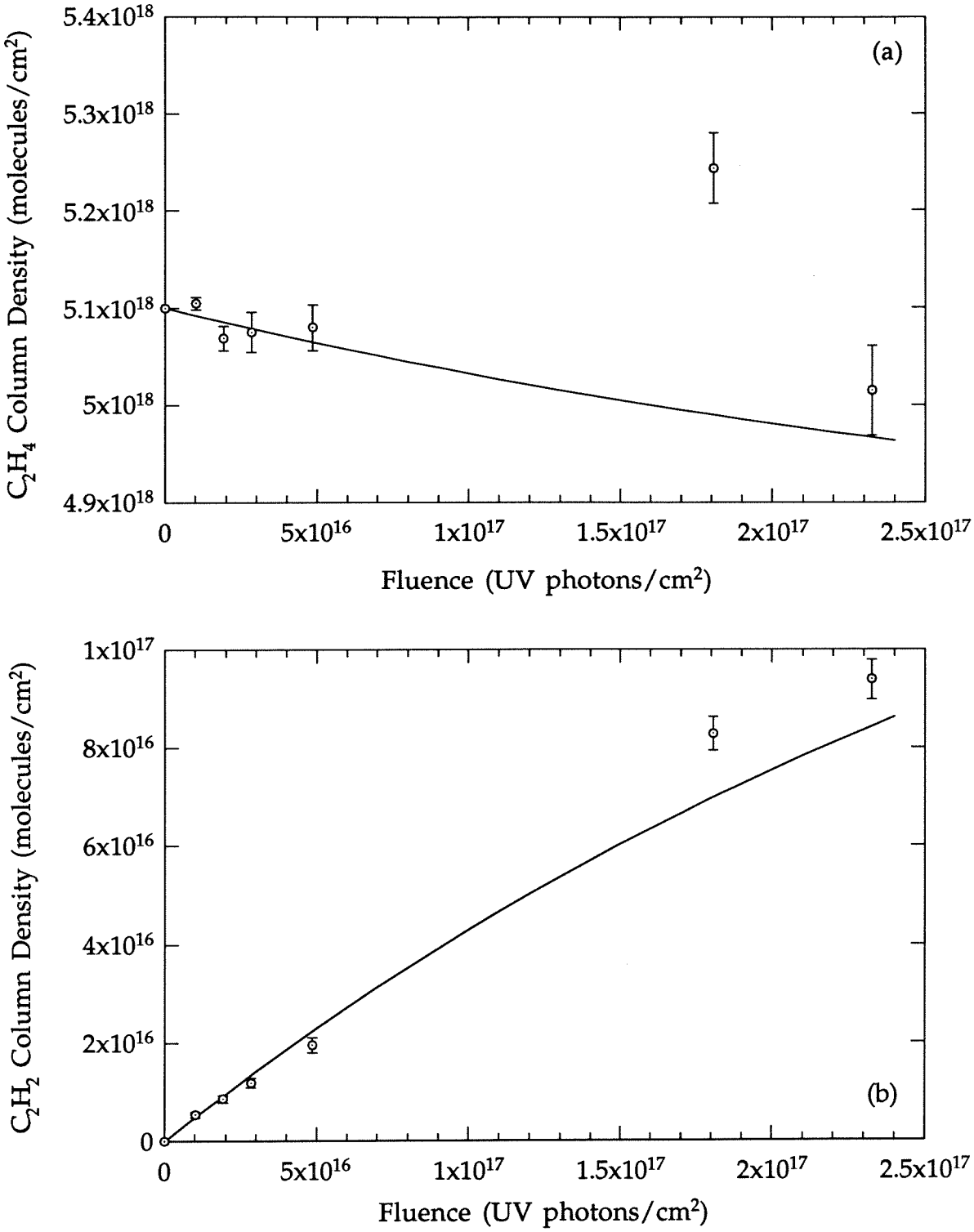

Figure 2.18. Examples of fits to the trends of (a) C_2H_4 and (b) C_2H_2 for photolysis with the Hg lamp. The disparity between fits and data are discussed in the text.

Lamp	Sample	Temp. (K)	Initial C_2H_4 (molec/cm^2)	k/I (cm^2)	k_1/I (cm^2)	k_3/I (cm^2)	UV scale length (cm)	Cross-section (cm^2)
H_2	C_2H_4	38	4.3E+16	5.0E-17	1.4E-17	2.2E-18	5.0E-07	9.3E-17
H_2	C_2H_4	38	8.5E+16	2.5E-17	1.1E-17	1.5E-18	9.0E-07	5.2E-17
H_2	C_2H_4	38	2.1E+17	2.1E-17	1.0E-17	3.0E-19	1.2E-06	3.9E-17
H_2	C_2H_4	38	1.5E+18	1.5E-17	1.2E-17	0	1.0E-06	4.7E-17
H_2	C_2H_4	38	3.0E+18	1.5E-17	8.8E-18	0	1.5E-06	3.1E-17
			Mean	2.5E-17	1.1E-17	8.0E-19	1.0E-06	4.6E-17
			Std. Deviation	1.4E-17	2.0E-18	1.0E-18	3.7E-07	1.7E-17
H_2	N_2:C_2H_4=15	17	5.4E+17	3.0E-17	6.5E-18	3.0E-18	4.5E-05	1.6E-17
H_2	N_2:C_2H_4=150	17	9.3E+16	3.7E-17	1.1E-17	0	6.0E-04	1.1E-17
Hg	C_2H_4	38	4.3E+17	2.0E-17	7.4E-18	0	3.0E-06	1.6E-17
Hg	C_2H_4	38	4.5E+17	5.0E-18	3.5E-18	0	5.0E-06	9.3E-18
Hg	C_2H_4	38	6.4E+17	3.0E-17	1.1E-17	2.0E-18	3.0E-06	1.6E-17
Hg	C_2H_4	38	8.1E+17	2.5E-17	6.8E-18	0	4.0E-06	1.2E-17
Hg	C_2H_4	38	8.1E+17	8.0E-18	2.0E-18	0	6.0E-06	7.8E-18
Hg	C_2H_4	38	1.1E+18	5.0E-18	3.0E-18	0	4.0E-06	1.2E-17
Hg	C_2H_4	38	1.6E+18	2.0E-17	4.5E-18	2.0E-18	6.0E-06	7.8E-18
Hg	C_2H_4	38	1.7E+18	1.0E-17	4.8E-18	0	6.0E-06	7.8E-18
Hg	C_2H_4	38	2.6E+18	3.0E-17	3.7E-18	0	7.0E-06	6.6E-18
Hg	C_2H_4	38	5.1E+18	6.0E-18	3.8E-18	0	6.0E-06	7.8E-18
			Mean	1.6E-17	5.1E-18	4.0E-19	5.0E-06	9.3E-18
			Std. Deviation	1.0E-17	2.7E-18	8.4E-19	1.4E-06	2.6E-18
Hg	N_2:C_2H_4=16	17	7.0E+17	1.0E-17	1.2E-18	0	2.0E-04	3.7E-18
Hg	N_2:C_2H_4=38	17	2.0E+17	4.0E-18	8.6E-19	0	2.0E-04	8.8E-18
Hg	N_2:C_2H_4=152	17	9.9E+16	2.0E-18	1.2E-18	0	1.0E-03	6.8E-18

Table 2.3. Summary of fit parameters for all photolysis experiments. The UV penetration scale length, k, k_1, and k_3 were the free parameters in each fit. Rate constants are given divided by the incident UV flux.

calculated average cross section of 4.6×10^{-17} cm^2 for the wavelength region of 1216 - 1700 Å provided by the H_2 lamp is less than a factor of two different than the corresponding gas phase C_2H_4 cross section of 3×10^{-17} cm^2 (at 1700 Å), discussed previously in Section 2.2. However, the calculated cross section of 9.3×10^{-18} cm^2 for 1849 Å by Hg photolysis is roughly 25 times larger for the solid state than the corresponding gas phase value of 3.7×10^{-19} cm^2. Since the model takes the cross section as constant for the duration of the photolysis, it represents an average value, both for all species and over time. As C_2H_4 and C_2H_2 have about the same cross section at 1849 Å, the bulk of the absorption may be due to other photolysis products with larger cross sections.

The inferred cross sections for the dilute C_2H_4 samples are similar to those for the pure samples, although they do generally appear somewhat smaller. It is possible that the calculated value for the C_2H_4 number density in the N_2 matrices is not very accurate (see Section 2.3.2), which would affect the cross section calculations. At present, the data are too sparse and uncertain to establish any trends due to dilution.

The quantum yield for ethylene destruction, as specified by eqn. (21), can be determined by dividing the given value for k/I by the cross section. For the hydrogen lamp, this gives a value of $\phi = 0.54 \pm 0.36$, suggesting that much of the incident radiation may ultimately be absorbed in the form of lattice vibrations. This may be quite reasonable, as the initially photoexited ethylene ($C_2H_4^*$) may decay into energetic vibrational states that couple with the lattice, transferring the energy into phonons that ultimately express themselves as heat. For the Hg lamp, $\phi = 1.7 \pm 1.2$, with a large enough uncertainty that the best one can say is that the quantum yield is of order unity.

As k_1 represents the rate of formation of C_2H_2, and k is the total photodestruction rate of C_2H_4, the ratio k_1/k gives the branching ratio for $C_2H_4 \rightarrow C_2H_2$. For photolysis by the H_2 lamp, this ratio is 0.44 ± 0.26, so that as a best estimate, only half of the lost ethylene can be accounted for by the corresponding increase in C_2H_2. For photolysis by the mercury lamp, the ratio is even smaller: 0.32 ± 0.26. The fact that the branching ratio is smaller at longer wavelengths is similar to the trend for gas phase photolysis discussed in Section 2.2, so the decrease may again be due to the formation of vinyl radicals at longer wavelengths. But as C_2H_3 or any carbon containing species other than C_2H_2 is not seen, a major question still remains: what is the form of the missing products, and why are they not seen in either the mass spectroscopic or IR spectroscopic analyses? It is possible that the distribution of product species other than C_2H_2 and H_2 is broad enough that any individual species is below the limit of detection for both the mass spectroscopic and infrared scans. Longer irradiation exposures in future experiments may help clarify this discrepancy.

It is unlikely that significant amounts of C_2H_3 are produced and stored in the matrix. *Ab initio* calculations of the dipole moment derivatives of C-H vibrational modes near 3100 cm^{-1} indicate they are roughly a third the size of the moment derivatives producing the observed ν_3 band of C_2H_2 (Dupuis and Wendoloski 1984). If the vinyl radical were a primary, stable product of C_2H_4 photolysis, absorption features of such strength would be seen.

An alternative possibility for the missing products is that the molecular weight of such products is higher than 70, the limit of the mass spectrometer scans. This is quite possible, as the photolysis of many ices eventually produce polymeric residues. The infrared bands of such polymers may be very wide, so that discerning them from the spectral baseline would

be difficult. Such refractory residues, or tholins, have been the subject of research both in the context of the interstellar medium (e.g., Hagen *et al.* 1979) and the outer solar system (e.g., Thompson *et al.* 1987). These residues are usually visibly colored, and have been suggested as the cause for coloration on the surfaces of outer solar system bodies. Acetylene is specifically known to polymerize upon photolysis (Zelikoff and Aschenbrand 1956), so this may in fact be the end product of the ethylene photolysis. However, as mentioned previously, we observed no coloration in our ice samples, so the ultimate fate of ethylene photolysis remains speculative.

The values determined for k_3, the destruction rate of C_2H_2, are the least certain in this analysis. Most of the data trends could be reasonably fit without any appreciable C_2H_2 destruction, but this is due to the fact that most experiments were short enough and samples thick enough that an appreciable percentage of the initial C_2H_4 was not photolyzed into C_2H_2, so that the destruction term for acetylene was not important for the duration of the photolysis. A notable exception is the experiment shown in Fig. 2.17, for a very thin sample subjected to a long exposure from the H_2 lamp. In this example, the trend for the C_2H_2 data could not be well fit without an appreciable C_2H_2 destruction rate, as the C_2H_2 growth is seen to flatten out. The inferred value of $k_3/I = 2.2 \times 10^{-18}$ cm^2 for this experiment is probably the most reasonable estimate for the C_2H_2 destruction rate. Taking the average gas phase cross section of C_2H_2 in the region from 1200 - 1700 Å as ~few x 10^{-18} cm^2, this would imply that the quantum yield for acetylene destruction ($k_3/I\sigma$) is of order unity. Again, further experiments quantifying the photolysis of solid state C_2H_2 are planned for the near future.

Taking the average values in Table 2.3 as the best parameters to fit the given data, these are put into the model to provide a simple picture of how a

sample of ethylene ice responds to photolysis, shown in Figure 2.19. As can be seen, the primary difference between photolysis with the H_2 and Hg lamps is in the depth scale. As the calculated cross section of solid state C_2H_4 at 1849 Å is smaller than that near 1600 Å, the UV photons penetrate further into the ice, and the energy absorbed per unit volume is smaller. The total destruction of C_2H_4 is roughly the same, but spread through a larger volume at longer wavelengths. The photochemical processing is rapid near the surface where the photons are not attenuated, but falls off quickly deeper into the ice.

Overall, the solid state kinetics for C_2H_4 photolysis are not substantially different from the corresponding gas phase kinetics. The primary difference appears to be in the branching ratio for C_2H_2 formation, and the lack of any other significant carbon containing species. More experimental work is definitely needed to provide a complete picture of the solid state chemistry of such photolysis.

2.6. Application to Triton's Surface

Given the quantitative values determined for the solid state photolysis of C_2H_4, the kinetics of ethylene ice photolysis on Triton's surface can be examined. As the results have shown that dilution in an N_2 matrix does not appreciably modify the C_2H_4 destruction rate, we need not establish if the C_2H_4 exists as a pure phase on the surface, or is in solid solution with the dominant N_2. The photochemical lifetime of surface ethylene can thus be calculated once the ambient UV radiation field on Triton's surface is known.

The dominant UV absorber in Triton's atmosphere for $\lambda < 1000$ Å is CH_4. However, the absorption cross section for methane drops sharply for $\lambda >$

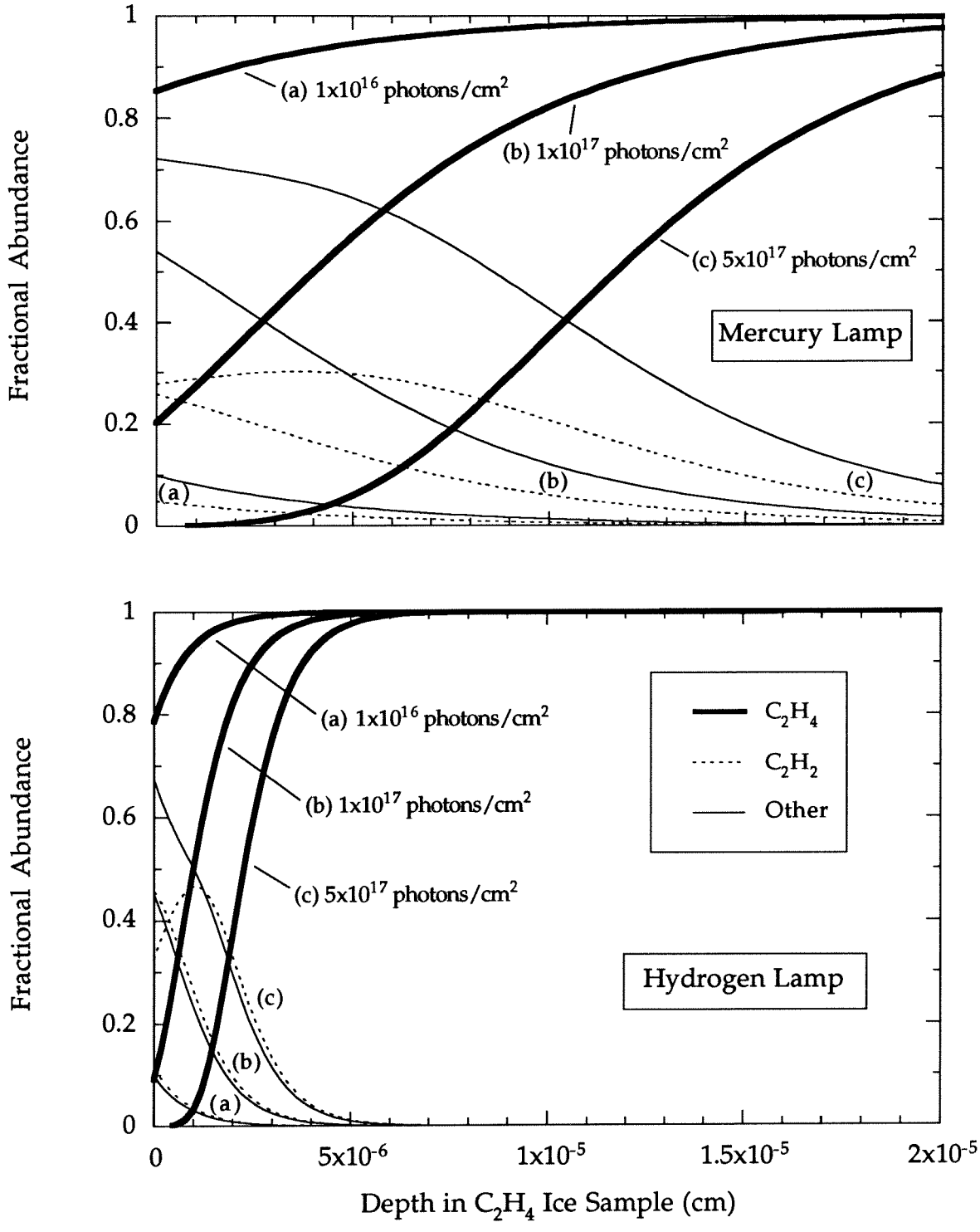

Figure 2.19. Results of the simple kinetic model for C_2H_4 and C_2H_2, showing how the abundances of these species change as a function of UV fluence and depth in an irradiated ice sample, for both the Hg and H_2 lamps. Also shown is the evolution of the photolysis products not seen in the experiments, but inferred from mass conservation.

1500 Å (Mount and Moos 1978), so the atmosphere is effectively transparent above this wavelength. The ambient mixing ratios of atmospheric photochemical products such as C_2H_4 and C_2H_2 are too small to provide any significant opacity (Lyons *et al.* 1994). This is true even for the haze layer, which has an estimated UV optical thickness of $\tau = 0.024$ (Herbert and Sandel 1991). As the results presented in this paper show that ethylene photodissociation in the solid state is robust even at $\lambda = 1849$ Å, a sizable window exists in Triton's atmosphere to allow processing of surface C_2H_4.

Figure 2.20 shows the estimated solar flux at Triton's surface as a function of wavelength. The solar spectrum (Mount and Rottman 1983) was adjusted for Triton's location at 30 AU. CH_4 provides the only opacity in this calculation, with a column density of 3×10^{17} molecules cm^{-2}, estimated from methane profiles given previously (Herbert and Sandel 1991; Lyons *et al.*, 1994). To show that the CH_4 abundance does not affect this value much, as the solar flux below 1850 Å is dominated by radiation longward of the CH_4 absorption threshold near 1500 Å, Table 2.4 gives the estimated integrated surface UV flux for $\lambda < 1850$ and 2000 Å, for different methane column densities. As a reasonable estimate, the total incident flux for wavelengths $\lambda < 1850$ Å is 2.6×10^9 photons cm^{-2} sec^{-1}. Radiation longward of 1850 Å may also produce photodissociation of C_2H_4 as it does in the gas phase (Balko *et al.* 1992), so this can be regarded as a lower limit to the incident UV flux. Given the estimated surface condensation rate of 1.7×10^8 molecules cm^{-2} sec^{-1} from Lyons *et al.* (1994), and using $\phi \sim 0.5$ as the quantum efficiency, the photochemical destruction rate is still roughly an order of magnitude greater than the calculated condensation rate. *The ambient solar UV flux incident on Triton's surface is thus more than sufficient to destroy all the C_2H_4 as it is deposited, so that building up a thick layer over time is not possible.*

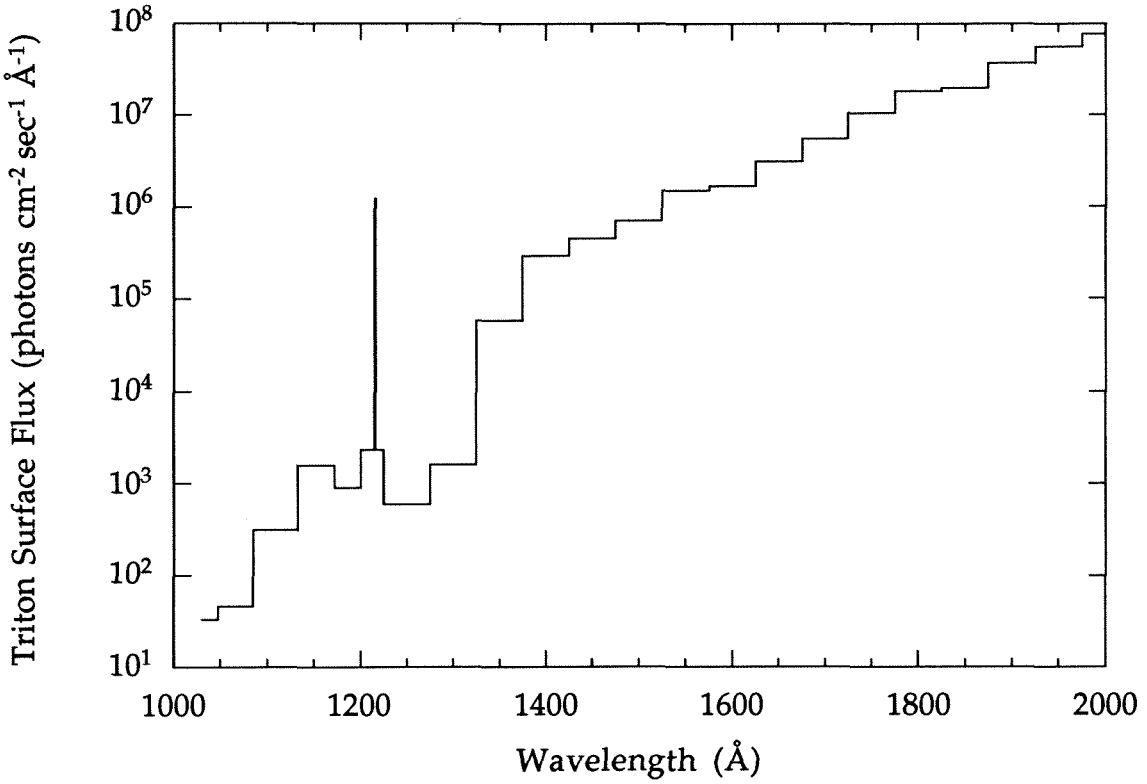

Figure 2.20. Calculated flux of solar UV radiation on Triton's surface. This assumes the only significant atmospheric absorber is CH_4 (estimated column density $3x10^{17}$ molecules/cm^2). The spike at 1216 Å is Lyman α.

Table 2.4. UV Flux at Triton's Surface for Different CH_4 Column Densities.

CH_4 Column Density (molec cm^{-2})	Total Surface Flux < 1850 Å (photons cm^{-2} sec^{-1})	Total Surface Flux < 2000 Å (photons cm^{-2} sec^{-1})
1.0E+15	3.5E+09	1.1E+10
1.0E+16	3.3E+09	1.1E+10
1.0E+17	2.7E+09	9.9E+09
1.0E+18	2.6E+09	9.7E+09
1.0E+19	2.6E+09	9.7E+09

Additional radiation due to energetic particle bombardment will only help in the destruction process. However, the UV radiation in the region from 1500 Å < λ < 1850 Å is the dominant energy source affecting Triton's immediate surface chemistry, that is, the composition in the top few microns that are observable with infrared instruments. The incident energy flux for cosmic rays is ~ 9 x 10^{-3} ergs cm^{-2} sec^{-1}, taken from a summary of energy sources in the atmosphere of Titan made by Sagan and Thompson (1984), assuming that the incident cosmic ray flux is the same for Titan and Triton and that Triton's atmosphere will provide negligible attenuation of this flux. The corresponding energy flux due to 1500 Å < λ <1850 Å photons is ~ 3 x 10^{-2} ergs cm^{-2} sec^{-1}, calculated from the spectrum shown in Fig. 2.20. However, as the absorption cross sections for cosmic rays are roughly 10^{-25} cm^2 (Capone *et al.* 1983), the penetration scale length is on the order of tens of centimeters. The difference in deposition energy *density* between UV photons and cosmic rays is therefore quite large, so that the uppermost surface composition that is inferred via spectroscopic observations is overwhelmingly controlled by the UV photochemistry.

It is interesting to note that as the estimated atmospheric condensation rate for C_2H_2 is an order of magnitude smaller than the corresponding rate for C_2H_4 (Lyons *et al.* 1994), the primary source of surface C_2H_2 will be production *in situ* by the photolysis of ethylene ice rather than the atmospheric condensation, greater by a factor of ~ 3 - 5 as determined from the branching ratio. However, as indicated in the previous discussion of the destruction rate for C_2H_2, the quantum yield for destruction of near unity would prevent the buildup of acetylene as well.

The production of trapped H_2 in the photolyzed ice is interesting with regard to the observed geyser-like activity on Triton's surface (Smith *et al.*

1989). The buildup over time of enough subsurface H_2 could eventually lead to explosive venting. However, given the fact that hydrocarbon species comprise a very small fraction of the surface ices, this process may not be adequate.

The primary question remaining with respect to the photolysis of C_2H_4 on Triton's surface is one raised previously: what is the photochemical evolution beyond and in addition to the formation of C_2H_2? It is tempting to suggest that the surface coloration is a direct result of the photolysis of hydrocarbons such as ethylene. However, a large quantitative gap remains in our understanding of the transition between the known surface chemistry and the observed surface coloration. The chemistry involved in this evolution is certainly quite complex. Hopefully more laboratory studies will attempt to address chemical mechanisms rather than just providing empirical fits, so that the complex chemistry of icy surfaces can eventually be unraveled.

2.7. Conclusions and Future Directions

We have shown experimentally that photolysis rates for C_2H_4 in the solid state are similar to those in the gas phase, and are not affected by dilution in an N_2 matrix. As the quantum yield for the photodestruction of C_2H_4 is of order unity, the ambient flux of solar UV radiation at Triton's surface is more than sufficient to photolyze the ethylene as it is condensing out from the atmosphere onto the surface, preventing the buildup of a layer of C_2H_4 over time. The primary products of this photolysis are C_2H_2 and H_2. The acetylene is photolyzed as well, and preliminary data suggest that the

ambient UV flux is again more than sufficient to destroy the C_2H_2 as it is being formed. The non-detection of these species on Triton is therefore not anomalous, but expected.

Further work is needed to quantify the full product yields of the photolysis of both C_2H_4 and C_2H_2 in the solid state. The results presented here only investigate the initial photochemical changes of one species; to fully understand the chemistry of the surface ices on Triton, the chemical evolution of each surface species, and their interrelations, must be explored. The ultimate goal of this type of research is to fully describe the photochemistry in the surface ice layer of outer solar system bodies as is done in the gas phase for planetary atmospheres. This will require a great deal of systematic, quantitative laboratory research on the irradiation effects of all major ice species in the solar system (e.g., H_2O, N_2, NH_3, CH_4, CO, HCN, etc.) with both UV and energetic particles, as called for by Thompson *et al.* (1987). Such information will generate substantial advances in our understanding of the evolution of chemical budgets of individual solar system bodies and the solar nebula in general.

References

Allamandola, L. J., S. A. Sandford, and G. J. Valero 1988. Photochemical and thermal evolution of interstellar/precometary ice analogs. *Icarus* **76**, 225.

Back, R. A., and D. W. L. Griffiths 1967. Flash photolysis of ethylene. *J. Chem. Phys.* **46**, 4839.

Balko, B. A., J. Zhang, and Y. T. Lee 1992. Photodissociation of ethylene at 193 nm. *J. Chem. Phys.* **97**, 935.

Capone, L. A., J. Dubach, S. S. Prasad, and R. C. Whitten 1983. Galactic cosmic rays and N_2 dissociation on Titan. *Icarus* **55**, 73.

Cruikshank, D. P., R. H. Brown, and R. N. Clark 1984. Nitrogen on Triton. *Icarus* **58**, 293.

Cruikshank, D. P., T. L. Rouch, T. C. Owen, T. R. Geballe, C. deBergh, B. Schmitt, R. H. Brown, and M. J. Bartholomew 1993. Ices on the surface of Triton. *Science* **261**, 742.

d'Hendecourt, L. B., L. J. Allamandola, F. Baas, and J. M. Greenberg 1982. Interstellar grain explosions: Molecule cycling between gas and dust. *Astron. Astrophys.* **109**, L12.

Dupuis, M., and J. J. Wendoloski 1984. Sytematic GVB study of harmonic vibrational frequencies and dipole moment derivatives; The vinyl radical C_2H_3 and other simple molecules. *J. Chem. Phys.* **80**, 5696.

Gordon, R., Jr., and P. Ausloos 1971. The solid phase photolysis and radiolysis of ethylene at 20 to 77 K. *J. Res. Natl. Bur. Std.* **75A**, 141.

Greenberg, J. M., C. X. Mendoza-Gomez, M. S. de Groot, and R. Breukers 1993. Laboratory dust studies and gas-grain chemistry. In *Dust and Chemistry in Astronomy* (T. J. Millar and D. A. Williams, Eds.), pp. 271-295. Bristol, Philadelphia.

Griffiths, P. R. and J. A. deHaseth 1986. *Fourier Transform Infrared Spectroscopy* (Wiley, New York).

Hagen, W., L. J. Allamandola, and J. M. Greenberg 1979. Interstellar molecule formation in grain mantles: The laboratory analog experiments, results, and implications. *Astrophys. Space Sci.* **65**, 215.

Hara, H., and I. Tanaka 1973. Photolysis of ethylene at 1634 Å and 1849 Å. *Bull. Chem. Soc. Japan.* **46**, 3012.

Herbert, F., and B. R. Sandel 1991. CH_4 and haze in Triton's lower atmosphere. *J. Geopys. Res.* **96**, 19241.

Hirokami, S., and R. J. Cvetanovic 1974. Photolysis of Liquid and Solid Ethylene at 184.9 nm. *J. Phys. Chem.* **78**, 1254.

Hudgins, D. M., S. A. Sandford, L. J. Allamandola, and A. G. G. M. Tielens 1993. Mid- and far-infrared spectroscopy of ices: Optical constants and integrated absorbances. *Ap. J. Suppl. Series* **86**, 713-870.

Jacox, M. E. 1962. Solid-state vibrational spectra of ethylene and ethylene-d_4. *J. Chem. Phys.* **36**, 140.

Khanna, R. K., M. J. Ospina, and G. Zhao 1988. Infrared band extinctions and complex refractive indices of crystalline C_2H_2 and C_4H_2. *Icarus* **73**, 527.

Kouchi, A., J. M. Greenberg, T. Yamamoto, and T. Mukai 1992. Extremely low thermal conductivity of amorphous ice: Relevance to comet evolution. *Astrophys. J.* **388**, L73.

Leger, A., M. Jura, and A. Omont 1985. Desorption from interstellar grains. *Astron. Astrophys.* **144**, 147.

Lyons, J.R., Y. L. Yung, and M. Allen 1994. Photochemistry of the atmosphere and ionosphere of Triton. Submitted to *Icarus*.

Moore, M. H., B. Donn, R. Khanna, and M. F. A'Hearn 1983. Studies of proton-irradiated cometary-type ice mixtures. *Icarus* **54**, 388.

Mordaunt, D. H., I. R. Lambert, G. P. Morley, M. N. R. Ashfold, R. N. Dixon, C. M. Western, L. Schnieder, and K. H. Welge 1993. Primary product channels in the photodissociation of methane at 121.6 nm. *J. Chem. Phys.* **98**, 2054.

Mount, G. H., and H. W. Moos 1978. Photoabsorption cross sections of methane and ethane, 1380 - 1600 Å, at T = 295 K and T = 200 K. *Astrophys. J.* **224**, L35.

Mount, G. H., and G. J. Rottman 1983. The solar absolute spectral irradiance 1150-3171 Å. *J. Geophys. Res.* **88**, 5403.

Okabe, H. 1983. Photochemistry of acetylene. *Can J. Chem.* **61**, 850.

Okabe, H., and J.R. McNesby 1962. Vacuum ultraviolet photochemistry. II. Photolysis of ethylene. *J. Chem. Phys.* **36**, 601.

Owen, T. C., T. L. Rouch, D. P. Cruikshank, J. L. Elliot, L. A. Young, C. deBergh, B. Schmitt, T. R. Geballe, R. H. Brown, and M. J. Bartholomew 1993. Surface ices and atmospheric composition of Pluto. *Science* **261**, 745.

Pirronello, V. 1993. Irradiation of molecular ices. In *Dust and Chemistry in Astronomy* (T. J. Millar and D. A. Williams, Eds.), pp. 297-329. Bristol, Philadelphia.

Prinn, R. G., and B. Fegley, Jr., 1989. Solar nebula chemistry: Origin of planetary, satellite, and cometary volatiles. In *Origin and Evolution of Planetary and Satellite Atmospheres* (S. K. Atreya, J. B. Pollack, and M. S. Matthews, Eds.), pp. 78-136. Univ. of Arizona Press, Tucson.

Rytter, E., and D. M. Gruen 1979. Infrared spectra of matrix isolated and solid ethylene. Formation of ethylene dimers. *Spectrochim. Acta* **35A**, 199.

Sagan, C., and W. R. Thompson 1984. Production and condensation of organic gases in the atmosphere of Titan. *Icarus* **59**, 133.

Sauer, M. C., Jr., and L. M. Dorfman 1961. Molecular detachment processes in the vacuum UV photolysis of gaseous hydrocarbons. I. Ethylene. II. Butane. *J. Chem. Phys.* **35**, 497.

Smith, B. A., L. A. Soderblom, and D. Banfield *et al.* 1989. Voyager 2 at Neptune: Imaging science results. *Science* **246**, 1422.

Strobel, D. F., M. E. Summers, F. Herbert, and B. R. Sandel 1990. The photochemistry of methane in the atmosphere of Triton. *Geophys. Res. Lett.* **17**, 1729.

Thompson, W. R., B. G. J. P. T. Murray, B. N. Khare, and C. Sagan 1987. Coloration and darkening of methane clathrate and other ices by charged particle irradiation: Applications to the outer solar system. *J. Geophys. Res.* **92**, 14933.

Thompson, W. R., and C. Sagan 1990. Color and chemistry on Triton. *Science* **250**, 415.

Trafton, L. 1984. Large seasonal variations in Triton's atmosphere. *Icarus* **58**, 312.

Tryka, K.A., R. H. Brown, V. Anicich, D. P. Cruikshank, and T. C. Owen 1993. Spectroscopic determination of the phase composition and temperature of nitrogen ice on Triton. *Science* **261**, 751.

Tschuikow-Roux, E., J. R. McNesby, W. M. Jackson, and J. L. Faris 1967. Reactions of ethylidene in the vacuum ultraviolet photolysis of ethylene. *J. Phys. Chem.* **71**, 1531.

Wu, C. Y. R., T. S. Chien, G. S. Liu, D. J. Judge, and J. J. Caldwell 1989. Photoabsorption and direct dissociation cross sections of C_2H_2 in the 1530 - 1930 Å region: A temperature dependent study. *J. Chem. Phys.* **91**, 272.

Zelikoff, M., and L. M. Aschenbrand 1956. Vacuum ultraviolet chemistry. III. Acetylene at 1849 Å. *J. Chem. Phys.* **24**, 1034.

Zelikoff, M., and K. Watanabe 1953. Absorption coefficients of ethylene in the vacuum ultraviolet. *J. Opt. Soc. Am.* **43**, 756.

Zhao, G., M. J. Ospina, and R. K. Khanna 1988. Infrared intensities and optical constants of crystalline C_2H_4 and C_2D_4. *Spectrochem. Acta* **44A**, 27.

Appendix A - Determination of Ice Film Thickness

The thickness of a vapor-deposited ice sample in the laboratory must be accurately measured to constrain the column density of a given species in the ice. Two procedures are commonly used to monitor the thickness of a deposited ice sample. The first method relies on modeling the baseline of the transmittance spectrum of the ice sample once the deposition is complete. As seen in Figure A.1, the baseline of the spectrum shows a sinusoidal variation, with the frequency of the oscillation proportional to the ice thickness. This baseline variation is labeled as "channel fringes" by Khanna and co-workers

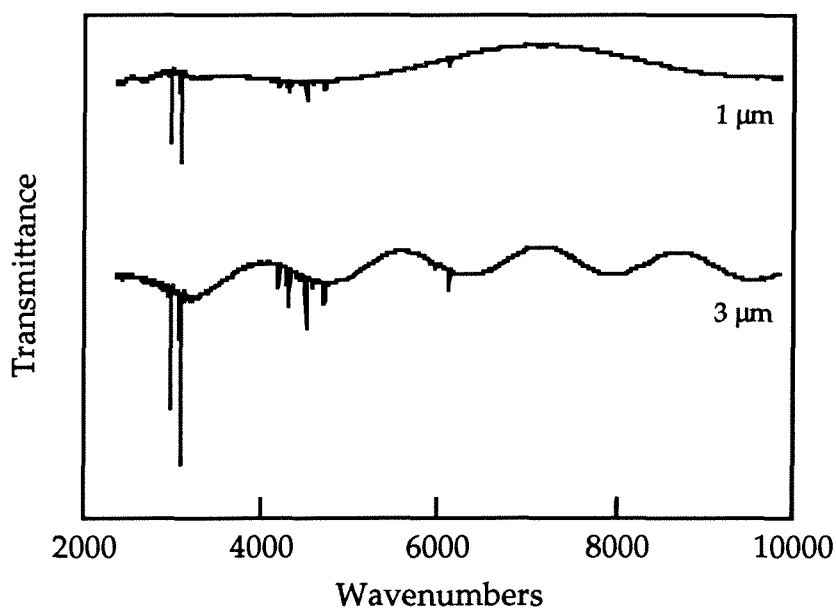

Figure A.1. Transmittance spectra of C_2H_4 ice for two film thicknesses of 1 μm and 3 μm. Note the difference in the frequency of the "channel fringes" in the spectral baseline between the two samples.

in their work measuring the infrared optical constants for various ices (e.g., Zhao, Ospina, and Khanna 1988; Khanna, Ospina, and Zhao 1988). This modeling method is more fully described in these references.

The second, more common, technique is to monitor the growth of the ice film directly by measuring the changing intensity of light reflected from the growing film. This is the method employed here. As the ice grows, the reflected intensity from a monochromatic source, such as a HeNe laser, exhibits interference fringes due to the superposition of reflections from the vacuum-ice interface and the ice-substrate interface. This method was discussed first by Heavens (1965), and has been used by many researchers (e.g., Sill, Fink, and Ferraro 1980; Wood and Roux 1982; Allamandola, Sandford, and Valero 1988). The following is a description of how the ice thickness is derived from the observed interference in the reflected intensity.

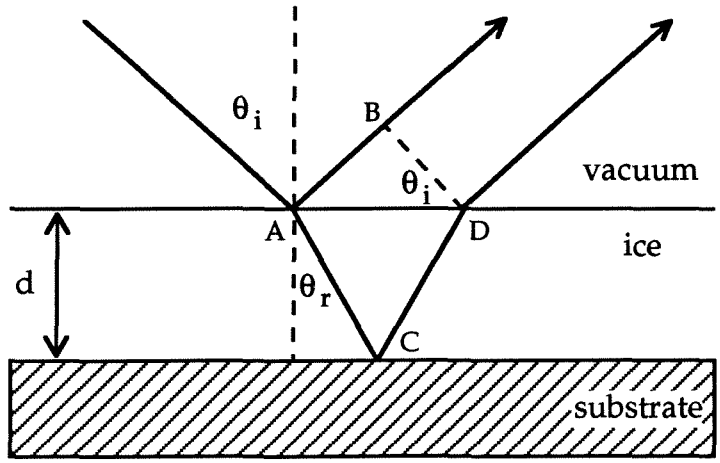

Figure A.2. Ray tracing of the reflectance from a thin film.

To illustrate the basic problem, Figure A.2 depicts a uniform film of thickness d and refractive index n deposited on a substrate. The path

difference between the ray reflected from the vacuum-ice interface and the ray reflected from the substrate-ice interface is given by

$$n(\overline{ACD}) - \overline{AB}. \tag{1}$$

When this difference is equal to $m\lambda$, where m is an integer and λ is the wavelength of the incident radiation (.6328 μm for a HeNe laser), the reflected wavefront interferes constructively and is a maximum. Alternatively, when

$$n(\overline{ACD}) - \overline{AB} = \left(m + \frac{1}{2}\right)\lambda, \tag{2}$$

the reflected wavefronts interfere destructively and give a minimum in the reflected intensity. Thus as the deposited film grows, the reflected intensity shows a sinusoidal pattern with a frequency proportional to the deposition rate.

The number of fringes that are observed in the reflected intensity can easily be related to the film thickness. From Fig. A.2, Snell's law gives

$$n\sin\theta_r = \sin\theta_i = \frac{\overline{AB}}{\overline{AD}}, \tag{3}$$

so that

$$\overline{AB} = \overline{AD}\, n\sin\theta_r.$$

In addition, as

$$\overline{AD} = 2d\tan\theta_r,$$

the path that reflects from the vacuum-ice interface can be expressed as:

$$\overline{AB} = \frac{2nd\sin^2\theta_r}{\cos\theta_r}. \tag{4}$$

Similarly, the path that passes through the ice sample can be expressed as:

$$n(\overline{ACD}) = \frac{2nd}{\cos\theta_r}. \tag{5}$$

Substitution of equations (4) and (5) into eqn. (1) then gives, in terms of the measurable quantity θ_i,

$$m\lambda = 2d\left[n^2 - \sin^2\theta_i\right]^{1/2}. \tag{6}$$

Thus for the simple geometry shown in Fig. A.2, the thickness of a deposited sample is determined by m, the number of interference fringes in the reflected intensity during deposition. This assumes that n, the refractive index of the ice, is known at 0.6328 μm. For the films of C_2H_4 and C_2H_2 used in the experiments of Chapter 2, it was assumed that n = 1.4 in the visible, as reported previously (Zhao, Ospina, and Khanna 1988; Khanna, Ospina, and Zhao 1988). For N_2 ice, a value of n = 1.2 was assumed, the value for n at the wavelength of the sodium D lines (Hallam and Scrimshaw 1973). For the H_2O films of chapter 1, n = 1.3 was used, as reported by Hudgins *et al.* (1993). (Other similar techniques are used that simultaneously determine both the thickness of a film and the refractive index at the laser wavelength. This is usually accomplished by concurrently monitoring the reflectance of two separate laser beams of the same wavelength but different incidence angles on the ice surface. Alternatively, two beams of different wavelengths but the

same incidence angle will give both d and n. An extensive list of references using these techniques is listed in Goodman (1978), in a paper that describes an approximate method to measure both d and n from the reflected or transmitted intensity of only one beam.)

The simple technique described above in reference to eqn. (6) has some complications in actual practice. In the Extraterrestrial Ice Simulator (EIS) at JPL, which was used for these experiments, the substrate for the ice deposition is a sapphire window exposed on both sides to the vacuum chamber, as

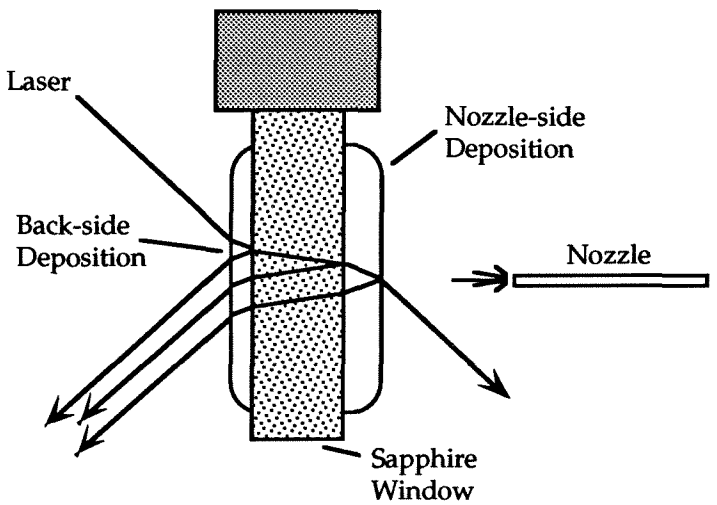

Figure A.3. Schematic of the deposition and laser geometry in the EIS. The thickness of the window and the deposition have been exaggerated.

shown in the schematic of Figure A.3. The deposition is directed toward only one side of the window by an inlet nozzle set ~4 cm away, but the deposition of ices that have low sticking coefficients or substantial vapor pressures at the temperature of the window cause the ambient pressure in the chamber to rise, allowing some deposition on the back side of the window. In addition, the distribution of gas flowing from the pinhole nozzle is wider than the

window dimension of 2 cm, so in selected experiments, a copper shield was added to frame the window edges to widen the effective cooled substrate area and thus minimize the background pressure during deposition.

The relation between the order of the interference fringes and the film thickness shown in eqn. (6) holds for thin film growth on either side of the window with respect to the incident laser beam. One would then expect depositions on both sides of the window to contribute to the laser reflectance,

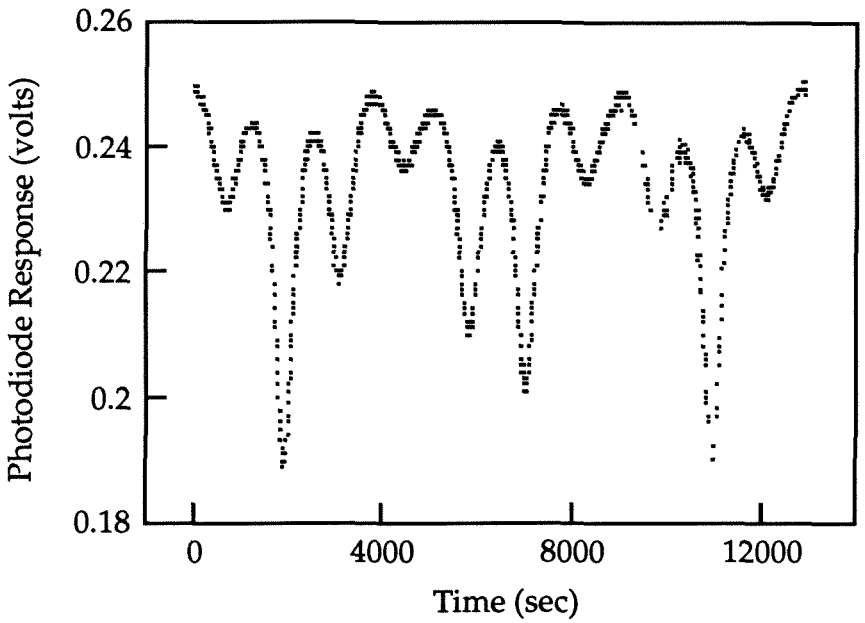

Figure A.4. Reflected intensity of a HeNe laser during the deposition of N_2 ice at 17K.

in a beat pattern due to the different deposition rates on both sides. This is in fact what is observed, as seen in Figure A.4, showing the reflected intensity as measured by a photodiode during a deposition of N_2. Two frequencies can clearly be distinguished: a high frequency component due to deposition directly from the nozzle, and a lower frequency component due to deposition on the back-side of the window. Unfortunately, the reflected intensity shown

in Fig. A.4 cannot be fit by the simple addition of two sine waves of different frequency and amplitude. This is because the amplitude of the reflected intensity from the growing film on the nozzle-side of the window is coupled to the transmitted intensity from the film on the back-side, as seen in Fig. A.3. The *frequencies* of the fringing on either side of the window are independent, however, as they depend only on the absolute deposition rates. As the fringe frequencies, and thus the absolute rates for the depositions on both sides can easily be discerned, this qualitative explanation is adequate to give the desired film thickness.

An additional point of concern experimentally is that the ice may not be of uniform thickness within the spectrometer beam. In an attempt to minimize this problem, the beam of the FTIR was stopped down to a diameter of ~0.7 cm on the ice sample. To test how uniform the ice samples

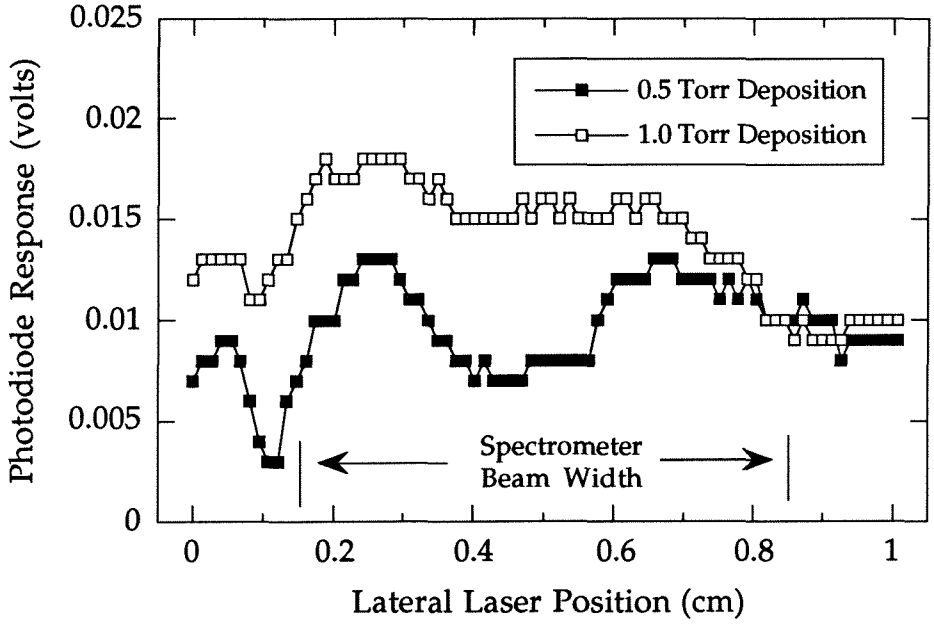

Figure A.5. Sweeps of the HeNe laser over N_2 ice samples, deposited at different nozzle backing pressures.

were within the spectrometer beam, the laser was put on a translation stage that allowed the laser beam to be swept across the sample. If the sample were uniform, then sweeping the laser should show no variation in the reflected intensity. If, however, the thickness varied on the order of a laser wavelength over the laser sweep, then interference fringes would be seen. Figure A.5 shows such laser sweeps for several different depositions of N_2. The laser was first swept over the bare substrate, and then swept over the N_2 deposition. The difference gives the profile of the ice deposition. As can be seen in Fig. A.5, the variation in the reflected intensity within the beam area is <0.01 volt as measured by the photodiode, while the peak-to-peak variation due to a fringe in the N_2 deposition shown in Fig. A.4 is ≥0.05 volts. The maximum possible thickness variation within the spectrometer beam area was therefore ~20%. Additionally, the variation does not appear to strongly depend on either deposition rate or sample thickness, at least within the range of deposition conditions used in these experiments.

References

Allamandola, L. J., S. A. Sandford, and G. J. Valero, 1988. Photochemical and thermal evolution of interstellar/precometary ice analogs. *Icarus* **76**, 225.

Goodman, A. M., 1978. Optical interference method for the approximate determination of refractive index and thickness of a transparent layer. *App. Optics* **17**, 2779.

Hallam, H. E., and G. F. Scrimshaw, 1973. *Vibrational Spectroscopy of Trapped Species*, ed. H. E. Hallam (Wiley, New York).

Heavens, O. S., 1965. *Optical Properties of Thin Solid Films* (Dover, New York).

Hudgins, D. M., S. A. Sandford, L. J. Allamandola, and A. G. G. M. Tielens, 1993. Mid- and far infrared spectroscopy of ices: optical constants and integrated absorbances. *Ap. J. Suppl. Series* **86**, 713.

Khanna, R. K., M. J. Ospina, and G. Zhao, 1988. Infrared band extinctions and complex refractive indices of crystalline C_2H_2 and C_4H_2. *Icarus* **73**, 527.

Sill, G., U. Fink, and J. R. Ferraro, 1980. Absorption coefficients of solid NH_3 from 50 to 7000 cm^{-1}. *J. Opt. Soc. Am.* **70**, 724.

Wood, B. E., and J. A. Roux, 1982. Infrared optical properties of thin H_2O, NH_3, and CO_2 cryofilms. *J. Opt. Soc. Am.* **72**, 720.

Zhao, G., M. Ospina, and R. K. Khanna, 1988. Infrared intensities and optical constants of crystalline C_2H_4 and C_2D_4. *Spectrochem. Acta* **44A**, 27.

Appendix B - UV Source Characterization

To properly evaluate the quantum yields and absolute reaction rates in the ethylene photolysis experiments, the output of the UV sources needed to be well characterized. Two low-pressure, microwave-discharge emission sources were utilized in the experiments: 1) a mercury lamp (Opthos, Inc.) sealed in a Suprasil quartz tube with a MgF_2 window, having narrow UV emission features at 1849 Å and 2537 Å, and 2) a homemade flowing hydrogen lamp, operated at 1 torr with a mixture of 10% H_2 and 90% He, having a narrow emission at Lyman α (1216 Å) and more extended emission

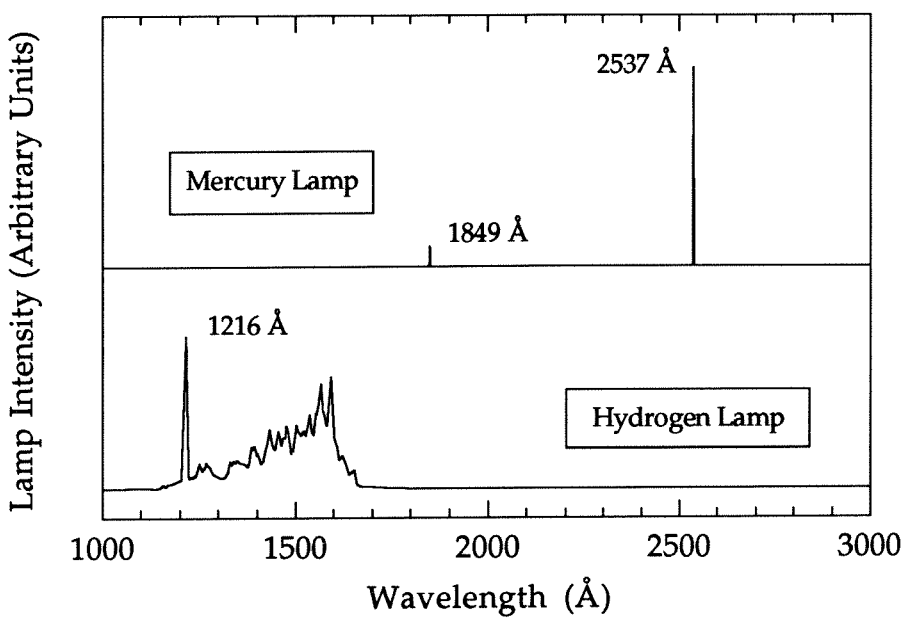

Figure B.1. Grating monochrometer scans of both UV sources (uncalibrated). This is valid only for line positions, and *not* relative strengths.

from the H_2 molecular lines centered near 1600 Å. The H_2/He mixture has been shown (Koller 1965) to provide a good source of Ly α, as the excited He buffer gas collisionally dissociates the H_2 into the separate hydrogen atoms necessary for Ly α emission. The qualitative spectra of these lamps in the region from 1000 - 3000 Å are shown in Figure B.1, taken on a vacuum UV grating monochrometer with the same silicon photodiode detector (IRD, model XUV-100) used to directly monitor the lamp flux on the ice samples, as discussed in the experimental section.

Simply measuring the current from the silicon photodiode in the EIS vacuum chamber when directly illuminated is unfortunately not adequate to characterize the UV output of the lamps. The discharge lamps have substantial emission longward of the wavelength threshold to produce photochemical changes in the ice samples, and the photodiode is sensitive to this emission as well. The task was thus to characterize the full spectrum of both lamps, and use only the flux from the photochemically important region of the output for the quantum yield calculations. As discussed in the results section, only the 1849 Å line from the Hg lamp is responsible for photochemistry, while the full region from 1216 ~ 1700 Å shown in Fig. B.1 from the hydrogen lamp is responsible for photochemical modification in the ice samples.

The monochrometer used to produce the spectra in Fig. B.1 is not sufficient for the full spectral characterization, as it does not operate longward of 3000 Å, and is additionally not calibrated in its operational region. Instead, a set of three long pass filters was used to measure the differential flux in different wavelength regions. The transmittance of these filters is shown in Fig. B.2, as provided by the manufacturers (Acton Research Corp., 1500 Å;

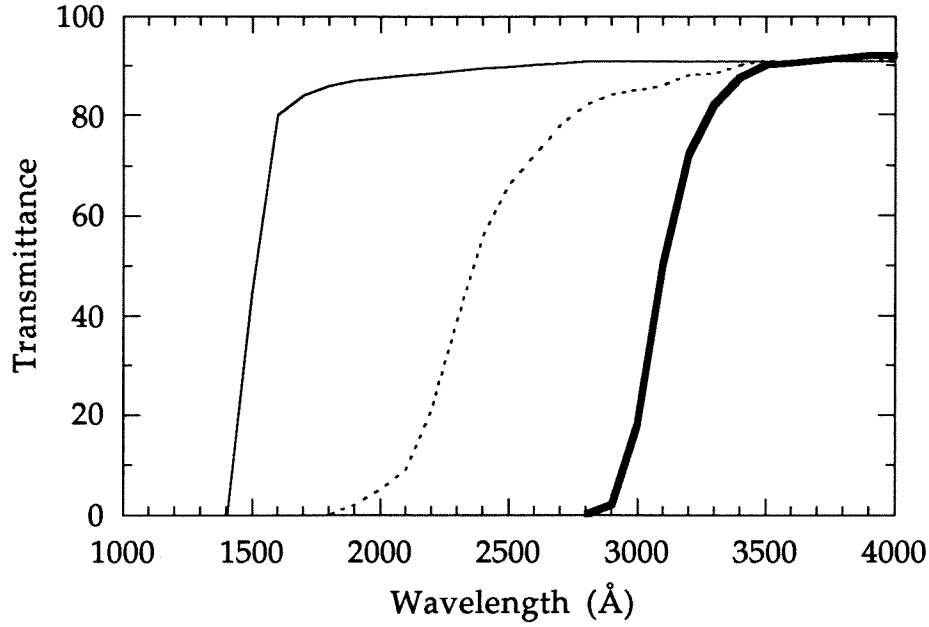

Figure B.2. Transmittance profiles of the three long-pass filters used for lamp calibrations, as specified by the manufacturers (Acton for 1500 Å and Oriel for others).

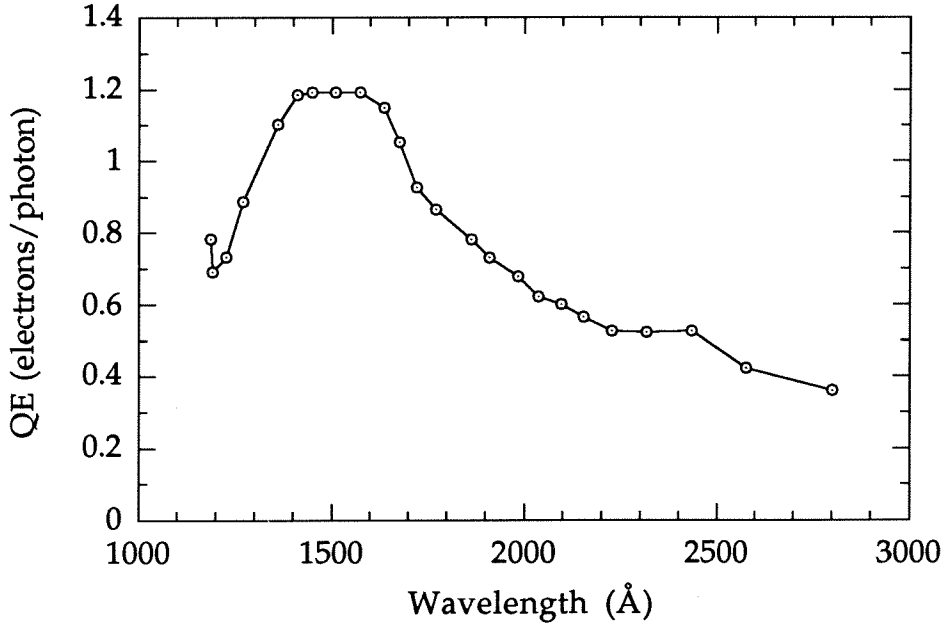

Figure B.3. Photodiode quantum efficiency as specified by manufacturer (IRD).

Oriel Corp., 2400 and 3100 Å). It was hoped that the 1500 Å filter would be adequate to measure the relative intensity between the Ly α and molecular emission from the hydrogen lamp, while the longer filters would separate out the photochemically important UV flux from the remainder of the output. Folded into these measurements is the photodiode response curve, provided by IRD and estimated to have an accuracy to within 20% at all wavelengths, shown in Fig. B.3. The quantum efficiency of the detector is on the order unity at the relevant UV wavelengths of these experiments, and it is 1 cm^2 in area.

The reported accuracy of the filters and silicon photodiode was tested with a calibrated source: a deuterium lamp traceable to a NIST standard source (Optronic Laboratories, Inc., model UV-40). The calibrated spectral irradiance from the lamp was reported from 2000 - 4000 Å, for operation 30 cm from a detector through one atmosphere. Measuring the throughput in this configuration with each filter showed that the silicon photodiode and filters operated as advertised, assuming a reasonable output from the deuterium lamp both longward and short of the calibrated window from 2000 - 4000 Å.

When using the hydrogen lamp, the measured photodiode current was $(3.6 \pm 0.2) \times 10^{-5}$ amps, nearly constant and quite repeatable for each experiment. The measured current dropped to 2.6×10^{-5} amps when blocked with the 3100 Å filter. Noting from the measured spectrum in Fig. B.1 that there is no substantial emission in the region between ~1700 Å and the filter onset at ~3100 Å, the total UV flux is found from the following:

$$\text{Bare Current} = (\text{QE*Flux})_{\lambda<1700\text{Å}} + (\text{QE*Flux})_{\lambda>3000\text{Å}} \quad (1)$$

$$3100\text{Å Filter Current} = (0.92)*(\text{QE*Flux})_{\lambda>3000\text{Å}}, \quad (2)$$

where QE is the quantum efficiency of the detector. Subtracting eqn. (1) from (2), and assuming QE = 1 for λ <1700Å, gives the UV flux:

$$(\text{Flux})_{\lambda<1700\text{Å}} = (6.3 \times 10^{18}\ \text{eV/C})^{*}\left[\left(3.6 \times 10^{-5}\right) - \left(\frac{2.6 \times 10^{-5}}{0.92}\right)\right]$$

$$= 4.9 \times 10^{13}\ [\text{photons/cm}^2\text{*sec}]. \qquad (3)$$

As the ice sample was about 50% further from the UV source than the photodiode, the UV flux on the ice sample was

$$(2/3)^2 * 4.9 \times 10^{13} = 2.2 \times 10^{13}\ [\text{photons/cm}^2\text{*sec}]. \qquad (4)$$

This is the total UV flux from the hydrogen lamp on the ice sample, and is uncertain by less than 20%. Distinguishing the Ly α flux from the H_2 emission by using the 1500 Å filter was ineffective, as the uncertainty in the subtraction technique outlined above was larger than the measured difference. From Fig. B.1, though, it is apparent that the molecular emission is by far the dominant UV component.

Determining the 1849 Å flux from the mercury lamp proved to be more difficult. The total output from the Hg lamp varied by over 50% as the discharge wattage drifted. The lamp was calibrated using both the 2400 and 3100 Å filters and by varying the wattage. Utilizing a set of equations analogous to (1) and (2), and separating the output regions into 1849 Å, 2537 Å, and visible emission, the relative flux from each of these regions was calculated as a function of lamp wattage, shown in Figure B.4. The 1849 Å line is responsible for roughly 3% of the total output of the lamp, for the usual discharge power of 26 - 32 Watts, although it does vary somewhat with total power. Again, this subtraction technique is poor when the difference

between the fluxes of two different filters is small compared to the overall flux, so the uncertainty in this figure is quite large (~50%).

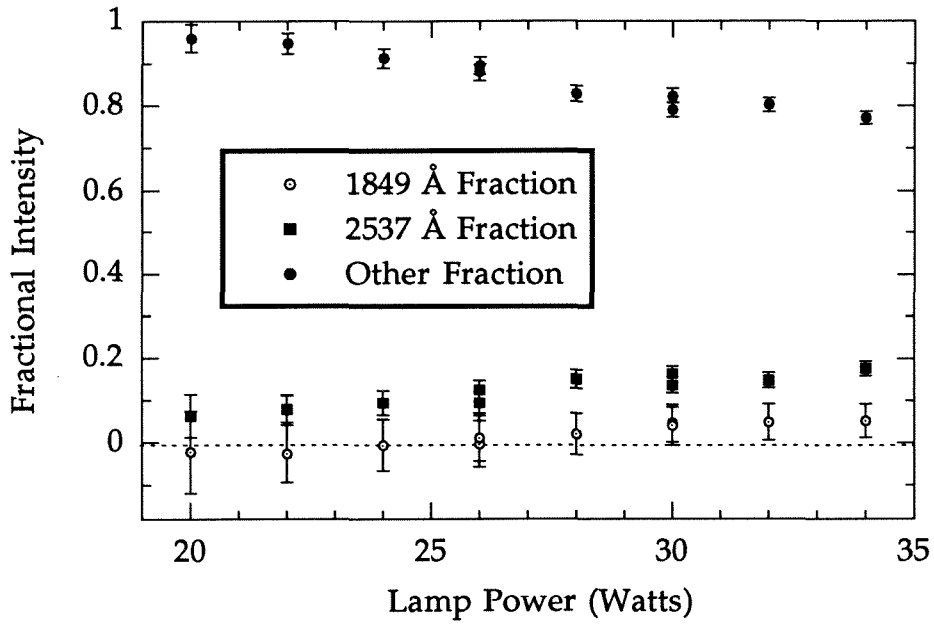

Figure B.4. Relative output of emission lines in mercury lamp as a function of discharge wattage.

Taking the relative output of the 1849 Å line to be 3%, the absolute flux on the ice samples from this line can be determined from the photodiode current. As mentioned in the experimental section, this current is continually monitored, so that fluence determinations are not based on the assumption that the absolute flux is constant. However, it was assumed that the *relative* flux of the 1849 Å line is constant, which is roughly true during each experiment. The conversion from measured current to a flux is then, assuming a QE for the photodiode of ~0.8 at 1849 Å,

$$(0.03) * (6.3 \times 10^{18}\ \text{eV/C}) * (1.25\ \text{photons/eV*cm}^2) = 2.4 \times 10^{17}\ [\text{photons/cm}^2\text{*C}]. \quad (5)$$

For this calibration, the detector was set 80% of the distance to the ice sample, so the conversion factor for the 1849 Å photolysis is

$$(0.8)^2 * 2.4 \times 10^{17} = 1.5 \times 10^{17} \text{ [photons/cm}^2\text{*C]}. \quad (6)$$

As the total photodiode current with the Hg lamp was typically in the range of 5×10^{-5} amps, the typical flux on the ice for 1849 Å was 7.5×10^{12} [photons/cm^2*sec], again, uncertain by roughly 50%.

A better way to monitor the intensity of a narrow feature like the 1849 Å line is the use of a narrow band pass filter that only transmits radiation of this wavelength. We plan to use such a filter in the near future to unambiguously monitor the flux variations in the 1849 Å line during ethylene photolysis, to constrain the chemistry as a function of fluence with greater precision.

Reference

Koller, L. R., 1965. *Ultraviolet Radiation*, (Wiley, NewYork), 86.

Chapter 3. Measurements of the Solid-State Greenhouse Effect in Glass Beads

Abstract

We show that a solid-state greenhouse, characterized by subsurface temperatures greater than the surface temperature in steady-state, can readily be produced in a bed of evacuated glass beads. Measurements of the thermal and radiative properties that govern the size of this subsurface temperature enhancement confirm that it can be reasonably predicted from these parameters.

3.1. Introduction

Thermal models of planetary surfaces generally assume that the absorption of incident insolation takes place only at the immediate surface. However, radiation at visible wavelengths incident on the surface of a translucent or high-albedo medium may be scattered to and absorbed at significant depths. If the subsurface absorption of visible radiation occurs in a medium that is opaque in the thermal infrared, then radiative cooling to space is only possible from the uppermost surface. The imbalance between the rapid rate of energy deposition at depth and the slower rate of cooling,

controlled by diffusive conduction of heat back to the surface, leads to an enhancement of subsurface temperatures over the mean surface temperature known as the solid-state greenhouse effect. This condition may be applicable to snowy or icy surfaces on earth (Schlatter 1972; Brandt and Warren 1993), or the surface of an icy satellite (Brown and Matson 1987; Matson and Brown 1989; Fanale *et al.* 1990).

The steady-state magnitude of the subsurface temperature enhancement, defined to be the difference in temperature between the average surface temperature and the hypothetical temperature at an infinite depth in the sunlit medium, was shown by Matson and Brown (1989) to be

$$\overline{\Delta T} = \overline{S'(t)}\frac{\zeta}{k}, \tag{1}$$

where $\overline{S'(t)}$ is the total absorbed insolation averaged over a diurnal cycle, ζ is the absorption scale length, defined as the depth at which 1/e of the bolometric absorption has occurred, and k is the thermal conductivity of the medium. Using values of k = 1000 ergs cm^{-1} sec^{-1} K^{-1} and ζ = 5 cm, Fanale *et al.* (1990) estimated that the magnitude of the subsurface temperature enhancement on an icy satellite such as Europa could be on the order of 35 K. Such an enhancement would alter the surface temperature boundary condition for global geophysical models, resulting in subsurface melting closer to the surface than predicted by traditional models that assume insolation is absorbed only at the immediate surface.

In this paper we verify experimentally that a subsurface, steady-state temperature enhancement can be established in a bed of evacuated glass beads, used as an analog for a planetary surface. In addition, we show that the magnitude of the subsurface temperature enhancement is of the same order

as that predicted by equation (1), by directly measuring the bead sample's bulk thermal conductivity, absorption scale length, and the incident visible flux.

3.2. Experiments at Atmospheric Pressure

As a trial run to test the feasibility of verifying and ultimately quantifying the solid-state greenhouse in the laboratory, the first set of experiments was purposefully kept simple and performed at atmospheric pressure. Air in pore spaces between the beads raises the thermal conductivity of the sample, so that the magnitude of the temperature inversion is much less than that in an evacuated sample. These experiments were designed only to show the qualitative difference in the temperature profiles between surfaces that absorb the bulk of the incident radiant energy at the surface versus at depth.

3.2.1. Experimental Setup at Atmospheric Pressure

To briefly outline the experimental setup, a bed of glass beads was poured into an insulating container, with thermocouples sandwiched at known depths in the bead bed. The surface of the bed was then irradiated with either floodlights that provided predominantly visible radiation that could penetrate through the transparent beads, or with a hot plate set directly on the bead surface to provide a strong infrared source that was absorbed at the immediate surface. A schematic for these experiments is shown in Fig. 3.1. The glass beads were purchased from Potters Industries, Inc., and were standard soda-lime glass (roughly 75% SiO_2, 15% Na_2O, and 10% CaO). The beads had a size range of 600 - 850 μm, were very nearly spherical, and were

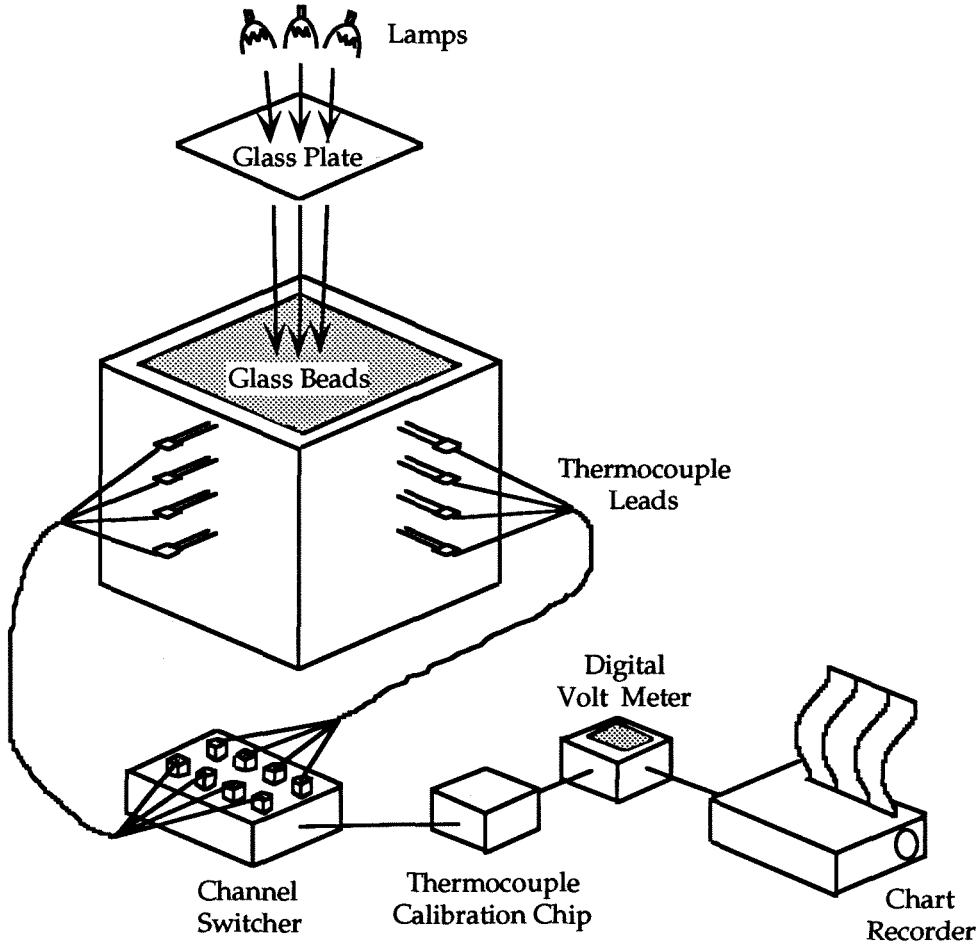

Figure 3.1. Schematic for the experiments at atmospheric pressure.

quite clear to visible light, with only ~ 1 in 100 beads having noticeable dark impurities, confirmed by microscopic inspection. For these experiments, the beads were used as bought, with no additional cleaning. The beads were poured a layer at a time into a Styrofoam insulating container 1 ft^3 in dimension. Copper constantan thermocouples were carefully positioned between each bead layer, vertically spaced ~ 1 cm apart in the center of the bead bed. The thermocouples were all run through a channel switcher that would take a new temperature reading every second. The raw thermocouple

junction voltages were converted to temperature using a calibration chip (Omega TAC) and the analog output temperature recorded.

The lamps used as the visible radiation source were three 50 Watt tungsten-halogen photofloods (Sylvania MR-16), each with a parabolic reflector coated to selectively focus the visible radiation, but not the thermal infrared, onto the bead surface. To minimize the infrared radiation on the beads even further (for the visible radiation experiments), a fan-cooled glass plate was placed between the lamps and the bead surface. The lamps provided roughly uniform intensity over about a 10 cm diameter on the bead surface.

3.2.2. Results at Atmospheric Pressure

Figure 3.2 (a) shows the thermal profiles with the infrared source incident on the bead surface. As the beads are opaque in the thermal infrared, all of the radiation is absorbed at the surface, so the heat transfer at all depths is purely conductive, the traditional picture for thermal models of planetary surfaces. As the hot plate providing the radiation has a constant power output, the infrared surface flux is also constant. The experimental thermal profiles can therefore be modeled by the heat equation for an infinite half-space, initially isothermal, with a constant surface flux as the upper boundary condition. This is a well-studied problem (Carslaw and Jaeger 1959), with solutions of the form given below:

$$T(z,t) = \frac{2F_o}{k}\sqrt{\kappa t}\ \mathrm{ierfc}\left(\frac{z}{2\sqrt{\kappa t}}\right), \qquad (2)$$

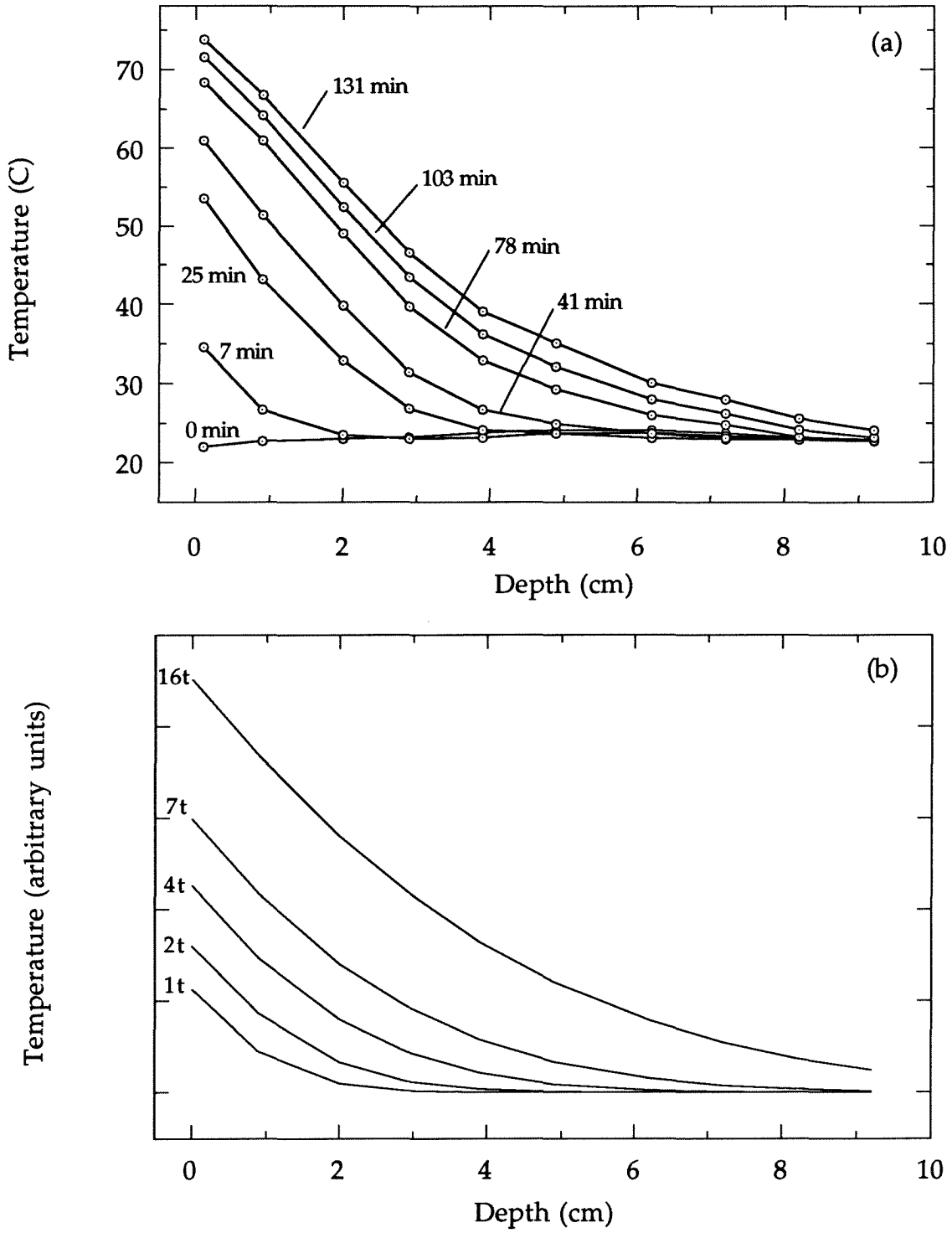

Figure 3.2. (a) Temperature profiles for an infrared source (hot plate) incident on bead surface, at atmospheric pressure. For comparison, (b) shows the theoretical qualitative changes in the thermal profiles for an infinite half-space irradiated with a constant surface flux, at the indicated relative times (see text).

a classic, monotonic error function solution to the heat equation, where F_0 is the surface flux, k the thermal conductivity, and κ the thermal diffusivity. For a qualitative comparison to the experimental profiles, Figure 3.2 (b) shows how the theoretical thermal profile changes with time.

The profiles for visible irradiation in Figure 3.3 show a distinct deviation from this behavior in the uppermost centimeter, as the absorption of radiation at depths of this order provides a subsurface source of heat. The net effect is an inverted thermal gradient to conduct heat from the depth to the surface. The magnitude of the inversion is small, as the air in the pore spaces between the beads provides substantial thermal conductivity in the medium. We were therefore motivated to try similar experiments under vacuum.

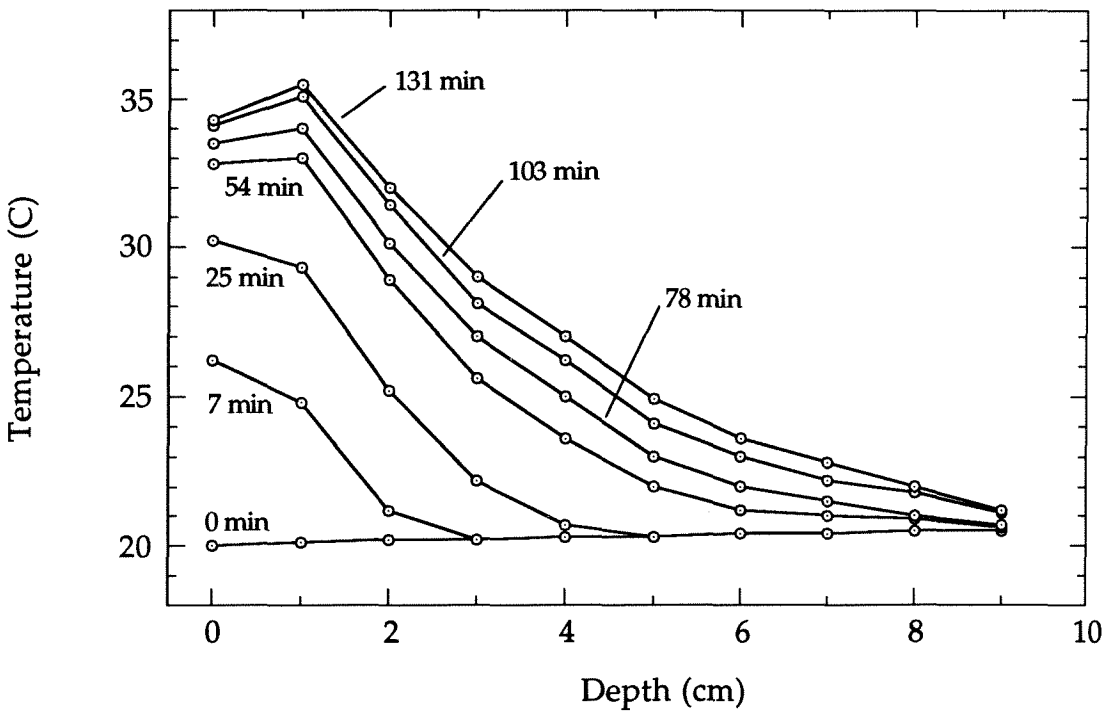

Figure 3.3. Temperature profiles with depth for visible radiation incident on the bead surface, at atmospheric pressure. Note the qualitative difference to Fig. 3.2, due to radiation absorption at depth.

3.3. Experiments in Vacuum

As stated by previous researchers (Wechsler *et al.* 1972), the conduction of heat by gas filling the void spaces between the particles in a bed of packed powder or beads is the largest contribution to the heat transfer at atmospheric pressure. The thermal conductivity of the gas remains roughly constant over a range of gas pressures, becoming proportional to the gas pressure only when the mean free path of the gas is larger than the characteristic void space between the beads, labeled the "breakaway" pressure. The contribution of the gas conductivity is minimal only at pressures below ~ 10^{-2} torr, independent of particle size. For this reason, the magnitude of the greenhouse subsurface temperature enhancement has been estimated to be much larger for the icy surfaces of airless bodies in the outer solar system than in terrestrial environments (Brown and Matson 1987; Matson and Brown 1989). To maximize the effect in the laboratory, the remainder of the experiments were done under vacuum.

3.3.1. Experimental Setup Under Vacuum

The schematic for the vacuum setup is shown in Figure 3.4. The glass bell vacuum chamber was evacuated by a liquid N_2 trapped diffusion pump, consistently operating in the 10^{-6} torr pressure range. The beads and lamps from the atmospheric pressure experiments were used again here. The container holding the beads was a Pyrex beaker, 19 cm in diameter and 10 cm deep. The beaker was loosely wrapped in aluminum foil to keep stray light from entering through the sides. In addition, a foil aperture 10 cm in diameter was suspended above the bead surface to permit the incident light only in the center of the sample surface, so that no visible radiation could

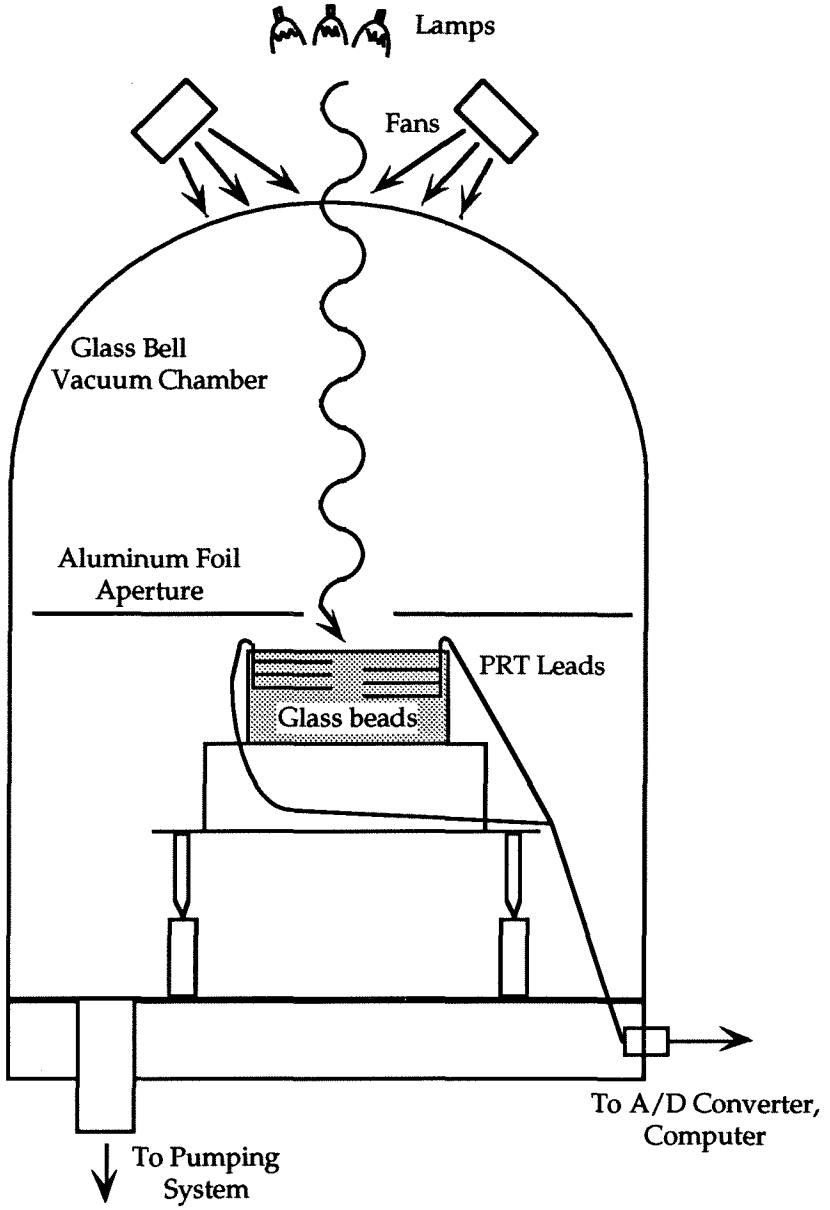

Figure 3.4. Schematic for the experiments done in a vacuum chamber.

penetrate directly to deep layers along the bead-container boundary. The entire container was set on ceramic standoffs to thermally decouple the sample from the base of the vacuum chamber.

To minimize the perturbation caused by the temperature measurement devices, small 1000 Ohm PRT's (Hy-Cal Ultra-7) were

substituted for the thermocouples. The thermocouple leads had a fairly large cross section (22 gauge), which was not a consideration in the first set of experiments due to the substantial thermal conductivity caused by the high gas pressure. The leads to the PRT's were 28 gauge copper wire, insulated and partially shielded in loosely wrapped foil to minimize the direct heating of the wires by radiation, which would have led to anomalous temperature readings. The PRT bodies were white and only 1 mm^2. The PRT's were again placed near the center of the bead sample, spaced vertically 0.5 to 1 cm. Although the PRT's were uncalibrated, the experiments were repeated with different PRT configurations to make sure there were no systematic differences among them.

The beads were allowed to degas overnight under vacuum before the lamps were turned on and the measurements taken. All temperature data were run through an A/D converter and stored on a computer.

3.3.2. Results of Vacuum Irradiation Experiments

Typical temperature profiles during long exposure to visible radiation are shown in Figure 3.5. The thermal inversion is now clear, with $\Delta T \sim 20$ K in the uppermost centimeter of the sample. The relatively small change in profiles between the 24 hour measurement and the final measurement indicates that the system is close to steady-state.

Since the sample had only finite depth, the bottom of the container could cool radiatively. This is different than the model of Matson and Brown (1989), which assumes no net vertical transport of heat at depth in steady-state, as their model encompasses an infinite half-space. The differences between their model assumptions and the laboratory setup will not affect

equation (1), as discussed in Appendix A. However, as the irradiated area is much smaller than the surface area available for radiative cooling, the bottom of the sample will be cooler than the surface in steady-state, giving rise to the gradient at depth in Fig. 3.5.

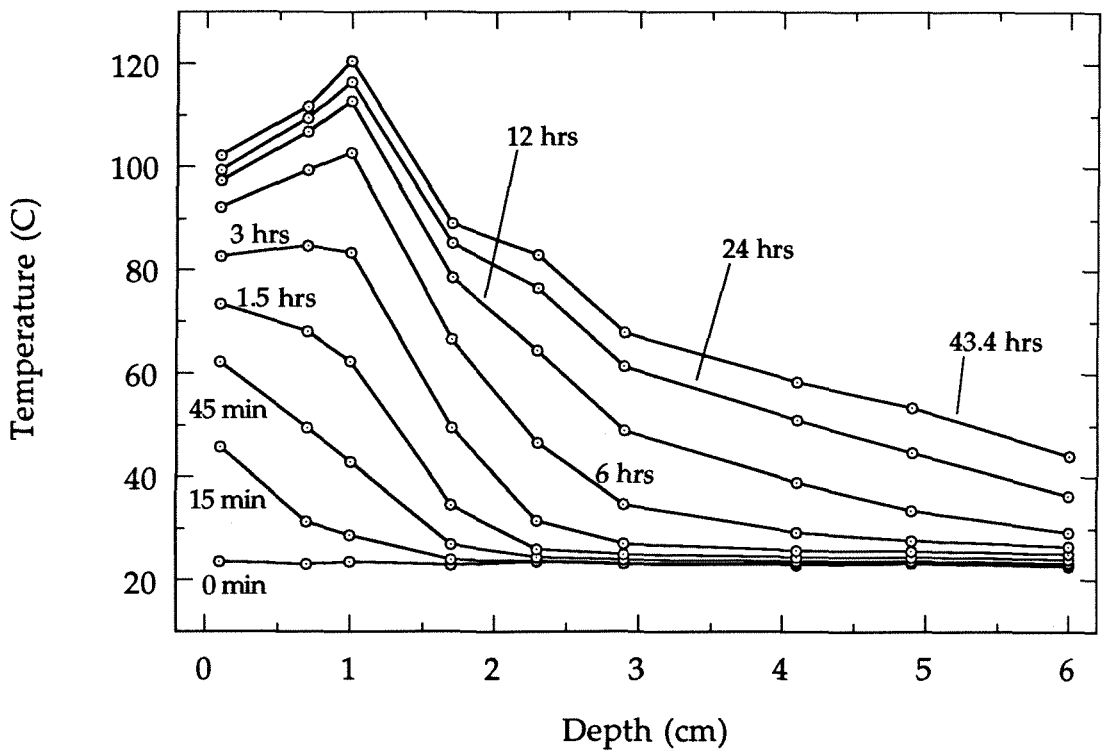

Figure 3.5. Temperature profiles for visible radiation incident on the bead surface under vacuum. The magnitude of the inversion is much larger than that in Fig. 3.3 due to the lower bulk thermal conductivity of the evacuated beads.

3.4. Measuring the Factors That Govern the Inversion Magnitude

The remainder of this paper will focus on making independent measurements of the three parameters that govern the size of the temperature inversion in the samples: the flux of the incident radiation, the absorption scale length of the radiation in the samples, and the bulk thermal

conductivity of the glass beads under vacuum. A comparison of the size of the temperature inversion predicted from these measurements with the one shown in Fig. 3.5 will help verify the predictive power of equation (1).

The incident flux is the easiest of the three parameters to quantify. A broad-band radiometer (Kendall MK IV) was placed at various locations at the level of the bead surface, and the difference taken with the lamps on and off. The background radiation was insignificant compared to that from the lamps. The measured flux varied little over the size of the aperture, with a mean value and standard deviation of $(4.6 \pm 0.2) \times 10^5$ ergs cm^{-2} sec^{-1}.

3.4.1 Determination of the Absorption Scale Length

The absorption per unit length, or absorption scale length, ζ, is the depth at which 1/e of the absorption of flux incident on the surface has occurred. In a two-stream approximation, where the radiation field is assumed to only change in the vertical dimension, ζ is related to the extinction coefficient, μ, by the following (Schlatter 1972):

$$\frac{1}{\zeta} = \frac{1-A}{1+A}\mu \tag{3}$$

where A is the albedo of the surface. To determine an appropriate value for ζ, both μ and A need to be known as functions of wavelength in the spectral region where most of the energy deposition is occurring. An average value of ζ can then be calculated to use in equation (1).

The albedo of a sample of beads was measured by Roger Clark of the USGS in Denver. The reflectance of the beads as a function of incident wavelength is shown in Figure 3.6. The measurement was taken at a single incidence angle, but the reflectance gathered over nearly 2π steradians, so

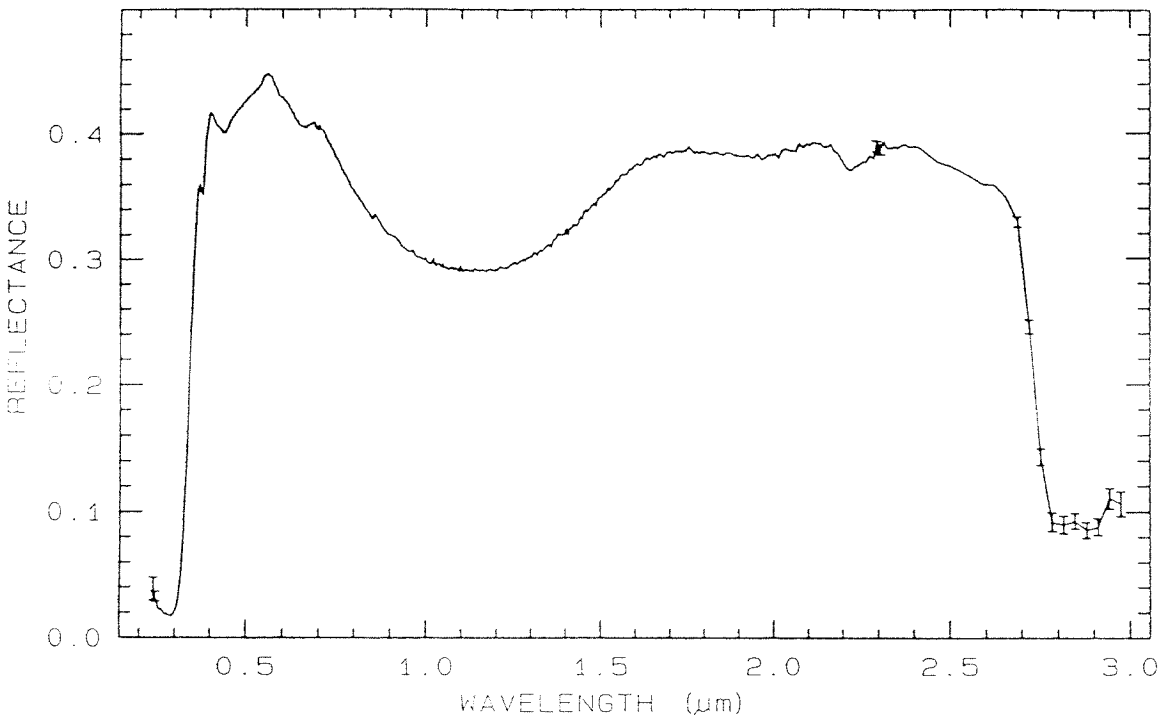

Figure 3.6. Bihemispherical reflectance of a sample of beads (measurement made at USGS in Denver).

barring any major angle of incidence effects, this represents the true bihemispherical albedo.

The reflectance is fairly uniform from 0.4 to 2.6 μm, so within this spectral region, the beads are rather "gray" in reflectance. This is convenient, as nearly all incident radiation from the lamps lies within this wavelength region. The lamps have a color temperature of ~ 3000 K, so the peak spectral output is at 1 μm, with virtually no radiation emitted at wavelengths shorter than 0.4 μm.

The extinction coefficient was determined at two wavelengths, 0.504 μm and 1.06 μm, by measuring the transmitted intensity of two laser sources through bead samples of known thickness. A dye laser was used for the 0.504

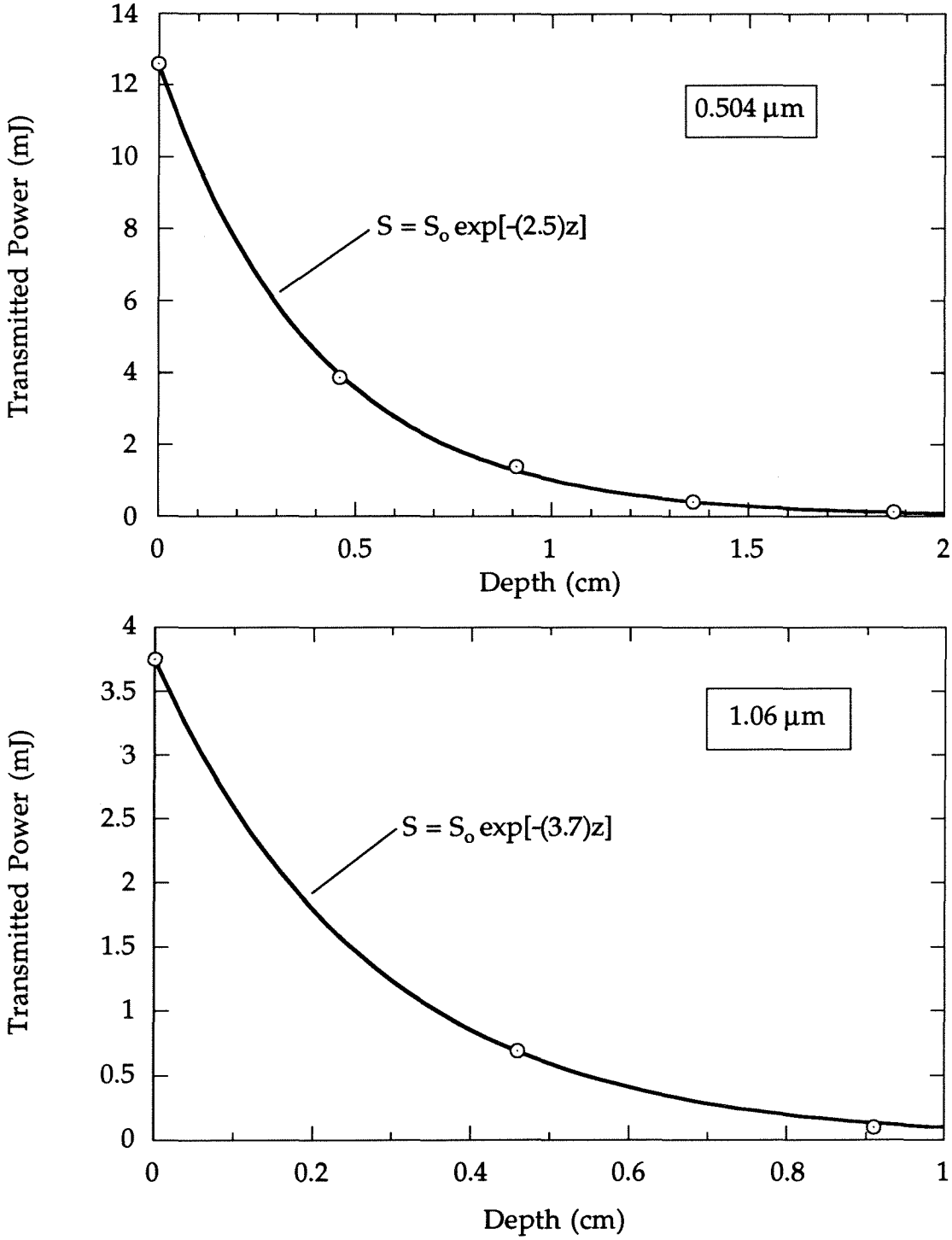

Figure 3.7. Measured extinction profiles for the glass beads at 0.504 and 1.06 μm. The data were taken by measuring the transmitted intensity of two different laser sources through bead samples of known thickness. The solid lines are exponential fits to the data, specified by the given equations.

μm beam, and a YAG for the 1.06 μm radiation. The bead samples were sandwiched between glass plates; all measurements were normalized to the transmittance with no beads in place. Neutral density filters were used to protect the pyrometer (Molectron) measuring the transmittance from overexposure. The results are shown in Figure 3.7, with the data fitted to the exponential curves

$$S = S_0 \exp[-\mu z] . \tag{4}$$

Taking values for μ from the exponential fits, and A from the spectrum in Figure 3.6, values for ζ are determined, with the results summarized in Table 3.1 below:

Table 3.1. Summary of measurements to determine ζ

Wavelength (μm)	μ (cm^{-1})	A	ζ (cm)
0.504	2.5	0.43	1.0
1.06	3.7	0.29	0.5

The value of ζ over the range of incident radiation is thus 0.75 ± 0.25 cm.

3.4.2. Thermal Conductivity of the Glass Bead Bed

The most difficult of the parameters to determine in the inversion magnitude estimate is the thermal conductivity. A short digression is warranted to discuss the work of other researchers in this area.

Several previous measurements of the thermal conductivity of evacuated powders and beads have been made. Watson (1964) determined the thermal conductivity for several different silica powders, including glass beads of various diameters, by remotely measuring the radiated flux from the

surface of a sample heated from below by a thermal bath. This technique was chosen, rather than the direct measurement of the thermal gradient in the sample in response to a known heat source, to avoid the perturbation of temperature measuring devices embedded in the sample. Watson found that the measured conductivity could effectively be modeled as the sum of two parts: a solid conduction term, independent of temperature, due to the contact conduction between the beads, and a radiative conduction term which shows a cubed dependence on temperature. The thermal conductivity thus has the functional form

$$k(T) = B + AT^3 . \qquad (5)$$

Watson's results showed that the radiative transfer coefficient A increases rapidly with bead size, for beads above 100 μm in diameter. He suggested that this trend is caused by the radiation in the pore spaces of the bead bed dominating the radiative transfer, as opposed to the radiation through the beads. The values he found for the coefficients A and B in a bed of glass beads 590 - 840 μm in diameter, similar in size to the beads in my sample, are: A = 2.66×10^{-5} ergs cm^{-1} sec^{-1} K^{-4} and B = -6.6 ergs cm^{-1} sec^{-1} K^{-1}. The negative value for B is not physically meaningful, but this is not important here as the radiative term dominates the effective conductance for all temperatures above ~150 K. For the range of temperatures in our experiments, ~ 300 - 400 K, these values put *k* in the neighborhood of 700 - 1700 ergs cm^{-1} sec^{-1} K^{-1}.

Langseth *et al.* (1972) give experimental results for the conductivity of beads in the same size range, at temperatures of 190 - 300 K, using both thermocouples and PRT's emplaced in a sensor array embedded in the bead bed above a known heat source. Their results give a value for *k* at 300 K of ~ 500 ergs cm^{-1} sec^{-1} K^{-1}. They also found that a compressive load qualitatively increases the thermal conductivity, as the number of bead-bead contacts

increases. Wechsler *et al.* (1972) give a summary of conductivity measurements for much finer beads (~ 40 - 70 μm diameter), with values in the range of $k \sim 120 - 160$ ergs cm^{-1} sec^{-1} K^{-1}.

The effective thermal conductivity in our evacuated samples was measured two different ways. Both methods rely on data obtained from the PRT's sandwiched in the bead bed when measuring the temperature profiles during the irradiation experiments, and are therefore subject to errors caused by heat flow through the temperature leads, to be discussed later in this section. The first technique uses an estimate of the heat flux from the bead bed surface as it cools, after the irradiating lamp was turned off. Assuming the surface cools radiatively, the heat flux from the surface can be approximated by:

$$\sigma(T_{surface}^4 - T_{room}^4) = -k\frac{\delta T}{\delta z} \quad . \tag{6}$$

The thermal profiles of the cooling sample can be used to determine both the surface temperature and the gradient. Figure 3.8 (a) shows the cooling profiles for the same sample as shown in the heating profiles of Fig. 3.5, for the first 55 minutes of cooling. Only the top 3 cm of the profile are shown, as the sample below this depth changed very little in this time. Taking the temperature difference between the top two measurement depths in the sample (1 and 7 mm) to be the thermal gradient supporting the surface flux, the thermal conductivity can be estimated for each surface temperature, taken to be the temperature measured at a depth of 1 mm. Using 295 K as the room temperature, Figure 3.8 (b) shows the thermal conductivity as a function of surface temperature. An estimate for the surface temperature from time $t = 0$ is not included, as the sample was still being irradiated at this time.

Also in Fig. 3.8 (b) is an attempt to fit the experimental conductivities by a cubic dependence on temperature such as eqn. (5). A fit cannot be made to all the data, which is not surprising, as the measurements were not taken

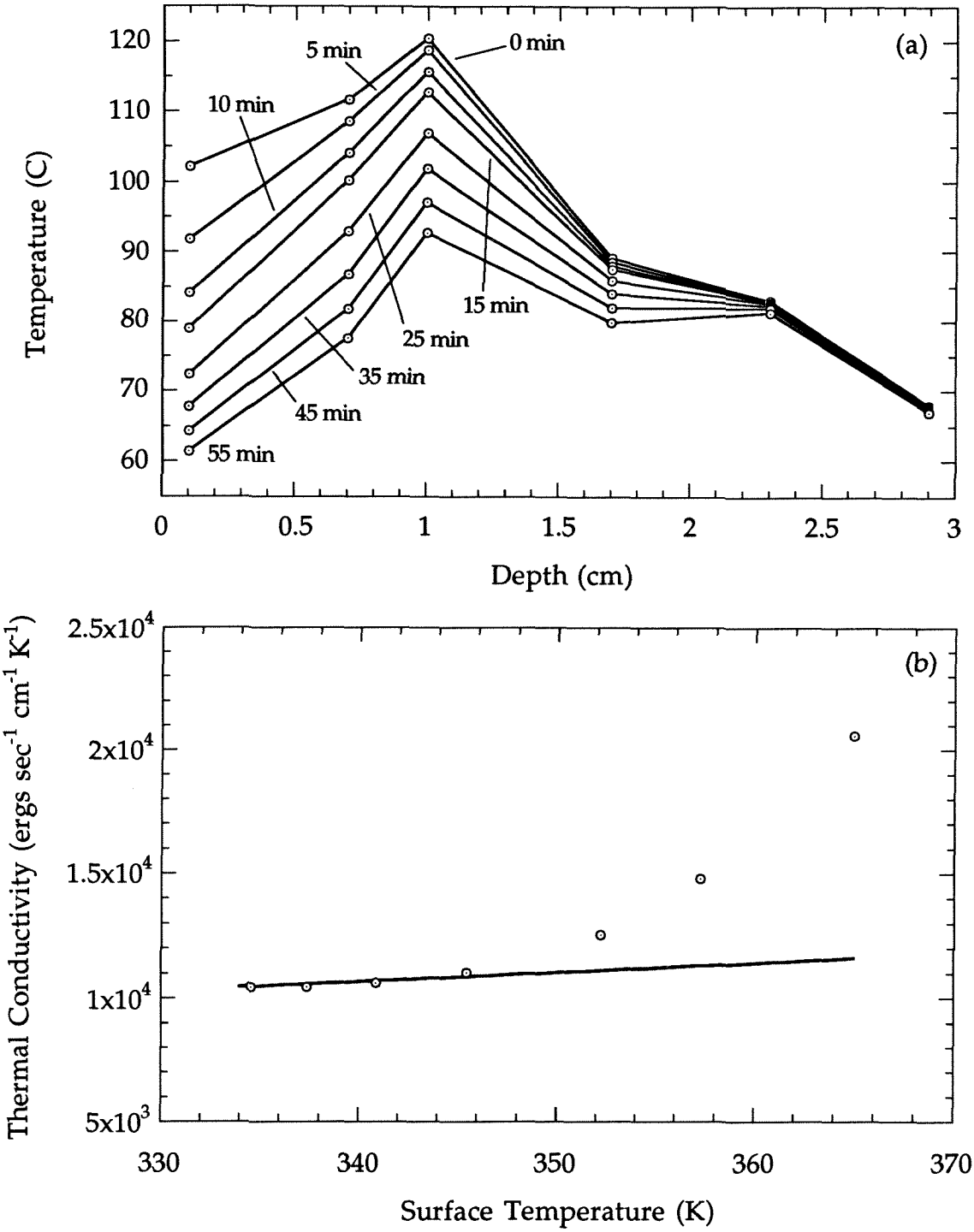

Figure 3.8. (a) Cooling profiles for the vacuum irradiation experiment shown in Fig. 3.5. Data below 3 cm did not change in the 55 minutes of monitoring. (b) The thermal conductivity as calculated from the surface temperature and near-surface gradient (points). The curve is an attempt to fit the thermal conductivity as a cubic function of temperature (see text).

under steady-state conditions. The gradient between the top two sensors steepens initially due to the light source being tuned off, with the beads closest to the surface cooling the most rapidly. Although the beads are never in equilibrium during cooling, it is reasonable to assume that the temperature profiles taken the longest time after the cooling begin approach an equilibrium surface gradient, and therefore provide the data best represented by the behavior of eqn. (5). The least-squares fit in Fig. 3.8 (b) only uses the lowest four experimental surface temperatures (from the last four measurements taken). Taking this fit to be indicative of the steady-state change in effective thermal conductivity with temperature, one can see that the conductivity is not a strong function of temperature. The value of k determined from this method is ~ 1×10^4 ergs cm^{-1} sec^{-1} K^{-1}.

The second method employed to calculate the thermal conductivity of the sample was to first measure the thermal diffusivity. As the diffusivity is given by

$$\kappa = k/\rho c\,, \tag{7}$$

where ρ is the bulk density and c is the specific heat, the conductivity can easily be calculated for measured or known values of κ, ρ, and c. The bulk density of the packed beads was measured to be 1.5 g cm^{-3} by weighing a known volume. The specific heat for the glass used in the beads was given by the manufacturer as 8.7×10^6 ergs g^{-1} K^{-1}.

Monitoring the speed at which a thermal wave propagates through the beads allows an estimate of the thermal diffusivity. This must be done well below the penetration scale length of light in the sample, at a depth where the heat transfer is only due to thermal conduction. For these calculations, only data from 4 cm or more below the sample surface were used, well below the region receiving direct radiation from the source lamps.

Taking the flow of heat as only being significant in the vertical direction (see Appendix A for a discussion of the validity of this assumption), the equation for heat flow is given by:

$$\frac{\delta T(t,z)}{\delta t} = \kappa \frac{\delta^2 T(t,z)}{\delta z^2} \,. \tag{8}$$

This assumes that the diffusivity is constant with temperature. This equation can be approximated in a discrete form,

$$\frac{T_z(t+\Delta t) - T_z(t)}{\Delta t} \approx \kappa \left[\frac{\left(\frac{T_{z+\Delta z}(t) - T_z(t)}{\Delta z} \right) - \left(\frac{T_z(t) - T_{z-\Delta z}(t)}{\Delta z} \right)}{\Delta z} \right], \tag{9}$$

where $T_z(t)$ is the temperature at depth z and time t. For the sample heating profiles shown in Fig. 3.5, the diffusivity was calculated for the measured points below 4 cm for each successive measurement in time. Averaging over these calculated diffusivities gives $\kappa = (3.7 \pm 2.7) \times 10^{-4}$ cm^2 sec^{-1}. Substituting the values mentioned above for the density and specific heat gives $k = (4.8 \pm 3.5) \times 10^3$ ergs cm^{-1} sec^{-1} K^{-1}, smaller than the rough value determined from the surface flux, but still larger than the thermal conductivities reported by previous authors.

An important factor to consider when estimating the conductivity is the degree to which the wire leads to the PRT's perturb the thermal profile by conducting heat rapidly out of the region where the temperatures are being measured. A comparison of the total power conducted through the wire leads versus the bead bed will provide an estimate of how strongly the leads perturb the thermal profile. The power conducted through a single lead is given by

$$P = -\sigma k \frac{dT}{dx} \,, \tag{10}$$

where σ in the wire cross-section (28 gauge = 8.14×10^{-4} cm^2), k is the thermal conductivity of the wire (~4×10^7 ergs cm^{-1} sec^{-1} K^{-1} for copper), and dT/dx is the thermal gradient, taken to be ~100 K/10 cm along a lead placed at a depth of 1 cm, the hottest depth in the sample. The power conducted through a single lead is thus ~ 3×10^5 ergs sec^{-1}. Accounting for all nine leads in the sample, and including the foil that shielded the leads from direct radiation, this figure increases, perhaps by as much as an order of magnitude.

To estimate the total power conducted through the beads, $\sigma \sim 75$ cm^2 (the approximate area of the bead surface being irradiated), k = 5×10^3 ergs cm^{-1} sec^{-1} K^{-1}, and $\Delta T/\Delta z = 20$ K/cm, giving P ~ 7.5×10^6 ergs/sec, Thus the total conduction of heat through the wire leads is probably comparable to that conducted through the beads, certainly large enough to significantly affect the thermal profile. The primary effect will be to flatten the profile, as the rate of energy loss is proportional to the size of the gradient along the wire, so that the leads have the largest affect at the hottest depths. The low conductivities found by Watson (1964), Wechsler *et al.* (1972), and Langseth *et al.* (1972) may be true of our pure bead samples as well, but the presence of the conducting leads in the samples raises the effective conductivity, and thus reduces the magnitude of the inversion. However, as the size of the inversion is measured with the leads in place, it makes sense to measure the thermal conductivity with the same set up.

3.4.3. Comparing the Predicted and Measured Inversion Magnitudes

Using the measured values for the incident flux, absorption scale length, and thermal conductivity, we can compare the magnitude of the thermal inversion predicted by eqn. (1) with that shown in Fig. 3.5. As the

thermal conductivity measurements yielded two values that were somewhat different, both will be used for comparison.

If we take the thermal conductivity as $k = 5 \times 10^3$ ergs cm^{-1} sec^{-1} K^{-1}, $\zeta = 0.75 \pm 0.25$ cm, and $S = 4.6 \pm 0.2 \times 10^5$ ergs cm^{-2} sec^{-1}, then $\Delta T = 69 \pm 25$ K from eqn. (1), which at best is a factor of two larger than the measured value of $\Delta T =$ 20 K. If $k = 10^4$ ergs cm^{-1} sec^{-1} K^{-1}, then $\Delta T = 35 \pm 12$ K. Although this is still a bit larger than the measured value, within the uncertainty of the thermal conductivity, eqn. (1) does give a reasonable estimate of the magnitude of the thermal inversion caused by the solid-state greenhouse effect.

The calculated values for the inversion magnitude are systematically higher than that actually measured. Apart from the difficulty of pinning down the thermal conductivity, another reason for this discrepancy is in the estimated value for ζ. If an appreciable amount of incident radiation had an absorption scale length much smaller than the given value of 0.75 cm, the predicted inversion would be smaller. A calculation for ζ that included the measured spectral output of the lamp would be more accurate than the simple bolometric average derived in Section 3.4.1.

3.5. Conclusions

We have shown that a solid-state greenhouse can readily be produced in the laboratory, using a bed of evacuated glass beads to simulate a planetary surface. Measurements of the incident radiative flux, absorption scale length, and thermal conductivity confirm that the magnitude of the subsurface temperature enhancement is reasonably predicted from these parameters as specified by eqn. (1).

Glass beads provide the necessary optical characteristics to set up a greenhouse inversion. However, their direct applicability to any planetary environment is limited. They were chosen as the operating medium only to keep the experiments as simple as possible. Unlike ices, glass beads do not experience any sort of phase change when moderately heated. The rapid sublimation of ices due to subsurface greenhouse temperature enhancements on an actual planetary surface would probably lead to widespread grain sintering and densification (Matson and Brown 1989; Eluszkiewicz 1991; Fanale *et al.* 1990), which would raise the thermal conductivity, lessening the magnitude of the inversion. This negative feedback makes the solid-state greenhouse effect in ices a self-limiting process, so that the temperature enhancements on actual planetary surfaces may be minimal. Experiments similar to those presented here, using ice grains instead of beads, would be much more complex, but they are necessary to establish the applicability of the solid-state greenhouse effect in actual planetary environments.

References

Brandt, R. E., and S. G. Warren 1993. Solar-heating rates and temperature profiles in Antarctic snow and ice. *J. Glaciol.* **39**, 99.

Brown, R. H., and D. L. Matson 1987. Thermal effects of insolation propagation into the regoliths of airless bodies. *Icarus* **72**, 84.

Carslaw, H. S., and J. C. Jaeger 1959. *Conduction of Heat in Solids.* p. 75. Oxford University Press, London.

Eluszkiewicz, J. 1991. On the microphysical state of the surface of Triton. *J. Geopys. Res.* **96**, 19217.

Fanale, F. P., J. R. Salvail, D. L. Matson, and R. H. Brown 1990. The effect of volume phase changes, mass transport, sunlight penetration, and densification on the thermal regime of icy regoliths. *Icarus* **88**, 193.

Langseth, M. G., Jr., S. P. Clark, Jr., J. Chute, Jr., and S. Keihm 1972. The Apollo 15 lunar heat flow measurement. In *Thermal Characteristics of the Moon* (J. W. Lucas, Ed.), pp. 215-241. MIT Press, Cambridge.

Matson, D. L., and R. H. Brown 1989. Solid-state greenhouses and their implications for icy satellites. *Icarus* **77**, 67.

Schlatter, T.W. 1972. The local surface energy balance and subsurface temperature regime in Antarctica. *J. App. Meteor.* **11**, 1048.

Watson, K. 1964. The thermal conductivity measurements of selected silicate powders in vacuum from 150° - 350° K. Ph.D. Thesis, California Institute of Technology.

Wechsler, A. E., P. E. Glaser, and J. A. Fountain 1972. Thermal properties of granulated materials. In *Thermal Characteristics of the Moon* (J. W. Lucas, Ed.), pp. 215-241. MIT Press, Cambridge.

Appendix - The Predicted Inversion Magnitude in the Laboratory Geometry

Equation (1) in the main manuscript, $\overline{\Delta T} = \overline{S'(t)}\frac{\zeta}{k}$, was derived by Matson and Brown (1989) for an infinite half-space subjected to a periodic radiation source, to model the conditions on the surface of a rotating body. The laboratory situation is somewhat different: first, the radiation source is constant, and second, the sample has a finite volume. A constant radiation source does not change the fundamental physics that govern eqn. (1), even if a finite thickness is assumed, but a finite volume does alter the calculations, as discussed below.

Following the derivation of Matson and Brown (1989), the steady-state equation for one-dimensional heat flow in an infinite half-space or infinite slab of thickness d is:

$$\frac{\partial^2 T(z)}{\partial z^2} = \frac{1}{k}\frac{\partial S(z)}{\partial z}, \tag{2}$$

where $S(z) = S_o e^{-z/\zeta}$ is the incident radiation field. Integrating over z:

$$\frac{\partial T(z)}{\partial z} = \frac{1}{k} S_o e^{-z/\zeta} + \text{constant}. \tag{3}$$

As $\zeta \rightarrow 0$ (i.e., all radiation absorbed at the surface), $\frac{\partial T(z)}{\partial z} \rightarrow 0$, so that the constant in eqn. (3) = 0. Integrating eqn. (3):

$$\int_0^z \frac{\partial T(z')}{\partial z'} dz' = \frac{S_o}{k} \int_0^z e^{-z'/\zeta} dz' \tag{4}$$

$$T(z) - T(0) = \frac{S_o \zeta}{k} \left(1 - e^{-z/\zeta}\right). \tag{5}$$

If $d >> \zeta$, then

$$T(d) - T(0) = \frac{S_o \zeta}{k} . \tag{6}$$

So for a constant radiation source incident on an infinite slab of thickness d, eqn. (1) still holds.

The approximation of an infinite slab is valid if the incident radiation field is uniform over a dimension much greater than the slab thickness. For the vacuum experiments, the sample thickness (10 cm) was roughly the same as the lateral dimension of the incident radiation, so at depth, the problem is no longer one-dimensional, as there will be steady-state thermal gradients orthogonal to the vertical dimension. However, the radiation field is uniform over a dimension much greater than ζ, so the depth of the sample that shows a thermal inversion is essentially one-dimensional. Thus eqn. (1) still provides a reasonable approximation for the inversion magnitude.